AC MAGNETIC CHARACTERIZATION OF NANOCRYSTALINE $Ni_{0.50-x}Cu_xZn_{0.50}Fe_2O_4$ PREPARED BY COMBUSTION TECHNIQUE

A Dissertation Submitted to the Department of Physics, Bangladesh University of Engineering & Technology, Dhaka, in Partial Fulfillment of the Requirement for the Degree of Master of Philosophy in Physics

SUBMITTED

By

Muhammad Lutfor Rahman

EXAMINATION ROLL NO. : **100614016F**
SESSION : **October 2006**

DEPARTMENT OF PHYSICS
BANGLADESH UNIVERSITY OF ENGINEERING & TECHNOLOGY
DHAKA 1000, BANGLADESH

BANGLADESH UNIVERSITY OF ENGINEERING & TECHNOLOGY
DEPARTMENT OF PHYSICS, DHAKA 1000, BANGLADESH

CERTIFICATION OF THESIS

The thesis titled "**AC MAGNETIC CHARACTERIZATION OF NANOCRYSTALLINE $Ni_{0.50-x}Cu_xZn_{0.50}Fe_2O_4$ PREPARED BY COMBUSTION TECHNIQUE**" submitted by **Muhammad Lutfor Rahman**, Roll No.: 100614016F, Session: October 2006, has been accepted as satisfactory in partial fulfillment of the requirement for the degree of **Master of Philosophy** in Physics on January 27, 2010

BOARD OF EXAMINERS

1. A. Hossain
Dr. A. K. M. Akther Hossain (Supervisor)
Professor, Department of Physics,
BUET, Dhaka — Chairman

2. A. Hossain
Head, Department of Physics,
BUET, Dhaka — Member (Ex- Officio)

3. Dr. Mominul Huq
Professor
Department of Physics,
BUET, Dhaka — Member

4. Dr. Sabina Hussain
Associate Professor,
Department of Physics,
University of Dhaka — Member (External)

CANDIDATE'S DECLARATION

It is hereby declared that this thesis or any part of it has not been submitted elsewhere for the award of any degree or diploma.

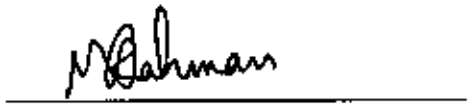

Muhammad Lutfor Rahman

ACKNOWLEDGEMENTS

I firstly express all of my admiration and devotion to the almighty Allah, the most beneficial who has enabled me to perform this research work and to submit this thesis.

I express my profound gratitude to my honourable supervisor Professor Dr. A.K.M. Akther Hossain, Department of Physics, BUET, for his constant guidance, constructive criticism and inspiration in pursuing the whole investigation of the present research. Words are always insufficient to express his unending enthusiasm for scientific rigorousness for innovative investigations This always becomes the everlasting source of inspiration for his students.

I am deeply grateful to Head, Department of Physics, BUET, for his kind permission to do this work. Thanks to BUET authority for providing the financial grant for this research.

I would like to express my gratitude to Professor Dr Mominul Huq, Professor Dr. Md. Abu Hashan Bhuiyan, Professor Dr. Nazma Zaman, Professor Dr Jiban Podder, Professor Dr. Md. Mostak Hossain, Mrs. Fahima Khanam, Dr. Nazrul Islam,, Dr Afia Begum, Dr Md. RafiUddin, Dr. Md. Forhad Mina and all other teachers of Physics Department, and Professor A. A Z Ahmad, chairperson, Department of Mathematics and Natural Sciences, BRAC University.

Special thanks to Professor Dr. Abdur Rashid, head, Department of Physic,Chittagong University of Engineering & Technology, for providing the facilities of A.C. magnetic measurements on their Impedence Analyzer.

I am thankful to my senior research worker Md.Abdul Hamidur Rahman Khan, Md.Farhad Alam,Shaikh Tawhid Mahmud, Tushar Shuvra Bistvas, Mr Omar Faruk, Khurshed Alam,Mahabub Rahman Shah for their cooperation throughout the study. Many many thanks to my friends Badal, Tarana, Binindita, Newaz, Ruhul and Harun for their inspiration and encouragement. I also gratefully acknowledge the wishes of my younger researchers, Maruf, Abdur Rahman for their constant support

Finally, I would mention a very special gratefulness for the moral support and sustaining inspiration provided by the members of my family specially my Parents and my elder sister. This dissertation would never have been possible without their love, affection and encouragement.

The Author

Muhammad Lutfor Rahman

ABSTRACT

Nanolycrystalline $Ni_{0.50-x}Cu_xZn_{0.50}Fe_2O_4$ (x varies from 0 to 0.25 insteps of 0.05) and $Ni_{0.45-x}Cu_{(x+y)}Zn_{0.55-y}Fe_2O_4$ (x and y varies from 0 to 0.10 insteps of 0.05 and 0.10 respectively) ferrites were prepared by combustion technique. The samples prepared from each composition were sintered at various temperatures in air for 5 hours. Structural and surface morphology were studied by X-ray diffraction and optical microscopy, respectively. The magnetic properties of these ferrites were characterized with high frequency (1 kHz-15 MHz) complex permeability and temperature dependent permeability measurements. The DC magnetizations as a function of applied magnetic field were measured at temperature 300K by SQUID magnetometer. The effects of microstructure, composition and sintering temperatures on the complex permeability of various $Ni_{0.50-x}Cu_xZn_{0.50}Fe_2O_4$ and $Ni_{0.45-x}Cu_{(x+y)}Zn_{0.55-y}Fe_2O_4$ ferrites are discussed. A possible correlation among sintering temperature, grain size and density is also discussed.

It was observed that the samples formed spinel structure.The lattice constant of all these samples follow Vegard's law. The X-ray densities of the samples increase with increasing Cu^{2+} content. On the other hand, the bulk densities of the samples increases and the corresponding porosity of the samples decreases with increasing of Cu^{2+} content up to x=0.10 Beyond this value of x, density decreases as well as porosity increases. The sintering densities of the polycrystalline $Ni_{0.50-x}Cu_xZn_{0.50}Fe_2O_4$ and $Ni_{0.45-x}Cu_{(x+y)}Zn_{0.55-y}Fe_2O_4$ increases in increasing sintering temperature up to optimum temperature above that the densities decreases. The microstructural study shows that grain size increases with increasing Cu^{2+} content up to an optimum concentration after that it decrease. The compositional variation of complex permeability spectra, loss factor and relative quality factor (Q) were studied with frequencies for the samples sintered at various temperatures. The general characteristic of the permeability spectra is that the real part of initial permeability (μ_i') remain fairly constant in the frequency range up to some critical frequency characterized by the onset of resonance, while at higher frequency it drops rapidly to a very small value and imaginary part (μ_i'') increase to have a peak. The Q is found to be increase with increasing Cu^{2+} content up to an optimum level beyond that it decreases. It is also observed that the Q value decreases

with increasing of sintering temperature and loss factors are minimum for frequency up to 1 MHz.The Néel temperature, T_N, of these samples are determined from the temperature dependent initial permeability which shows a decreasing trend as a function of composition due to the weakening of the *A-B* interaction and increasing trend due to the strengthen of the *A-B* interaction Compositional variation saturation magnetization, saturating field, Bohr magneton were calculated from M-H loops measurement. The variation saturation magnetizations were described on the basis of cation distribution

CONTENTS

CHAPTER 6

LIST OF FIGURES

LIST OF TABLES

LIST OF SYMBOLS AND ABBREVIATIONS

AC	Alternating current
B	Magnetic induction
CMR	Colossal magnetoresistance
$F(\theta)$	Nelson-Riley function
f_r	Resonance frequency
g	Landé splitting factor
H_{ci}	Critical field
J	Exchange integral
K	Total anisotropy
K_1	Magnetocrystalline anisotropy constant
L_s	Self-inductance of the sample core
L_o	Inductance of the winding coil without sample
M	Magnetization
M_s	Saturation magnetization
N_A	Avogadro's number
P	Porosity
P_{intra}	Intragranular porosity
P_{inter}	Intergranular porosity
P_e	Eddy-current loss
Q	Relative quality factor
T_c	Curie temperature
T_N	Néel temperature
T_s	Sintering temperature
$tan\ \delta$	Loss factor
Z	Complex impedance
θ	Bragg's angle
α	Restoring force coefficient
β	Viscous damping factor
γ	Domain wall energy
ω	Angular velocity
δ_w	Domain wall thickness
μ_i	Initial permeability
μ'	Real part of complex permeability
μ''	Imaginary part of complex permeability
μ_B	Bohr magneton
χ_{spin}	Intrinsic rotational susceptibility
χ_w	Domain wall susceptibility

CHAPTER 1
INTRODUCTION

1.1 Introduction

Physics of magnetic nanoparticles continue to be a fascinating subject of interest both from the fundamental and application points of view. Especially, the magnetic nanomaterials show some unusual behavior as an effect of nanoscale confinement. Basically the nano-size particle have attracted some research interest because of their potential applications as microwave absorbing and shielding materials [1] and in the electromagnetic devices like inductors, dc-dc converters [2]. In particular, for the electromagnetic devices applications at high frequencies [3,4] researchers have long been searching soft magnetic materials with high saturation magnetization, high permeability and low energy losses [5-7]. Magnetic saturation, coercivity, magnetization and magnetic loss change drastically as the particle size move down to the nano-scale range. It has been observed that they have super-paramagnetic properties. due to their reduced size. These make them attractive candidates for the information storage, magneto-optical devices and many other applications including magnetic fluids, magnetic latex etc.

On the other hand, there is an intense demand for high performance and miniaturization of many electronic devices. For some devices soft magnetic materials of high permeability is desired Most modern soft ferrites have spinel type crystal structure. It has tetrahedral A site and octahedral B site in AB_2O_4 crystal structure. It shows various magnetic properties depending on the compositions and cation distribution. Various cations can be placed in A site and B site to tune its magnetic properties. Depending on A site and B site cations it can exhibit ferromagnetic, antiferromagnetic, spin (cluster) glass, and paramagnetic behaviour [8]. The general chemical formula of such ferrites is $MeFe_2O_4$, where Me represents one or several of the divalent transition metals. These types of ferrites are subjects of intense theoretical and experimental investigation due to their remarkable magnetic and electric properties [9-23].

The $Ni_{1-x}Zn_xFe_2O_4$ ferrites are most popular and versatile which was investigated by many scientists [9, 24-27]. Recently in our laboratory S. T. Mahmud studied grain size dependent permeability of $Ni_{0.60}Zn_{0.40}Fe_2O_4$ and $Ni_{0.80}Zn_{0.20}Fe_2O_4$ ferrites [28]. Frequency dependence permeability of $Co_{0.60}Zn_{0.40}Fe_2O_4$ and $Co_{0.80}Zn_{0.20}Fe_2O_4$ ferrites were studied by K. K. Kabir [29]. Influence of Mg and Cr substitution on structural and magnetic properties of polycrystalline $Ni_{0.50}Zn_{0.50-x-y}Mg_xCr_yFe_2O_4$, and enhancement of initial permeability due to Mn substitution in polycrystalline $Ni_{0.50-x}Mn_xZn_{0.50}Fe_2O_4$ were studied by T. S. Biswas [30].

Recently grain size dependence permeability of polycrystalline Ni-Zn ferrites prepared with conventional solid state reaction technique has been studied in our laboratory [25]. It was observed that if the polycrystalline samples are prepared from fine powders, there is an enlargement of grain size at lower sintering temperature. In solid state reaction technique, there are some limitations of having smaller particle size. Combustion technique is suitable for the preparation of nano sized initial powders. Combustion technique is also time consuming as well as power saving. In our present research work we are interested to study structural, AC and DC magnetic properties of different $Ni_{0.50}Zn_{0.50}Fe_2O_4$ doped by Cu^{2+} which were prepared by combustion technique. Possible explanation for the observed characteristics of magnetization and initial permeability of the studied samples are discussed.

1.2 Objectives of the present work

The Cu substituted ferrites with their ease of preparation and versatility for use in wide ranging applications are commercially very attractive. These ferrites are used in the surface mount devices (SMD) and multilayer chip inductors (MLCI) due to their high electrical resistivity and excellent soft magnetic properties at high frequencies [31]. The addition of Cu in the ferrite composition has also been known to play a crucial role in lowering the firing temperature. The aim of this study is to investigate the effects of compositional change of a stoichiometric $Ni_{0.50}Zn_{0.50}Fe_2O_4$ by partial substitution of Ni^{2+} with divalent cations Cu^{2+} on structural, morphological and physical properties.

The main objectives of the present research are as follows:

- Preparation of various $Ni_{0.50-x}Cu_xZn_{0.50}Fe_2O_4$ (x=0, 0.05, 0.10, 0.15, 0.20, and 0.25) and $Ni_{0.45-x}Cu_{(x+y)}Zn_{0.55-y}Fe_2O_4$ (x=0, 0.05, 0.10 and y=0, 0.10, and 0.10) samples.
- Study of structural characterizations (x-ray diffraction), density and porosity of the samples.
- Study of surface morphology (grain size).
- Determination of ferrimagnetic to paramagnetic transition temperature (T_K) from measurement of temperature dependent initial permeability.
- Measurement of initial permeability as a function of frequency (1 KHz-15MHz) for samples having various microstructures (e g. grain size).

Possible outcome of the research is as follows:

Combustion technique is expected to produce nanocrystalline initial powder. Samples prepared from these initial powders will have fewer defects and hence materials with improved magnetic properties are expected. From the sintering temperature (T_s) dependent grain size studies, an optimum T_s may be obtained for corresponding ferrite composition. A scaling of frequency dependent initial permeability with respect to grain size may be obtained, which will be helpful for practical applications of the above mentioned ferrites.

At present, Bangladesh is very dependent on the imported ferrite cores and other soft magnetic materials. If we develop a high quality ferrite with desired characteristics in our country, importation can be stopped that will save foreign currency.

1.3 Summary of the thesis

The summary of the thesis is as follows:

Chapter 1 deals with the importance of ferrites and objectives of the present work.

Chapter 2 gives a brief overview of the materials, theoretical background as well as crystal structure of the spinel ferrites.

Chapter 3 gives the details of the sample preparation

Chapter 4 gives descriptions of different experimental setup that have been used in this research work.

Chapter 5 is devoted to the results of various investigations of the study and a brief discussion.

The conclusions drawn from the overall experimental results and discussion are presented in chapter 6

References

[1] Petrov, V M. and Gagulin. V.V., "Microwave Absorbing Materials," *Neorg. Mater.* **37(2)**, 135–141, (2001)

[2] Mazaleyrat, F., Varga, L.K., "Ferromagnetic Nanocompsites," *J. Magn. Magn. Mater.*, **253** 215–216,(2000).

[3] Hayakawa, Y., Makino, A., Fujimori, H., "High resistive nanocrystalline Fe-M-O (M=Hf, Zr, rare-earth metals) soft magnetic films for high-frequency applications," *J. Appl. Phys.*, **81(8)**, 3747, (1997).

[4] Turgut, Z., Nuhfer, N. T., Piehler, H. R., McHenry, M. E., "Magnetic properties and microstructural observations of oxide coated FeCo nanocrystals before and after compaction," *J. Appl. Phys.* **85**, 4406 (1999)

[5] Kasagi, T., T Tsutaoka and K. Hatakeyama, "Particle size effect on the compex permeability for permalloy composite materials," *IEEE Trans. Magn.*,**35(5)**, 3424-3426, (1999).

[6] Moulin, J., Champion, Y., Varga, L.K., Grenèche, J.-M., Mazaleyrat, F., "Magnetic properties of nanocomposites containing Fe-Ni or Fe dispersed in a Mn-Zn ferrite matrix."*IEEE Trans. Magn.***38(5)**, 3015-3017(2002)

[7] Zhao, YW; Zhang, T; Xiao, JQ,"Explosion compacted FeCo particles coated with ferrites. A possible route to achieve artificial softferrites." *J. Appl. Phys.* **93**, 8014-8016, (2003).

[8] Alex Goldman, *Modern Ferrite Technology, 2nd Ed* © 2006 Springer Science+BusinessMedia, Inc. Ferrite Technology Pittsburgh, PA, USA.

[9] A. K. M. Akther Hossain, M. Seki, T. Kawai and H. Tabata, "Colossal magnetoresistance in spinel type $Zn_{1-x}Ni_xFe_2O_4$," *J. Appl. Phys.*, **96**, 1273 (2004).

[10] L. K. Leung, B. J. Evans and A. H. Morrish, "Low-temperature Mössbauer study of a nickel-zinc ferrite $Zn_{1-x}Ni_xFe_2O_4$," *Phys. Rev. B*, **8**, 29 (1973).

[11] W. Schiessl, W. Potzel, H. Karzel, M. Steiner and G. M. Kalvius, "Magnetic properties of the $ZnFe_2O_4$ spinel," *Phys. Rev. B*, **53**, 9143 (1996).

[12] J. M. Hasting and L. M. Corliss, "An antiferromagnetic transition in zinc ferrite," *Phys. Rev.*, **102**, 1460 (1956).

[13] J. M. Hasting and L. M. Corliss, "Neutron diffraction studies of zinc ferrite and nickel ferrite." *Rev. Mod. Phys.*, **15**, 114 (1953)

[14] A. Goldman, *Handbook of Modern Ferromagnetic Materials*, Kulwer Acad. Pub, Boston, U.S.A. (1999)

[15] R. Valenzuela, *Magnetic Ceramics*, Cambridge University Press, Cambridge (1994)

[16] M. A. Ahmed, N. Okasa and L. Salah, "Influence of yttrium ions on the magnetic properties of Ni-Zn ferrites," *J. Magn. Magn. Mater.*, **264**, 241 (2003).

[17] A. Verma, T. C. Goel, R. G. Mendiratta and P. Kishan, "Magnetic properties of nickel-zinc ferrites prepared by the citrate precursor method," *J. Magn. Magn. Mater.*, **208**, 13 (2000).

[18] G. Ranga Mohan, D. Ravinder, A. V. Ramana Reddy and B. S. Boyanov, "Dielectric properties of polycrystalline mixed nickel-zinc ferrites," *Materials Letters*, **40**, 39 (1999).

[19] Yu. G. Chukalkin and A. E. Teplykh, "Magnetic state of nickel-zinc ferrites at high zinc concentrations," *Phys. Solid State*, **40(8)**, 1364 (1998).

[20] N. Rezlescu, E. Rezlescu, C. Pasnicu and M. L. Craus, "Effects of the rare-earth ions on some properties of a nickel-Zinc ferrite," *J. Phys.: Condens. Matter*, **6**, 5707 (1994).

[21] M. El-Shabasy, "DC electrical properties of Ni-Zn ferrites," *J. Magn. Magn. Mater.*, **172**, 188 (1997).

[22] M. I. Rosales, E. Amano, M. P. Cuautle and R. Valenzuela, "Impedance spectroscopy studies of Ni-Zn ferrites," *Materials Science and Engineering*, **B49**, 221 (1997).

[23] T. Tsutaoka, M. Ueshima, T. Tokunaga, T. Nakamura and K. Hatakeyama, "Frequency dispersion and temperature variation of complex permeability of Ni-Zn ferrite composite materials," *J. Appl. Phys.*, **78(6)**, 3983 (1995).

[24] Shannon A. Morrison, Christopher L. Cahill, Everett E. Carpenter, Scott Calvin, Raja Swaminathan and Michael E. McHenry, Vincent G. Harris, " Magnetic and structural properties of nickel zinc ferrite nanoparticles sythesized at room temperature," *J. Appl. Phys.*, **95(11)**, 6392 (2004).

[25] S. T. Mahmud, A. K. M. Akther Hossain, A. K. M. Abdul Hakim, M. Seki, T. Kawai and H. Tabata, "Influence of microstructure on the complex permeability of spinel type Ni-Zn ferrite," *J. Magn. Magn. Mater.*, **305**, 269 (2006).

[26] Ovidiu F. Caltun, Leonard Spinu, Alexandru Sraneu, " Magnetic properties of High frequency Ni-Zn ferrites Doped with CuO," *IEEE Trans. Magn.*, **37(4)**, 2353, (2001).

[27] Takanori Tsutaoka, " Frequency dispersion of complex permeability in Mn-Zn and Ni-Zn spinel ferrites and their composite materials," *J. Appl. Phys.*, **93(5)**, 2789.(2003).

[28] S. T. Mahmud "Study of microstructure and its effect on the complex permeability of Ni-Zn ferrite," *M. Phil. Thesis*, BUET, Bangladesh (2006).

[29] K.K.Kabir "Preparation and investigation of frequency dependence permeability of Co-Zn ferrite," *M. Phil. Thesis*, BUET, Bangladesh (2007).

[30] T.S. Biswas "Influence of Mg and Cr substitution on structural and magnetic properties of polycrystalline $Ni_{0.70}Zn_{0.30-x-y}Mg_xCr_yFe_2O_4$," *M. Phil. Thesis*, BUET, Bangladesh (2008).

[31] T. Nakamura "Low temperature sintering of Ni-Zn-Cu ferrite and its permeability spectra," *J. Magn. Magn. Mater.*, **168**, 285 (1997).

CHAPTER 2

LITERATURE REVIEW

Double oxides of iron and other metals are important members of ferrimagnetic system commonly known as ferrites. The outstanding properties of ferrites are their complex magnetic structure, which can be varied to tailor their magnetic properties for various high frequency applications. In this chapter we describe a brief overview of the ferrites. The basic issue of ferrimagnetism, crystal structure of the spinel ferrites and effect of non-magnetic Zn substitution on the magnetic moments in spinel ferrites are discussed. A few theoretical aspects of complex permeability are also discussed

2.1 Overview of the materials

Ferrites commonly expressed by the general chemical formula $MeO.Fe_2O_3$, where *Me* represents divalent metals, first commanded the public attention when Hilpert (1909) focused on the usefulness of ferrites at high frequency [1]. A systematic investigation was launched by Snoek (1936) at Philips Research Laboratory [2] At the same time Takai (1937) in Japan was seriously engaged in the research work on the same materials [1]. Snoek's extensive works on ferrites unveiled many mysteries regarding magnetic properties of ferrites. He was particularly looking for high permeability materials of cubic structure. This particular structure for symmetry reasons supports low crystalline anisotropy He found suitable materials in the form of mixed spinels of the type $MeZnFe_2O_4$, where *Me* stands for metals like *Cu*, *Mg*, *Ni*, *Co* or *Mn*, for which permeability were found to be up to 4000 [1-3]. Here after starts the story of *Ni-Zn* ferrites. Remarkable properties like high permeability, low loss factor, high stability of permeability with temperature and time, high wear resistance, controlled coercive force, low switching coefficient etc. have aptly placed *Ni-Zn* ferrites as highly demandable ferrites to both researchers and manufacturers. Every year great deals of paper are being published on various aspects of *Ni-Zn* ferrites. A large number of scientists and technologists are engaged in research to bring about improvements on the magnetic properties of *Ni-Zn* ferrites

The sintering process is considered to be one of the most vital steps in ferrite preparation and often plays a dominant role in many magnetic properties. Tasaki *et al.* [4]

studied the effect of sintering atmosphere on permeability of sintered ferrite. They found that high density is one of the factors. which contribute to greater permeability. However, permeability decreased in an atmosphere without O_2 at high sintering temperature where high density was expected. This decrease in permeability is attributed to the variation of chemical composition caused by volatilization of *Zn*. At low sintering temperature a high permeability is obtained in an atmosphere without O_2 because densification and stoichiometry plays a principal role in increasing permeability At high sintering temperature the highest permeability is obtained in the presence of O_2 because the effect of decrease of *Zn* content can then be neglected.

Studying the electromagnetic properties of ferrites, Nakamura [5] suggested that both the sintering density and the average grain size increased with sintering temperature. These changes were responsible for variations in magnetization, initial permeability and electrical resistivity

High permeability attainment is certainly affected by the microstructure of the ferrites. Roess showed that [6] the very high permeability is restricted to certain temperature ranges and the shapes of permeability versus temperamre curves are strongly affected by any inhomogeneity in the ferrite structure.

Rezlescu *et al.* [8] reported that the sintering behaviour and microstructure of the ferrites samples largely affected by *PbO* addition. *PbO* significantly reduced the sintering temperatures, thus energy consumption is minimized and material loss by evaporation is minimized [9].

Calmn [10] studied magnetic properties of high frequency Ni-Zn ferrites doped with CuO.Upon increasing the the Cu substitution ,the average grain size decreases and the microstructure becomes more umform with fewer pores.initial permeability was higher for higher Cu content Chul Sung Kim [11] studied the structure of Cu-doped NiZn ferrite.The Lattice parameter increases linearly with Cu content.

Rahman[12] studied on Ni-Cu-Zn based ferrites .Average crystallite size increase linearly with calcined temperature.The lattice parameter and the ionoc radious of the octahedral sites increases with copper content.The saturation magnetization decreases with increasing non-magnetic Cu content. Woo Chul Kim [13] studied growth of

ultrafine NiCuZn ferrite and magnetic properties by sol-gel method.The saturation magnetization increases drastically with annealing temperature.

Nakamura [14] reported on low temperature sintering Ni-Cu-Zn ferrite and its permeability spectra The complex permeability of the sintering ferrites is describe as the summation of the spin rotational contribution and domain wall motion componet.The permeability in 100MHz region is determined mainly by the spin rotation magnetization mechanism and it depends only on the post sintering density The effect of domain wall contribution cannot be ignored in the 10MHz region. The domain wall contribution can be controlled not only by the post sintering density but also by the ferrites grain size.

Caltun [15] studied the microstructure and of the permeability spectra of NiCuZn ferrites. The particle size increase when the sintering temperature is raised. For the same composition and different sintering temperature permeability in low frequency region decreases by addition of CuO. As the sintering temperature increases natural resonance frequency shifted towards lower frequency.Aminul Islam[16] studied the microstructral effect of the magnetic and electrical properties of NiCuZn ferrites Lattice parameter increases with increasing Cu content. Grain size increases with increasing Cu content and sintering temperature. Saturation magnetization decreases and initial permeability increases with increasing copper content.

There are two mechanisms in the phenomenon of permeability; spin rotation in the magnetic domains and wall displacements. The uncertainty of contribution from each of the mechanisms makes the interpretation of the experimental results difficult. Globus [17] shows that the intrinsic rotational permeability μ_r and 180^0 wall permeability μ_w may be written as: $\mu_r = 1 + 2\pi M_s^2 / K$ and $\mu_w = 1 + 3\pi M_s^2 D / 4\gamma$, where M_s is the saturation magnetization, K is the total anisotropy. D is the grain diameter and $\gamma = K\delta_w$ is the wall energy.

M. A. Ahmed et al [18] studied the DC, AC electrical resistivity of $Zn_{0.80}Ni_{0.20}Fe_2O_4$ ferrites. The DC electrical resistivity (ρ_{dc}) decreases as temperature (T) of the sample increases This decrease in the resistivity is due to the semiconductive behavior of the studied composition $Zn_{0.80}Ni_{0.20}Fe_2O_4$ which is controlled by the form $\rho_{dc} = \rho_o exp(E/k_BT)$, where ρ_o is the resistivity at infinitely high temperature, k_B is Boltzmann's constant and E is the activation energy in eV for electrical conductions. The frequency

dependence of the real AC electrical conductivity ($\sigma'_{ac}(\omega)$) increases as the frequency of the applied electric field increases. The relationship between the real AC electrical conductivity and the frequency can be written as $\sigma'_{ac}(\omega)=B\omega^n$, where B and n are constants which depend on both the temperature and composition and $\omega=2\pi f$ is the angular frequency.

2.2 Magnetic ordering

The onset of magnetic order in solids has two basic requirements:

(i) Individual atoms should have magnetic moments (spins),

(ii) Exchange interactions should exist that couple them together.

Magnetic moments originate in solids as a consequence of overlapping of the electronic wave function with those of neighboring atoms. This condition is best fulfilled by some transition metals and rare-earths. The exchange interactions depend sensitively upon the inter-atomic distance and the nature of the chemical bonds, particularly of nearest neighbour atoms. When the positive exchange dominates, which corresponds to parallel coupling of neighbouring atomic moments (spins), the magnetic system becomes ferromagnetic below a certain temperature T_C called the Curie temperature. The common spin directions are determined by the minimum of magneto-crystalline anisotropy energy of the crystal. Therefore, ferromagnetic substances are characterized by spontaneous magnetization. But a ferromagnetic material in the demagnetized state displays no net magnetization in zero field because in the demagnetized state a ferromagnetic of macroscopic size is divided into a number of small regions called domains, spontaneously magnetized to saturation value and the directions of these spontaneous magnetization of the various domains are such that the net magnetization of the specimen is zero. The existence of domains is a consequence of energy minimization. The size and formation of these domains is in a complicated manner dependent on the shape of the specimen as well as its magnetic and thermal history. When negative exchange dominates, adjacent atomic moments (spins) align antiparallel to each other, and the substance is said to be anti-ferromagnetic below a characteristic temperature, T_N, called the Néel temperature. In the simplest case, the lattice of an anti-ferromagnet is divided into two sublattices with the magnetic moments of these in anti-parallel alignment. This result is zero net magnetization. A special case of anti-ferromagnetism is ferrimagnetism. In

ferrimagnetism, there are also two sublattices with magnetic moments in opposite directions, but the magnetization of the sublattices are of unequal strength resulting in a non-zero magnetization and therefore has net spontaneous magnetization. At the macroscopic level of domain structures, ferromagnetic and ferrimagnetic materials are therefore similar.

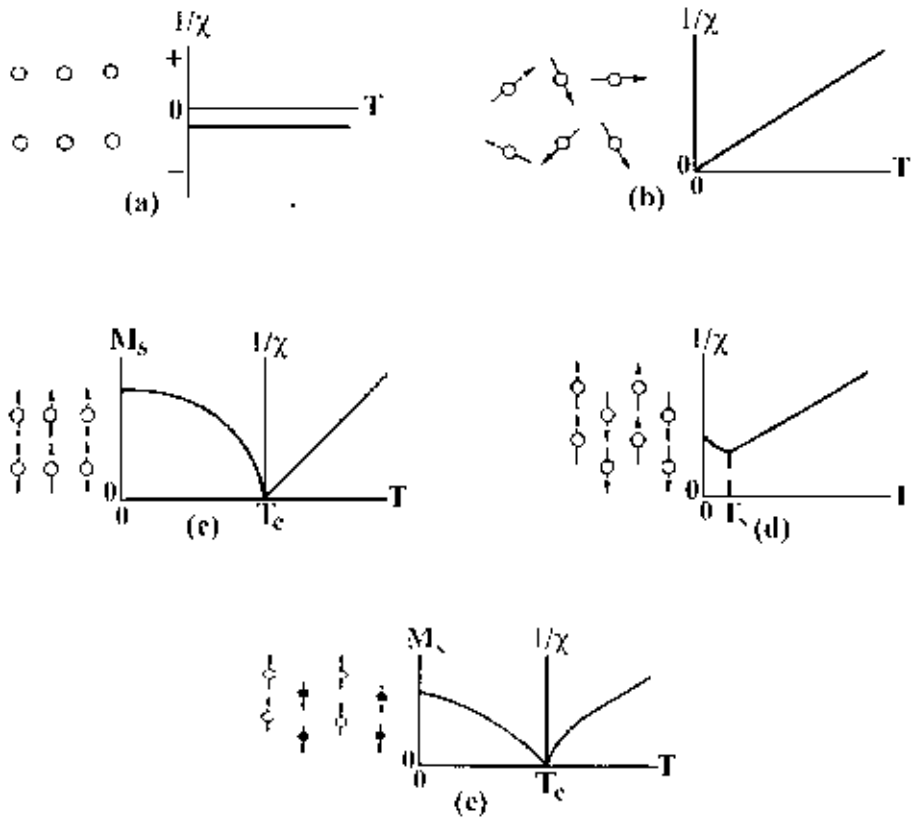

Figure 2.1. Temperature dependence of the inverse susceptibility for (a) a diamagnetic material, (b) a paramagnetic material, showing Curie's law behaviour, (c) a ferromagnetic material, showing a spontaneous magnetization for $T<T_C$ and Curie-Weiss behaviour for $T>T_C$; (d) an antiferromagnetic material; (e) a ferrimagnetic material, showing a net spontaneous magnetization for $T<T_C$ and non linear behaviour for $T>T_C$.

The Curie and Néel temperatures characterize a phase transition between the magnetically ordered and disordered (paramagnetic) states. From these simple cases of magnetic ordering various types of magnetic order exists, particularly in metallic substances. Because of long-range order and oscillatory nature of the exchange

interaction, mediated by the conduction electrons, structures like helical, conical and modulated patterns might occur. A useful property for characterizing the magnetic materials is the magnetic susceptibility, χ, defined as the magnetization, M, divided by the applied magnetic field, H i.e. $\chi = M / H$ The temperature dependence of susceptibility or more accurately, inverse of susceptibility is a good characterization parameter for magnetic materials; Fig. 2.1(e) shows that in the paramagnetic region, the variation of the inverse susceptibility with temperature of a ferrite material is decidedly non-linear. Thus the ferrite materials do not obey the Curie-Weiss law, $\chi = C/(T - T_c)$ [2, 19].

2.3 Crystal structure of spinel ferrites

Ferrites have the cubic structure, which is very close to that of the mineral spinel $MgO.Al_2O_3$, and are called cubic spinel. Analogous to the mineral spinel, magnetic spinel have the general formula $MeO\ Fe_2O_3$ or $MeFe_2O_4$ where Me is the divalent metal ion [20]. This crystal structure was first determined by Bragg and by Nishikawa [1,19]. Formerly, spinels containing Fe were called ferrites but now the term has been broadened to include many other ferrimagnets including garnets and hexagonal ferrites these need not necessarily contain iron. The spinel lattice is composed of a close-packed oxygen (radius about 1.3Å) arrangement in which 32 oxygen ions form a unit cell that is the smallest repeating unit in the crystal network. The unit cell of the ideal spinel structures is given in Fig. 2.2. Between the layers of oxygen ions, if we simply visualize them as spheres, there are interstices that may accommodate the metal ions (radii ranging from 0.6 to 0.8Å). Now, the interstices are not all the same: some which we call A sites are surrounded by or coordinated with 4 nearest neighboring oxygen ions whose lines connecting their centers form a tetrahedron. Thus, A sites are called tetrahedral sites. The other type of sites (B sites) is coordinated by 6 nearest neighbor oxygen ions whose center connecting lines describe an octahedron. The B sites are called octahedral sites. In the unit cell of 32 oxygen ions there are 64 tetrahedral sites and 32 octahedral sites. If all these were filled with metal ions, of either +2 or +3 valence, the positive charge would be very much greater than the negative charge and so the structure would not be electrically neutral. It turns out that of the 64 tetrahedral sites, only 8 are occupied and out of 32 octahedral sites, only 16 are occupied. Thus the unit cell contains eight formula units

AB_2O_4, with 8 *A* sites, 16 *B* sites and 32 oxygen ions. and total of 8 x 7 = 56 ions. A spinel unit cell contains two types of subcells, Fig 2.2. The two types of subcells alternate in a three-dimensional array so that each fully repeating unit cell requires eight subcells, Fig. 2.3.

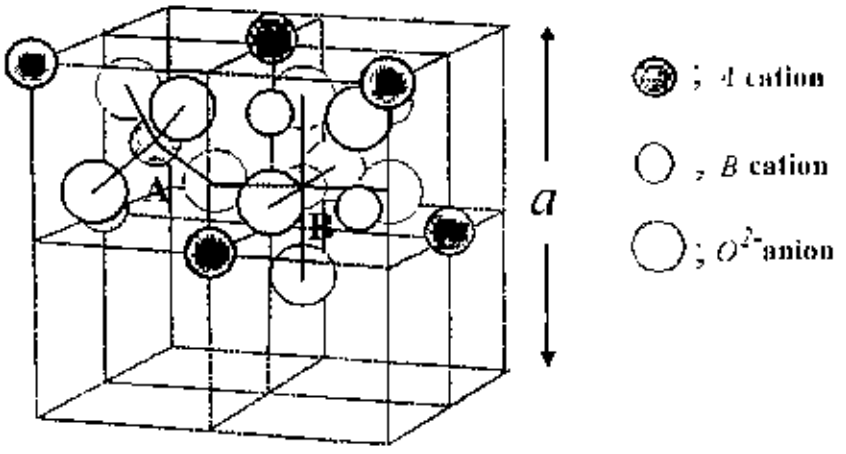

Figure 2.2. Two subcells of a unit cell of the spinel structure.

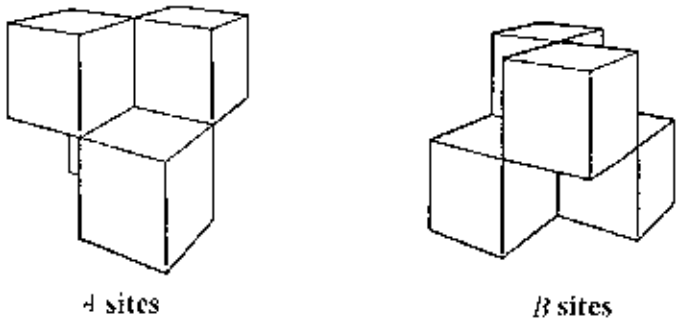

Figure 2.3. Unit cell of spinel ferrite divided into eight subcells with *A* and *B* sites

The positions of the ions in the spinel lattice are not perfectly regular (as the packing of hard spheres) and some distortion does occur. The tetrahedral sites are often too small for the metal ions so that the oxygen ions move slightly to accommodate them. The oxygen ions connected with the octahedral sites move in such a way as to shrink the size the octahedral cell by the same amount as the tetrahedral site expands. The movement of the tetrahedral oxygen is reflected in a

quantity called the oxygen parameter, which is the distance between the oxygen ion and the face of the cube edge along the cube diagonal of the spinel subcell. This distance is theoretically equal to $3/8a_0$ where a_0 is the lattice constant [1]

2.4 Cation distribution of spinel ferrites

In spinel structure the distribution of cations over the tetrahedral or *A* sites and octahedral or *B* sites can be present in a variety of ways. If all the Me^{2+} ions in $Me^{2+}Me_2^{3+}O_4$ are in tetrahedral and all Me^{3+} ions in octahedral positions, the spinel is then called normal spinel. Another cation distribution in spinel exists, where one half of the cations Me^{3+} are in the *A* positions and the rest, together with the Me^{2+} ions are randomly distributed among the *B* positions The spinel having the latter kind of cation distribution is known as inverse spinel. The distribution of these spinels can be summarized as [2, 21-22]:

1) Normal spinels, i.e. the divalent metal ions are on *A*-sites: $Me^{2+}[Me_2^{3+}]O_4$,

2) Inverse spinels, i.e. the divalent metal ions are on *B*-sites: $Me^{3+}[Me^{2+}Me_2^{3+}]O_4$

A completely normal or inverse spinel represents the extreme cases. *Zn* ferrites have normal spinel structure and its formula may be written as $Zn^{2+}[Fe^{3+}Fe^{3+}]O_4^{2-}$. On the other hand, *Ni* ferrites have inversel spinel structure and its formula may be written as $Fe^{3+}[Ni^{2-}Fe^{3+}]O_4^{2-}$. There are many spinel oxides which have cation distributions intermediate between these two extreme cases and are called mixed spinels. The general cation distribution for the spinel can be indicated as:

$$(Me_x^{2+}Me_{1-x}^{3-})[Me_{1-x}^{2+}Me_{1+x}^{3+}]O_4$$

where the first and third brackets represent the A and B sites respectively. For normal spinel x=1, for inverse spinel x=0. The quantity x is a measure of the degree of inversion. In the case of some spinel oxides x depends upon the method of preparation.

The basic magnetic properties of the ferrites are very sensitive functions of their cation distributions. Mixed ferrites having interesting and useful magnetic properties are prepared by mixing two or more different types of metal ions. The chemical formula of mixed *Ni-Zn* ferrite may be written as $(Zn_{1-x}^{2+}Fe_x^{3+})[Ni_x^{2+}Fe_{2-x}^{3+}]O_4^{2-}$ where $0 \le x \le 1$.

Spinel oxides are ionic compounds and hence the chemical bonding occurring in them can be taken as purely ionic to a good approximation. The total energy involved, however, consists of the Coulomb energy, the Born repulsive energy, the polarization and the magnetic interaction energy. The energy terms are all dependent on lattice constant, oxygen position parameter and the ionic distribution. In principle the equilibrium cation distribution can be calculated by minimizing the total energy with respect to these variables. But the only energy that can be written with any accuracy is the Coulomb energy The individual preference of some ions for certain sites resulting from their electronic configuration also play an important role. The divalent ions are generally larger than the trivalent (because the larger charge produces greater electrostatic attraction and so pulls the outer orbits inward). The octahedral sites are also larger than the tetrahedral. Therefore, it would be reasonable that the trivalent ions Fe^{3+} (0.67Å) would go into the tetrahedral sites and the divalent ions Fe^{2+} (0.83Å) go into the octahedral. Two exceptions are found in Zn^{2+} and Cd^{2+} which prefer tetrahedral sites because the electronic configuration is favourable for tetrahedral bonding to the oxygen ions. Thus Zn^{2-} (0.74Å) prefer tetrahedral sites over the Fe^{3-} (0.67Å) ions. Zn^{2+} (0.74Å) and Ni^{2+} (0.74Å) have almost the same ionic radius but *Zn* prefers tetrahedral sites and *Ni* prefers octahedral sites because of the configuration exception. Ni^{2+} (0.78Å) and Cr^{3+} (0.64Å) have strong preferences for octahedral sites. Hence the factors influencing the distribution the cations among the two possible lattice sites are mainly their ionic radii of the specific ions, the size of the interstices, temperature, the matching of their electronic configuration to the surrounding anions and the electrostatic energy of the lattice, the so-called Madelung energy, which has the predominant contribution to the lattice energy under the constrain of overall energy minimization and charge neutrality.

2.5 Interaction between magnetic moments on lattice sites

Spontaneous magnetization of spinels (at 0K) can be estimated on the basis of their composition, cation distribution, and the relative strength of the possible interaction. Since cation-cation distances are generally large, direct (ferromagnetic) interactions are negligible. Because of the geometry of orbital involved, the strongest superexchange interaction is expected to occur between octahedral and tetrahedral cations. The strength of interaction or exchange force between the moments of the two metal ions on different

sites depends on the distances between these ions and the oxygen ion that links them and also on the angle between the three ions. The nearest neighbours of a tetrahedral, an octahedral and an anion site are shown in Fig. 2.4. The interaction is greatest for an angle of 180^0 and also where the interionic distances are the shortest Fig. 2.5 shows the interionic distances and the angles between the ions for the different type of interactions. In the *A-A* and *B-B* cases, the angles are too small or the distances between the metal ions and the oxygen ions are too large. The best combination of distances and angles are found in *A-B* interactions.

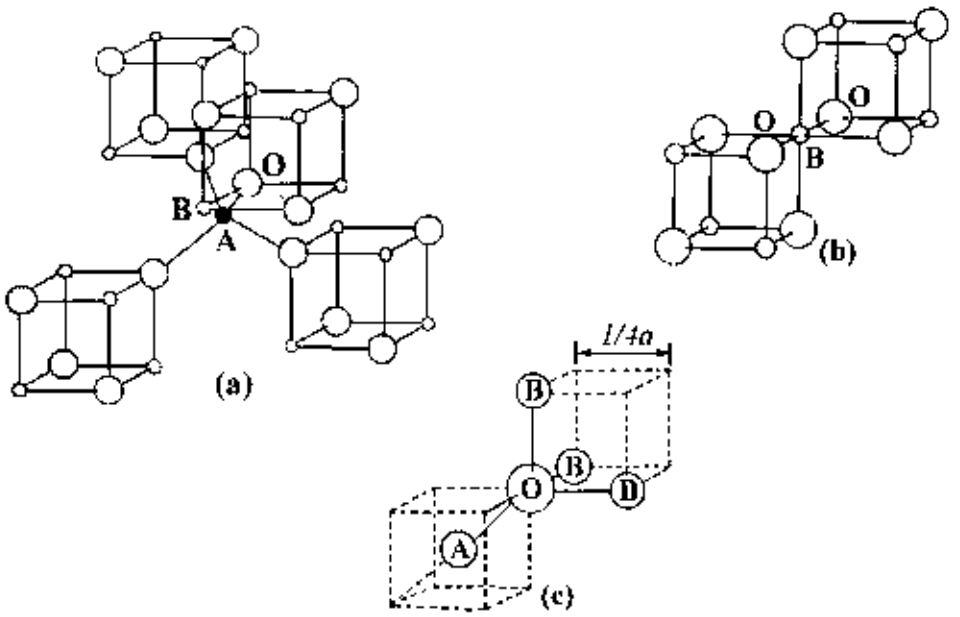

Figure 2.4. Nearest neighbours of (a) a tetrahedral site, (b) an octahedral site and (c) an anion site

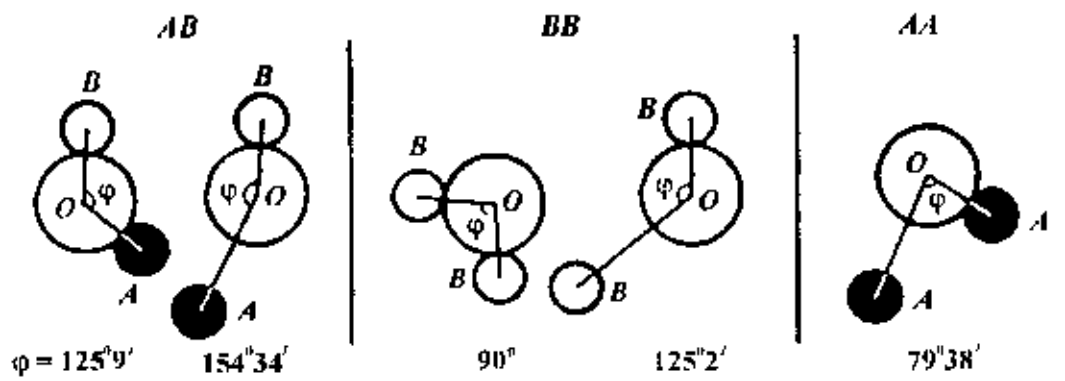

Figure 2.5. Interionic angles in the spinel structure for the different type of lattice site interactions.

For an undistorted spinel, the *A-O-B* angles are about 125^0 and 154^0 [1-2, 23] The *B-O-B* angles are 90^0 and 125^0 but the latter, one of the *B-B* distances is large In the *A-A* case the angle is about 80^0. Therefore, the interaction between moments on the *A* and *B* site is strongest. The *BB* interaction is much weaker and the most unfavorable situation occurs in the *AA* interaction. By examining the interaction involving the major contributor, or the *A-B* interaction which orients the unpaired spins of these ions antiparallel, Néel was able to explain the ferrimagnetism of ferrites.

2.6 Magnetism in spinel ferrite

The magnetic moment of a free atom is associated with the orbital and spin motions of electrons in an incomplete sub-shell of the electronic structure of the atom. In crystals the orbital motions are quenched, that is the orbital planes may be considered to be fixed in space relative to the crystal lattice, and in such a way that in bulk the crystal has no resultant moment from this source Moreover this orbital-lattice coupling is so strong that the application of a magnetic field has little effect upon it. The spin axes are not tightly bound to the lattice as are the orbital axes. The anions surrounding a magnetic cation subject it to a strong inhomogeneous electric field and influence the orbital angular momentum. However, the spin angular momentum remains unaffected. For the first transition group elements this crystal field effect is intense partly due to the large radius of the 3d shell and partly due to the lack of any outer electronic shell to screen the 3d shell whose unpaired electrons only contribute to the magnetic moment. We have originally defined the magnetic moment in connection with permanent magnets. The electron itself may well be called the smallest permanent magnet [1]. For an atom with a resultant spin quantum number *S*, the spin magnetic moment will be

$$\mu = g\sqrt{S(S+1)}\mu_B$$

where g is the Landé splitting factor and μ_B, known as the Bohr magneton, is the fundamental unit of magnetic moment. The value of g for pure spin moment is 2 and the quantum number associated with each electron spin is $\pm 1/2$. The direction of the moment is comparable to the direction of the magnetization (from South to North poles) of a permanent magnet to which the electron is equivalent. Fig. 2.6 illustrates the electronic configuration of Fe atoms and Fe^{3+} ions. Fe atom has four unpaired electrons and Fe^{3+} ion has five unpaired

electrons. Each unpaired electron spin produced 1 Bohr magneton. In compounds, ions and molecules, account must be taken of the electrons used for bonding or transferred in ionization. It is the number of unpaired electrons remaining after these processes occur that gives the net magnetic moment [1]. According to the Hund's rules the moment of Fe atom and Fe^{3+} ion are $4\mu_B$ and $5\mu_B$ respectively. Similarly the moment of Fe^{2+} and Ni^{2+} ion are $4\mu_B$ and $3\mu_B$ respectively.

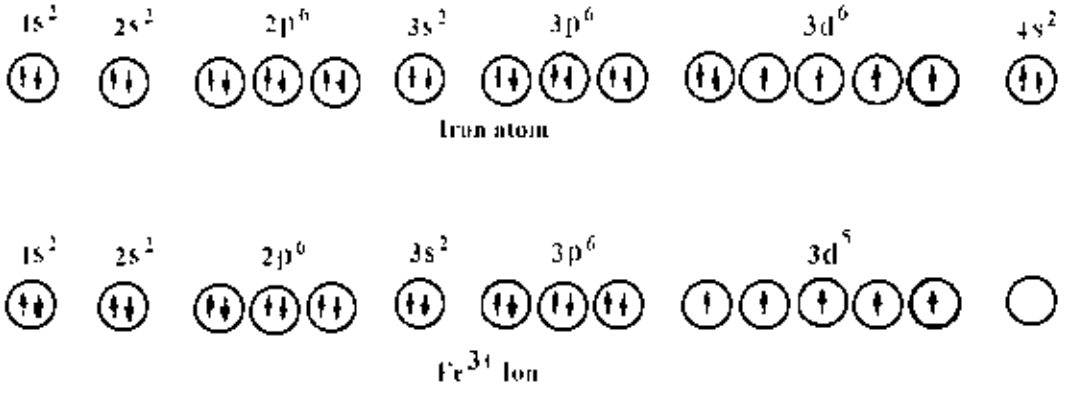

Figure 2.6. Electronic configuration of atoms and ions

2.6.1 Exchange interactions in spinel

The intense short-range electrostatic field, which is responsible for the magnetic ordering, is the exchange force that is quantum mechanical in origin and is related to the overlapping of total wave functions of the neighbouring atoms. The total wave function consists of the orbital and spin motions. Usually the net quantum number is written as S, because the magnetic moments arise mostly due to the spin motion as described above. The exchange interactions coupling the spins of a pair of electrons are proportional to the scalar product of their spin vectors [20, 22, 24],

$$V_{ij} = -2J_{ij}\vec{S}_i.\vec{S}_j \tag{2.1}$$

where J_{ij} is the exchange integral given in a self explanatory notation by

$$J_{ij} = \int \psi_i^*(1)\psi_j^*(2)\left[\frac{1}{r_{12}} + \frac{1}{r_{ij}} - \frac{1}{r_{i1}} - \frac{1}{r_{j2}}\right]\psi_i(1)\psi_j(2)dv_1dv_2 \tag{2.2}$$

In this expression r's are the distances, subscripts i and j refer to the atoms, 1 and 2 refers to the two electrons. If the J in equation (2.1) is positive, we achieve ferromagnetism. A negative J may give rise to anti-ferromagnetism or ferrimagnetism.

Magnetic interactions in spinel ferrites as well as in some ionic compounds are different from the one considered above because the cations are mutually separated by bigger anions (oxygen ions). These anions obscure the direct overlapping of the cation charge distributions, sometimes partially and some times completely making the direct exchange interaction very weak. Cations are too far apart in most oxides for a direct cation-cation interaction. Instead, superexchange interactions appear, i.e., indirect exchange via anion p-orbitals that may be strong enough to order the magnetic moments. Apart from the electronic structure of cations this type of interactions strongly depends on the geometry of arrangement of the two interacting cations and the intervening anion. Both the distance and the angles are relevant. Usually only the interactions with in first coordination sphere (when both the cations are in contact with the anion) are important. In the Neél theory of ferrimagnetism the interactions taken as effective are inter- and intra-sublattice interactions A-B, A-A and B-B. The type of magnetic order depends on their relative strength.

The superexchange mechanism between cations that operate via the intermediate anions was proposed by Kramer for such cases and was developed by Anderson and Van Vleck [21, 22]. A simple example of superexchange is provided by MnO which was chosen by Anderson. From the crystal structure of MnO it will be seen that the antiparallel manganese ions are collinear with their neighbouring oxygen ions. The O^{2-} ions each have six $2p$ electrons in three antiparallel pairs. The outer electrons of the Mn^{2+} ions are in $3d$ sub-shells which are half filled with five electrons in each. The phenomenon of superexchange is considered to be due to an overlap between the manganese $3d$ orbits and the oxygen $2p$ orbits with a continuous interchange of electrons between them. It appears that, for the overall energy of the system to be a minimum, the moments of the manganese ions on either side of the oxygen ion must be antiparallel. The manganese magnetic moments are thus, in effect, coupled through the intervening oxygen ion. The idea is illustrated in Fig. 2.7.

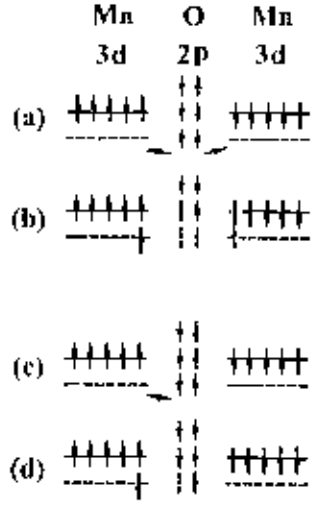

Figure 2.7. Illustrating superexchange in *MnO*.

In Figs. 2.7(a) and 2.7(c) the outer electrons in a pair of Mn^{2+} ions, and in an intervening O^{2-} ion in the unexcited state, are shown by the arrows. One suggested mode of coupling is indicated in Fig. 2.7(b). The two electrons of a pair in the oxygen ion are simultaneously transferred, one to the left and the other to the right. If their directions of spin are unchanged then, by Hund's rules, the moments of the two manganese ions must be antiparallel as shown. Another possibility is represented in Fig. 2.7(d). One electron only has been transferred to the manganese ion on the left. The oxygen ion now has a moment of $1\mu_B$ and if there is negative interaction between the oxygen ion and the right-hand manganese ion then again the moments of the manganese ions will be antiparallel. If these ideas are accepted then the oxygen ions play an essential part in producing antiferromagnetism in the oxide. Moreover, because of the dumbbell shape of the *2p* orbits, the coupling mechanism should be most effective when the metal ions and the oxygen ions lie in one straight line, that is, the angle between the bonds is 180°, and this is the case with *MnO*.

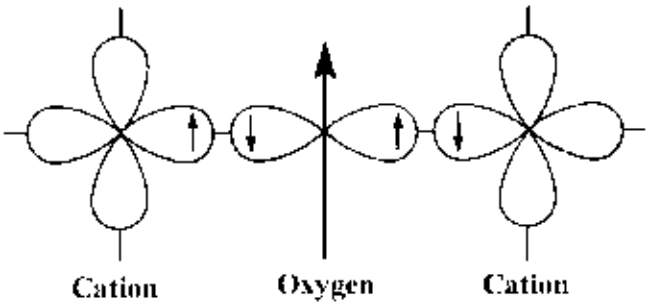

Figure 2.8. Schematic representation of the superexchange interaction in the magnetic oxides. The *p* orbital of an anion (center) interact with the *d* orbitals of the transitional metal cations.

In the case of spinel ferrites the coupling is of the indirect type which involves overlapping of oxygen wave functions with those of the neighboring cations. Consider two transition metal cations separated by an O, Fig. 2.8. The O^{2-} has no net magnetic moment since it has completely filled shells, with *p*-type outermost orbitals. Orbital p_x has two electrons: one with spin up, and the other with spin down, consistent with pauli's exclusion principle. The essential point is that when an oxygen *p* orbital overlaps with a cation *d* orbital, one of the *p* electrons can be accepted by the cations. When one of the transition-metal cations is brought close the O^{2-}, partial electron overlap (between a *3d* electron from the cation and a *2p* electron form the O^{2-}) can occur only for antiparallel spins, because electrons with the same spin are repelled. Empty *3d* states in the cation are available for partial occupation by the O^{2-} electron, with an antiparallel orientation. Electron overlap between the other cation and the O^{2-} then occurs resulting in antiparallel spins and therefore antiparallel order between the cations. Since the *p* orbitals are linear, the strongest interaction is expected to take place for *cation*–O^{2-}–*cation* angles close to 180^0 [2]

2.6.2 Néel theory of ferrimagnetism

If we consider the simplest case of a two-sublattice system having antiparallel and non-equal magnetic moments, the inequality may be due to:

1) different elements in different sites,
2) same element in different ionic states, and

3) different crystalline fields leading to different effective moments for ions having the same spin.

The spins on one sublattice are under the influence of exchange forces due to the spins on the second sublattice as well as due to other spins on the same sublattice. The molecular fields acting on the two sublattices A and B can be written as [2, 19-24]

$$\vec{H}_A = \lambda_{AA}\vec{M}_A + \lambda_{AB}\vec{M}_B,$$

$$\vec{H}_B = \lambda_{AB}\vec{M}_A + \lambda_{BB}\vec{M}_B$$

where $\vec{M}_A$ and $\vec{M}_B$ are the magnetizations of the two sublattices and λ's are the Weiss constants. Since the interaction between the sublattices is antiferromagnetic, λ_{AB} must be negative, but λ_{AA} and λ_{BB} may be negative or positive depending on the crystal structure and the nature of the interacting atoms. Probably, these interactions are also negative, though they are in general quite small.

Assuming all the exchange interactions to be negative the molecular fields will be then given by

$$\vec{H}_A = -\lambda_{AA}\vec{M}_A - \lambda_{AB}\vec{M}_B,$$

$$\vec{H}_B = -\lambda_{AB}\vec{M}_A - \lambda_{BB}\vec{M}_B$$

Since in general, λ_{AA} and λ_{BB} are small compared to λ_{AB}, it is convenient to express the strengths of these interactions relative to the dominant λ_{AB} interaction.

Let $\lambda_{AA} = \alpha\lambda_{AB}$

and $\lambda_{BB} = \beta\lambda_{AB}$

In an external applied field $\vec{H}$, the fields acting on A and B sites are

$$\vec{H}_A = \vec{H} - \lambda_{AB}(\alpha\vec{M}_A - \vec{M}_B),$$

$$\vec{H}_B = \vec{H} - \lambda_{AB}(\vec{M}_A - \beta\vec{M}_B)$$

At temperatures higher than the transition temperature, T_N, $\vec{H}_A$, $\vec{M}_A$ and $\vec{M}_B$ are all parallel and we can write

$$\vec{M}_A = \frac{C_A}{T}[\vec{H} - \lambda_{AB}(\alpha\vec{M}_A - \vec{M}_B)], \qquad (23)$$

$$\vec{M}_B = \frac{C_B}{T}[\vec{H} - \lambda_{AB}(\vec{M}_A - \beta\vec{M}_B)] \tag{2.4}$$

where C_A and C_B are the Curie constants for the two sublattices.

$$C_A = N_A g\mu_B^2 S_A(S_A+1)/3K$$

and $$C_B = N_B g\mu_B^2 S_B(S_B+1)/3K$$

N_A and N_B denote the number of magnetic ions on A and B sites respectively and S_A and S_B are their spin quantum numbers. Solving for the susceptibility, χ, one gets [2, 19]

$$\frac{1}{\chi} = \frac{T}{C} - \frac{1}{\chi_0} - \frac{b}{T-\theta}$$

$$\frac{1}{\chi} = \frac{T+(C/\chi_0)}{C} - \frac{b}{T-\theta} \tag{2.5}$$

where C, χ_0, b and θ are constants for particular substance and are given by

$$C = C_A + C_B$$

$$\frac{1}{\chi_0} = -\frac{1}{C^2}[C_A^2\lambda_{AA} + C_B^2\lambda_{BB} + 2C_AC_B\lambda_{AB}]$$

$$b = \frac{C_AC_B}{C^3}[C_A^2(\lambda_{AA}-\lambda_{BB})^2 + C_B^2(\lambda_{BB}-\lambda_{AB})^2$$
$$-2C_AC_B\{\lambda_{AB}^2 - (\lambda_{AA}+\lambda_{BB})\lambda_{AB} + \lambda_{AA}\lambda_{BB}\}]$$

$$\theta = -\frac{C_AC_B}{C}(\lambda_{AB}+\lambda_{BB}) - 2\lambda_{AB}$$

Equation (2.5) represents a hyperbola, and the physically meaning part of it is plotted in Fig. 2.9. This curvature of the plot of $1/\chi$ versus T is a characteristics feature of a ferrimagnet. It cuts the temperature axis at T_c, called the Ferrimagnetic Curie point. At high temperatures the last term of equation (2.5) become negligible, and reduces to a Curie-Weiss law

$$\chi = \frac{C}{T+(C/\chi_0)}$$

This is the equation of straight line, shown dashed in Fig. 2.9, to which the $1/\chi$ versus T curve becomes asymptotic at high temperatures.

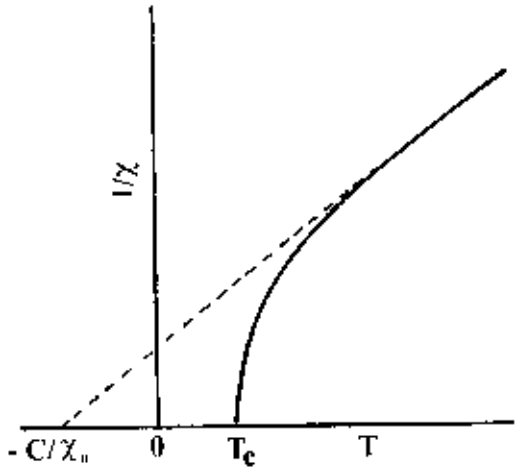

Figure 2.9. The temperature dependence of the inverse susceptibility for ferrimagnets.

The Ferrimagnetic Curie temperature T_C is obtained from equations (2.3) and (2.4) with $H = 0$ and setting the determinant of the coefficients of M_f equal to zero. This gives

$$T_C = \frac{1}{2}[C_A\lambda_{AA} + C_B\lambda_{BB} + \{(C_A\lambda_{AA} - C_B\lambda_{BB})^2 + 4C_AC_B\lambda_{AB}^2\}^2] \qquad (2.6)$$

Equation (2.5) is in good agreement with the experiment, except near the Curie point. The experimental Curie temperature, the temperature at which the susceptibility becomes infinite and spontaneous magnetization appears, is lower than the theoretical Curie temperature [19]. This disagreement between theory and experiment in the region of Curie point is presumably due to the short-range spin order (spin clusters) at temperatures above experimental T_C [2, 19].

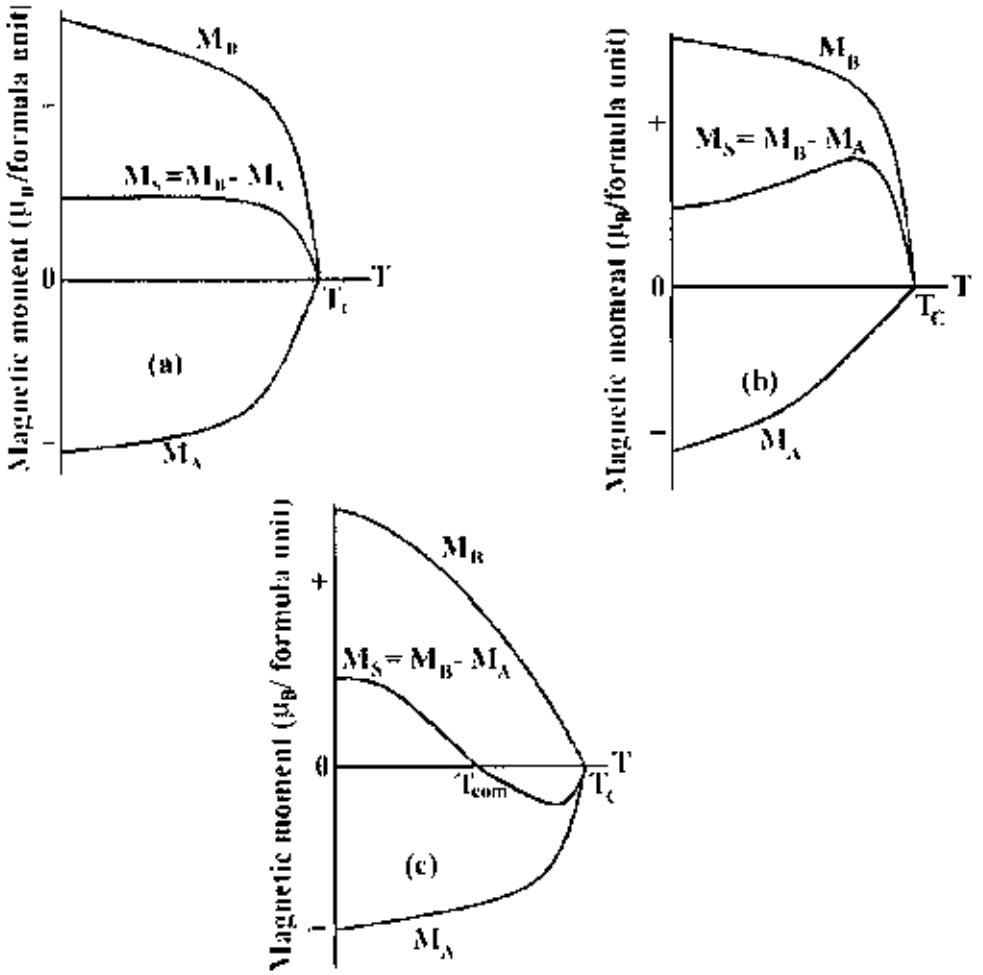

Figure 2.10. Superposition of various combinations of two opposing sublattice magnetizations producing differing resultants including one with a compensation point (schematic).

The sublattice magnetizations will in general have different temperature dependences because the effective molecular fields acting on them are different. This suggests the possibility of having anomaly in the net magnetization versus temperature curves, Fig. 2.10. For most ferrimagnets the curve is similar to that of ferromagnets, but in a few cases there be a compensation point in the curve, Fig. 2.10(c) [1, 19]. At a point below the Curie temperature point, the two sublattice magnetizations are equal and thus appear to have no moment. This temperature is called the compensation point. Below this temperature one sublattice magnetization is larger and provides the net moment. Above this temperature the other magnetization does dominates and the net magnetization reverses direction.

The essential requisite for Néel configuration is a strong negative exchange interaction between *A* and *B* sublattices which results in their being magnetized in opposite directions below the transition point. But there may be cases where intrasublattice interactions are comparable with intersublattice interaction. Neel's theory predicts paramagnetism for such substances at all temperatures. This is unreasonable since strong *AA* or *BB* interaction may lead to some kind of ordering especially at low temperature. In the cases of no *AB* interaction, antiferromagnetic ordering may be expected either in the *A* or in the *B* sublattice. Under certain conditions there may be non-collinear spin arrays of still lower energy.

2.6.3 Effect of zinc substitution on the magnetic moments in spinel ferrites

Fe_3O_4 has ferromagnetic properties because of its inverse structure which leads to the formation of domains. A unit cell of Fe_3O_4 contains eight formula units each of which may be written in the form $Fe^{3+}[Fe^{2+}Fe^{3+}]O_4^{2-}$ [21]. Snock and his co-workers found that oxides of inverse structure could be artificially produced in which the divalent ions of another element, for example *Mn*, *Ni*, *Co*, *Mg* or *Cu*, could be substituted for the divalent Fe^{2+} ions in Fe_3O_4. An extensive range of ferrites could thus be made having the general formula $\vec{Fe}^{3+}[\overleftarrow{M}^{2+}\overleftarrow{Fe}^{3+}]O_4^{2-}$, where arrows indicate spin ordering. Since the trivalent iron ions are equally distributed on *A* and *B* sites they cancel each other out magnetically, and the magnetic moment per formula unit is then theoretically the same as the magnetic moment of the divalent ion. The *Ni* ferrite has a moment of $2.3\mu_B$ compared with a theoretical value of $2\mu_B$ [1]. *Zn* ferrite is a normal spinel, with $Zn^{2+}(3d^{10})$ ions in *A* sites have zero magnetic moment; Fe^{3+} ions in *B* sites have a magnetic moment $5\mu_B$. The cation distribution can be written as $Zn^{2+}[\vec{Fe}^{3+}\overleftarrow{Fe}^{3+}]O_4$, where spin ordering is indicated by arrows. The zero magnetic moment of Zn^{2+} ions leaves trivalent iron ions on *B* sites with a negative *BB* interaction between equal ions. Therefore *Zn* ferrite is not ferromagnetic. Zinc ferrite therefore be expected to be antiferromagnetic and thus to have a Néel point, though measurements show it to be paramagnetic only [1-2, 19, 21].

Magnetic properties can be modified widely by cation substitution. An illustrative case is substitution of *Ni* by *Zn* in *Co* ferrite to form solid solutions $Ni_{1-x}Zn_xFe_2O_4$. The cation distribution can be written as $(Zn_x^{2+}Fe_{1-x}^{3+})[Ni_{1-x}^{2+}Fe_{1+x}^{3+}]O_4^{2-}$ [2]. Zn^{2+} is diamagnetic and its main effect is to break linkages between magnetic cations. Another effect is to increase interaction distance by expanding the unit cell, since it has an ionic radious larger than the *Ni* and *Fe* radii. The most remarkable effect is that substitution of this diamagnetic cation (*Zn*) results in a significant increase in magnetic moment in a number of spinel solid solutions, Fig. 2.11.

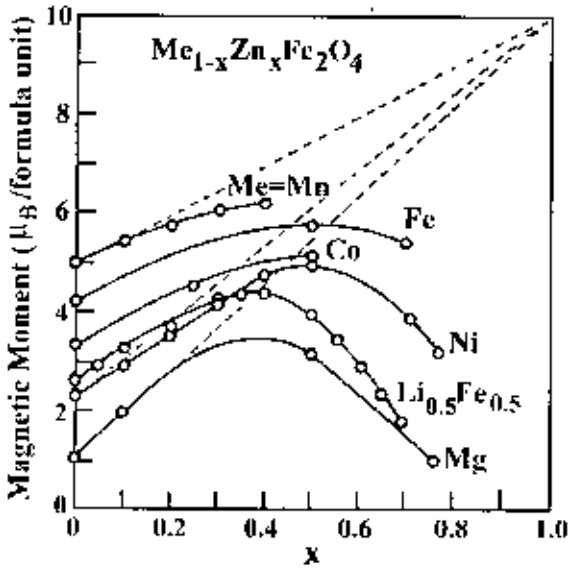

Figure 2.11. Variation of Magnetic moment (in Bohr magnetons per formula unit) with increasing zinc substitution [1, 2].

Magnetic moment as a function of *Zn* content shows an increase for small substitutions, goes through a maximum for intermediate values, decreases and finally vanishes for high *Zn* contents

A simple analysis shows that this increase can be expected for an antiparallel alignment. As the *Zn* content increases, magnetic moments decreases in sublattice *A* and increase in sublattice *B*. If the magnetic moment of *Fe* and *Ni* are 5 and ~2.3 μ_B/ion, respectively, then, per foufumula unit, the total moment in Bohr magnetons on *B* sublattice is $2.3(1-x)+5(1+x)$ and on *A* sublattice the total antiparallel moment

is $5(1-x)$. If the resultant moment per formula unit is $M_s(0)$, then by taking the difference of *A* and *B* moments [21],

$$M_s(0) = 2.3(1-x) + 5(1+x) - 5(1-x)$$
$$= x(10-2.3) + 2.3$$

A linear relationship is obtained with a slope of 7.7, predicting a moment value of $10\mu_B$ per formula unit for *Zn* substitution $x = 1$, as shown by the broken lines in Fig. 2.11. This relationship is not followed over the entire composition range. However, as the *Zn* content increases, $A-O-B$ interactions become too weak and $B-O-B$ interactions begin to dominate. That is, the average distance between the interacting spins gets larger. As a consequence, the system becomes frustrated causing a perturbation to the magnetically ordered spins as large number of *B* sites spins gets non-magnetic impurity atoms as their nearest neighbors.

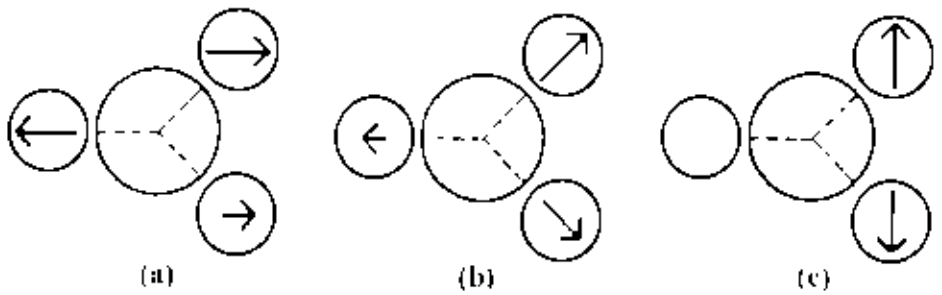

Figure 2.12. Schematic representation of spin arrangements in $Ni_{1-x}Zn_xFe_2O_4$ (a) ferrimagnetic (for $x \leq 0.5$), (b) triangular or Yafet-Kittel (for $x > 0.5$), and (c) antiferromagnetic for $x \approx 1$.

The *B* spins are no longer held in place due to this weak anti-ferromagnetic *A*-*B* interaction leading to non-collinearity or canting among the *B* sublattice. Thus for $x > 0.5$ *Zn* content, instead of a collinear antiparallel alignment, canted structure appears, where spins in *B* sites are no longer parallel [2, 25], Fig. 2.12. Evidence of this triangular structure has been observed by neutron diffraction [26]; a theoretical analysis showed that departure from collinear order depends on the ratio of the $A-O-B$ to $B-O-B$ molecular field coefficients, $\lambda_{AB}/\lambda_{BB}$ [27]. For high *Zn* concentration, $B-O-B$ interactions dominant and the ferrite become antiferromagnetic for $x = 1$ [2].

2.7 Microstructure

A polycrystal is much more than many tiny crystals bonded together. The interfaces between the crystals, or the grain boundaries which separate and bond the grains, are complex and interactive interfaces. The whole set of a given material's properties (mechanical, chemical and especially electrical and magnetic) depend strongly on the nature of the microstructure.

In the simplest case, the grain boundary is the region, which accommodates the difference in crystallographic orientation between the neighbouring grains. For certain simple arrangements, the grain boundary is made of an array of dislocations whose number and spacing depends on the angular deviation between the grains. The ionic nature of ferrites leads to dislocation patterns considerably more complex than in metals, since electrostatic energy accounts for a significant fraction of the total boundary energy [2].

For low-loss ferrite, Ghate [1] states that the grain boundaries influence properties by

1) creating a high ressistivity intergranular layer,
2) acting as a sink for impurities which may act as a sintering aid and grain growth modifiers,
3) providing a path for oxygen diffusion, which may modify the oxidation state of cations near the boundaries.

In addition to grain boundaries, ceramic imperfections can impede domain wall motion and thus reduce the magnetic property. Among these are pores, cracks, inclusions, second phases, as well as residual strains. Imperfections also act as energy wells that pin the domain walls and require higher activation energy to detach. Stresses are microstructural imperfections that can result from impurities or processing problems such as too rapid a cool. They affect the domain dynamics and are responsible for a much greater share of the degradation of properties than would expect [1].

Grain growth kinetics depends strongly on the impurity content. A minor dopant can drastically change the nature and concentration of defects in the matrix, affecting grain boundary motion, pore mobility and pore removal [2, 28]. The effect of a given dopant depends on its valence and solubility with respect to host material. If it is not

soluble at the sintering temperature, the dopant becomes a second phase which usually segregates to the grain boundary.

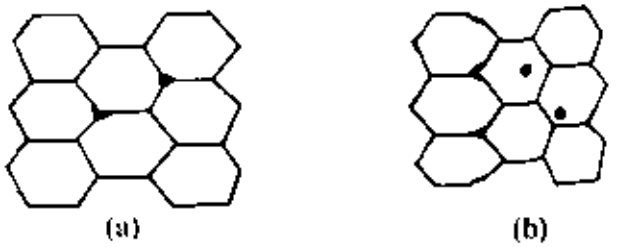

Figure 2.13. Porosity character: (a) intergranular, (b) intragranular

The porosity of ceramic samples results from two sources, intragranular porosity and intergranular porosity, Fig. 2.13. An undesirable effect in ceramic samples is the formation of exaggerated or discontinuous grain growth which is characterized by the excessive growth of some grains at the expense of small, neighbouring ones, Fig. 2.14. When this occurs, the large grain has a high defect concentration. Discontinuous growth is believed to result from one or several of the following: powder mixtures with impurities; a very large distribution of initial particle size; sintering at excessively high temperatures, in ferrites containing *Zn* and /or *Mn*, a low O_2 partial pressure in the sintering atmosphere. When a very large grain is surrounded by smaller ones, it is called "duplex" microstructure.

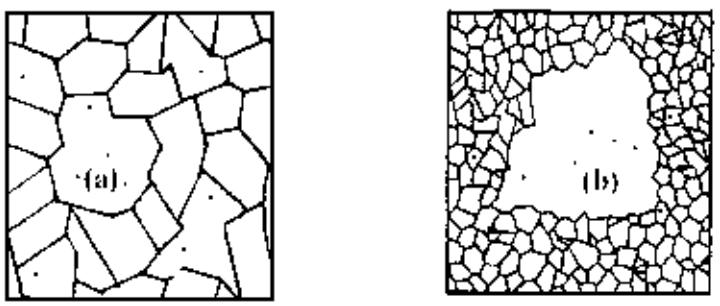

Figure 2.14. Grain growth (a) discontinuous, (b) duplex (schematic).

2.8 Theories of permeability

Permeability is defined as the proportionality constant between the magnetic field induction B and applied field intensity H [2, 23, 29]:

$$B = \mu H \tag{2.7}$$

If the applied field is very low, approaching zero, the ratio will be called the initial permeability, Fig. 2.15 and is given by

$$\mu_i = \frac{\Delta B}{\Delta H}_{(\Delta H \to 0)}$$

This simple definition needs further sophistications. A magnetic material subjected to an ac magnetic field can be written as

$$H = H_0 e^{i\omega t} \tag{2.8}$$

It is observed that the magnetic flux density B lag behind H. This is caused due to the presence of various losses and is thus expressed as

$$B = B_0 e^{i(\omega t - \delta)} \tag{2.9}$$

Here δ is the phase angle that marks the delay of B with respect to H. The permeability is then given by

$$\mu = \frac{B}{H} = \frac{B_0 e^{i(\omega t - \delta)}}{H_0 e^{i\omega t}} = \frac{B_0 e^{-i\delta}}{H_0} = \frac{B_0}{H_0}\cos\delta - i\frac{B_0}{H_0}\sin\delta = \mu' - i\mu'' \tag{2.10}$$

where $$\mu' = \frac{B_0}{H_0}\cos\delta \tag{2.11}$$

and $$\mu'' = \frac{B_0}{H_0}\sin\delta \tag{2.12}$$

The real part (μ') of complex permeability (μ), as expressed in equation (2.10) represents the component of B which is in phase with H, so it corresponds to the normal permeability. If there are no losses, we should have $\mu = \mu'$. The imaginary part μ'' corresponds to that of B, which is delayed by phase angle 90^0 from H [19, 23]. The presence of such a component requires a supply of energy to maintain the alternating magnetization, regardless of the origin of delay. The ratio of μ'' to μ', as is evident from equation (2.12) and (2.11) gives

$$\frac{\mu''}{\mu'} = \frac{\frac{B_0}{H_0}\sin\delta}{\frac{B_0}{H_0}\cos\delta} = \tan\delta \tag{2.13}$$

This $\tan\delta$ is called loss factor.

The quality factor is defined as the reciprocal of this loss factor, i.e.

$$\text{Quality factor} = \frac{1}{\tan\delta} \tag{2.14}$$

And the relative quality factor, $Q = \frac{\mu'}{\tan\delta}$ (2.15)

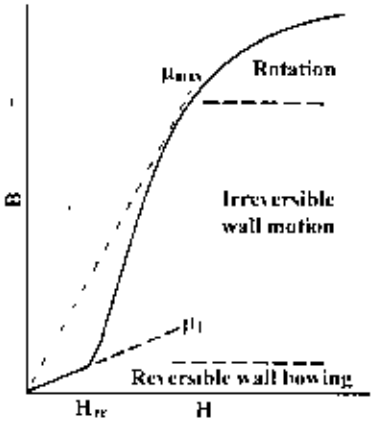

Figure 2.15. Schematic magnetization curve showing the important parameter: initial permeability, μ_i (the slope of the curve at low fields) and the main magnetization mechanism in each magnetization range.

The curves that show the variation of both μ' and μ'' with frequency are called the magnetic spectrum or permeability spectrum of the material [19]. The variation of permeability with frequency is referred to as dispersion. The measurement of complex permeability gives us valuable information about the nature of domain wall and their movements. In dynamic measurements the eddy current loss is very important. This occurs due to the irreversible domain wall movements. The permeability of a ferrimagnetic substance is the combined effect of the wall permeability and rotational permeability mechanisms.

2.8.1 Mechanisms of permeability

The mechanisms can be explained as follows: A demagnetized magnetic material is divided into number of Weiss domains separated by Bloch walls. In each domain all the magnetic moments are oriented in parallel and the magnetization has its saturation value M_s. In the walls the magnetization direction changes gradually from the direction of magnetization in one domain to that in the next. The equilibrium positions of the walls result from the interactions with the magnetization in neighboring domains and from the influence of pores; crystal boundaries and chemical inhomogeneities which tend to favour certain wall positions.

2.8.1.1 Wall permeability

The mechanism of wall permeability arises from the displacement of the domain walls in small fields. Lets us consider a piece of material in the demagnetized state, divided into Weiss domains with equal thickness L by means of 180° Bloch walls (as in the Fig. 2.16). The walls are parallel to the YZ plane. The magnetization M_s in the domains is oriented alternately in the $+Z$ or $-Z$ direction. When a field H with a component in the $+Z$ direction is applied, the magnetization in this direction will be favoured. A displacement dx of the walls in the direction shown by the dotted lines will decrease the energy density by an amount [30, 31]:

$$\frac{2M_s H_z dx}{L}$$

This can be described as a pressure $M_s H_z$ exerted on each wall. The pressure will be counteracted by restoring forces which for small deviations may assume to be kdx per unit wall surface. The new equilibrium position is then given by

$$d = \frac{M_s H_z dx}{L}$$

From the change in the magnetization

$$\Delta M = \frac{2M_s d}{L},$$

the wall susceptibility χ_w may be calculated Let H makes the angle θ with Z direction. The magnetization in the θ direction becomes

$$(\Delta M)_\theta = \frac{2M_s d}{L}\cos\theta \text{, And with } H_z = H\cos\theta \text{ and } d = \frac{2M_s H_z}{K}$$

we obtain

$$\chi_w = \frac{(\Delta M)_\theta}{H} = \frac{4M_s^2\cos^2\theta}{KL} \tag{2.16}$$

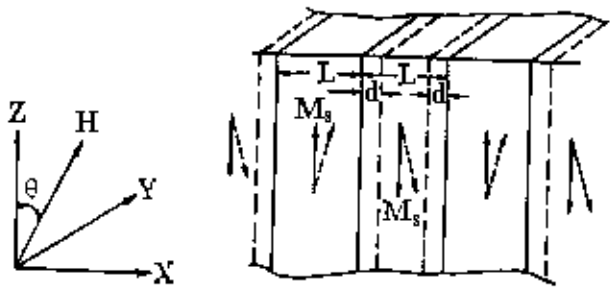

Figure 2.16. Magnetization by wall motion and spin rotation.

2.8.1.2 Rotational permeability

The rotational permeability mechanism arises from rotation of the magnetization in each domain. The direction of M can be found by minimizing the magnetic energy E as a function of the orientation Major contribution to E comes from the crystal anisotropy energy. Other contributions may be due to the stress and shape anisotropy. The stress may influence the magnetic energy via the magnetostriction. The shape anisotropy is caused by the boundaries of the sample as well as by pores, nonmagnetic inclusions and inhomogeneities. For small angular deviations, α_x and α_y may be written as

$$\alpha_x = \frac{M_x}{M_s} \text{ and } \alpha_y = \frac{M_y}{M_s}.$$

For equilibrium Z-direction, E may be expressed as [24, 25]

$$E = E_0 + \frac{1}{2}\alpha_x^2 E_{xx} + \frac{1}{2}\alpha_y^2 E_{yy}$$

where it is assumed that x and y are the principal axes of the energy minimum. Instead of E_{xx} & E_{yy}, the anisotropy field H_x^A and H_y^A are often introduced. Their magnitude is given by

$$H_x^A = \frac{E_{xx}}{2M_s} \text{ and } H_y^A = \frac{E_{yy}}{2M_s},$$

H_x^A & H_y^A represent the stiffness with which the magnetization is bound to the equilibrium direction for deviations in the x and y direction, respectively. The rotational susceptibilities $\chi_{r,x}$ and $\chi_{r,y}$ for fields applied along x and y directions, respectively are

$$\chi_{r,x} = \frac{M_s}{H_x^A} \text{ and } \chi_{r,y} = \frac{M_s}{H_y^A}.$$

For cubic materials it is often found that H_x^A and H_y^A are equal. For $H_x^A = H_y^A = H^A$ and a field H which makes an angle θ with the Z direction (as shown in Fig. 2.16) the rotational susceptibility, $\chi_{r,c}$ in one crystallite becomes

$$\chi_{r,c} = \frac{M_s}{H^A}\sin^2\theta \qquad (2.17)$$

A polycrystalline material consisting of a large number of randomly oriented grains of different shapes, with each grain divided into domains in a certain way. The rotational susceptibility χ_r of the material has to be obtained as a weighted average of $\chi_{r,c}$ of each crystallite, where the mutual influence of neighbouring crystallites has to be taken into account. If the crystal anisotropy dominates other anisotropies, then H^A will be constant throughout the material, so only the factor $\sin^2\theta$ (equation 2.17) has to be averaged. Snoek [32] assuming a linear averaging of $\chi_{r,c}$ and found

$$\chi_r = \frac{2M_s}{3H^A}$$

The total internal susceptibility

$$\chi = \chi_w + \chi_r = \frac{4M_s^2 \cos^2\theta}{KL} + \frac{2M_s}{3H^A} \qquad (2.18)$$

If the shape and stress anisotropies cannot be neglected, H^A will be larger. Any estimate of χ_r will then be rather uncertain as long as the domain structure, and the pore distribution in the material are not known. A similar estimate of χ_w would require knowledge of the stiffness parameter k and the domain width L. These parameters are influenced by such factors as imperfection, porosity and crystallite shape and distribution which are essentially unknown

References

[1] A. Goldman, *Handbook of Modern Ferromagnetic Materials*, Kulwer Acad. Pub, Boston, U.S.A (1999)

[2] R. Valenzuela, *Magnetic Ceramics*, Cambridge University Press, Cambridge (1994)

[3] M. M. Haque, "Influence of additives on the magnetic and electrical properties of iron-excess Mn-Zn ferrites," *M. Phil. Thesis*, BUET, Bangladesh (2000).

[4] J. Tasaki and T. Ito, *Intl. Conf. On Ferrite*, Japan, (1970).

[5] T. Nakamura, "Low-temperature sintering of Ni-Zn-Cu ferrite and its permeability spectra," *J. Magn. Magn. Mater.* **168**, 285 (1997).

[6] E. Roess, *Ferrites*, U. of Tokyo Press, Tokyo, 187 (1971).

[7] L. K. Leung, B. J. Evans and A. H. Morrish, "Low-temperature Mössbauer study of a nickel-zinc ferrite $Zn_{1-x}Ni_xFe_2O_4$," *Phys. Rev. B*, **8**, 29 (1973)

[8] N. Rezlescu, E. Rezlescu, C. Pasnicu and M. L. Craus, "Effects of the rare-earth ions on some properties of a Nickel-Zinc ferrite," *J. Phys.: Condens. Matter.*, **6**, 5707 (1994)

[9] E. Rezlescu, L. Sachelaric, P. D. Popa and N. Rezlescu, "Effect of substitution of diavalent ions on the electrical and magnetic properties of Ni-Zn-Me ferrites," *IEEE Trans. Magn.*, **36**, 3962 (2000)

[10] Caltun Ovidiu F., Leonard Spinu, "Magnetic properties of high frequency NiZn ferrites doped with CuO," *IEEE Trans. Magn.*, **37(4)**, 1 (2001).

[11] Chul Sung Kim, Woo Chul Kim, Sung Yong An, Seung Wha Lee, "Structure and mossbauer studies of Cu-dopped NiZn ferrites," *J. Magn. Magn. Mater.*, **213**, 215-216 (2000)

[12] I.Z. Rahman and T. T. Ahmed, "A study on Cu substituted chemically processed Ni-Zn-Cu ferrites", *J. Magn. Magn. Mater.*, 290-291, 1576-1579 (2005)

[13] Woo Chul Kim, Sa Jin Kim,, Seung Wha Lee, Chul Sung Kim, "Growth of ultrafine NiCuZn ferrite and magnetic properties," *J. Magn. Magn. Mater.*, **226 230(2)**,1418 (2001)

[14] T. Nakamura "Low temperature sintering of Ni-Zn-Cu ferrite and its permeability spectra," *J. Magn. Magn. Mater.*, **168**, 285 (1997).

[15] Caltun O F , Spinu L , Stancu Al., Thung L.D ,Zhou W., "Study of the microstructure and of the permeability spectra of Ni-Zn-Cu ferrites," *J Magn. Magn. Mater.*, **160**, 242-245 (2002).

[16] Aminul Islam "Effect of microstructure n the magnetic and electric properties of nickel-zink ferrites doped with copper oxide," *M. Phil. Thesis*, BUET, Bangladesh (2002).

[17] A Globus, *2nd EFS Conf on Soft Magnetic Materials*, Wolfson Center for Magnetic Technology, Cardiff, Wales (1975)

[18] M. A. Ahmed and M A El Hiti, "Electrical and dielectric properties of $Zn_{0.85}Co_{0.20}Fe_2O_4$," *J. Phys III France5, 775(1995).*

[19] B D Cullity, *Introduction to Magnetic Materials*, Addison-Wisley Publishing Company, Inc , California (1972).

[20] M A. Wahab, *Solid State Physics: Structure and Properties of Materials*, Narosa Publishing House, New Delhi (1999)

[21] F. Brailsford, *Physical Principles of Magnetism*, D. Van Nostrand Company Ltd., London (1966).

[22] A J. Dekker, *Solid State Physics*, Macmillan India Ltd , New Delhi (1998)

[23] S. Chikazumi, *Physics of Magnetism*, Jhon Wiley & Sons, Inc., New York (1966)

[24] C Kittel, *Introduction to Solid State Physics*, 7th edition, Jhon Wiley & Sons, Inc., Singapore (1996).

[25] A. K M Akther Hossain, M. Seki, T. Kawai and H. Tabata, "Colossal magnetoresistance in spinel type $Zn_{1-x}Ni_xFe_2O_4$," *J Appl Phys.*, **96**, 1273 (2004)

[26] N. S Satya Murthy, M G Natera and S I Youssef "Yafet-Kittel angles in nickel-zinc ferrites," *Physical Review*, **181**, 969 (1969).

[27] Y. Yafet and C. Kittel "Antiferromagnetic arrangements in ferrites," *Physical Review*, **87**, 290 (1952)

[28] M F Yan and D W Johnson, "Impurity induced exaggerated grain growth in Mn-Zn ferrites," *J. Am. Ceram. Soc.*, **61**, 342 (1978).

[29] D. Hadfield, *Permanent Magnets and Magnetism*, Jhon Wiley & Sons, Inc., New York (1962).

[30] S. S. Sikder, "Temperature dependence of magnetization and induced magnetic anisotropy of some Fe, Co and Ni-based amorphous ribbons " *Ph. D. Thesis*, BUET, Bangladesh (1999).

[31] K. M A. Hussain, "Study of complex permeability and secondary effects in some cobalt and manganese based ferrites," *M Phil Thesis*, BUET, Bangladesh (2003).

[32] J L Snoek, "Dispersion and absorptions in magnetic ferrites at frequencies above Mc/s," *Physica*, **14**, 207 (1948).

CHAPTER 3

SAMPLE PREPARATION

In this chapter we describe the preparation method of samples. We describe also the effect of calcinations and sintering process on the ferrites

3.1 Composition of the studied ferrite system

In the present research Cu^{2+}-based soft ferrites are synthesized and investigated The ferrites under investigation are:

$Ni_{0.50-x}Cu_xZn_{0.50}Fe_2O_4$ (with x = 0.00, 0.05, 0.10, 0.15, 0.20, 0.25, 0.30)

$Ni_{0.45-x}Cu_{(x+y)}Zn_{0.55-y}Fe_2O_4$ (with x = 0.00, 0.05, 0.10 and y = 0.00, 0.10, 0.10)

3.2 Sample preparation

A goal common to all the ferrites is the formation of the spinel structure. Now a days, the majority of ferrite powders are made by the conventional Ceramic process or Solid State Reaction technique. Most of the non-conventional processes are involved in producing the powder by a wet method. Among these methods, some are [1, 2]:

1) Co-precipitation
2) Organic precursors
3) Sol-gel synthesis
4) Spray-drying
5) Freeze-drying
6) Combustion synthesis
7) Glass crystallization

In this chapter, we describe the combustion method that is used in this research work.

3.3 Combustion Method

Combustion method a novel method for preparation of fine particles of ferrites makes use of the strong exothermic reaction between metal nitrate and fuel. In this processes, the stoichiometric ratio of nitrates is dissolve in the minimum amount of ethanol in a glass beaker and starrier it until all the nitrate salts completely soluble in the

ethanol. The mixed solution was then evaporated on a constant temperature water bath. After boiling and ignition of the mixture, a spinel residue is obtain in a few minutes. A heating rate of at least 75°C/min is used to obtained good combustion. These powders are crushed and ground thoroughly. Low temperature calcination has to perform. The calcined powders are again crushed into fine powders. The pellets or toroid-shaped samples are prepared from these calcined powders using die-punch assembly or hydrostatic or isostatic pressure. Sintering is carried out, at temperature ranging 1100-1400°C, for times of typically 1-40 h and in various atmospheres (e.g. Air, O_2 and N_2) [3-6]. Fig. 3.1 shows, diagrammatically, the stages followed in preparation of nanocrystalline ferrite by combustion method.

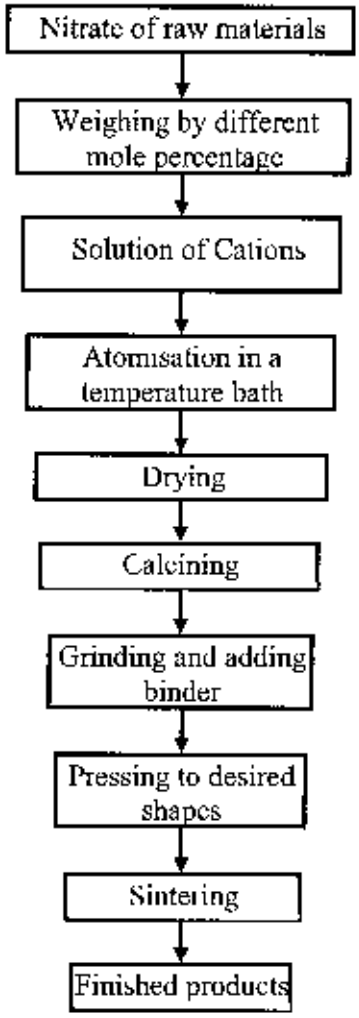

Figure 3.1. Flow chart of the stages in preparation of spinel ferrite

There are basically four steps in the preparation of ferrite:

1) Preparation of materials to form an intimate mixture with the metal nitrate in the ratio which they will have in the final product,
2) Heating of this mixture to form the ferrite (often called calcining),
3) Grinding the calcined powders and pressing the fine powders into the required shape, and
4) Sintering to produce a highly densified product.

The calcining process can be repeated several times to obtain a high degree of homogeneity. This calcined powders are fine powders. The ideal characteristics of fine powders are [2]:

1) small particle size (sub micron)
2) narrow distribution in particle size
3) dispersed particles
4) equiaxed shape of particles
5) high purity
6) homogeneous composition.

A small particle size of the reactant powders provides a high contact surface area for initiation of the solid state reaction, diffusion paths are shorted, leading to more efficient completion of the reaction. Porosity is easily eliminated if the initial pores are very small. A narrow size distribution of spherical particles as well as a dispersed state is important for compaction of the powder during green-body formation. Grain growth during sintering can be better controlled if the initial size is small and uniform.

A binder is usually added prior to compaction, at a concentration lower than 5wt % [2]. Binders are polymers or waxes; the most commonly used binder in ferrite is polyvinyl alcohol. The binder facilitates the particles flow during compacting and increases the bonding between the particles, presumably by forming bonds of the type *particle-binder-particle*. During sintering, binders decompose and are eliminated from the ferrite. Pressures are used for compacting very widely but are commonly several tons per square inch (i. e., up to 10^8 N m^{-2}).

Sintering is defined as the process of obtaining a dense, tough body by heating a compacted powder for a certain time at a temperature high enough to significantly promote diffusion, but clearly lower than the melting point of the main component. The

driving force for sintering is the reduction in surface free energy of the powder. Part of this energy is transferred into interfacial energy (grain boundaries) in the resulting polycrystalline body [2, 7]. The sintering time, temperature and the furnace atmosphere play very important role on the magnetic property of ferrite materials. The purposes of sintering process are.

1) to bind the particles together so as to impart sufficient strength to the product,
2) to densify the material by eliminating the pores and
3) to homogenize the materials by completing the reactions left unfinished in the calcining step

Sintering of crystalline solids is dealt by Coble and Burke [8] who found the following empirical relationship regarding rate of grain growth:

$$\bar{d} = kt^n$$

where $\bar{d}$ is the mean grain diameter, n is about 1/3, t is sintering time and k is a temperature dependent parameter. Sintering is divided into three stages. Fig. 3.2 [2, 9].

Stage 1. Contact area between particles increases,

Stage 2. Porosity changes from open to closed porosity,

Stage 3. Pore volume decreases; grains grow.

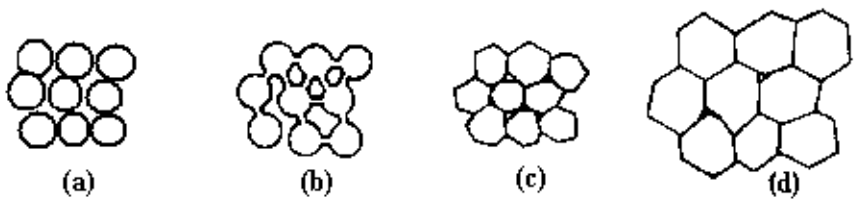

Figure 3.2. Schematic representation of sintering stages (a) greenbody, (b) initial stage, (c) intermediate stage, and (d) final stage.

In the initial stage, neighbouring particles form a neck by surface diffusion and presumably also at high temperatures by an evaporation-condensation mechanism. Grain growth begins during the intermediate stage of sintering. Since grain boundaries are the sinks for vacancies, grain growth tends to decrease the pore elimination rate due to the increase in distance between pores and grain boundaries, and by decreasing the total grain boundary surface area. In the final stage, the grain growth is considerably enhanced and the remaining pores may become isolated.

In *Ni-Zn* ferrites, the presence of *Zn* complicates the sintering process because high temperature coupled with low oxygen firing will cause *Zn* loss. High density is important for high permeability, but so is *Zn* conservation. Tasaki [1] described two alternative firings to achieve high density:

1) Low sintering temperature excluding O_2 (Vacuum, argon, nitrogen),
2) High temperature in pure oxygen to reduce *Zn* loss.

Accordingly, other properties correlated along with density:

1) Lattice constant is greater for O_2, smaller for vacuum
2) Curie temperature is greater for vacuum, smaller for O_2
3) Resistivity is greater for O_2, smaller for vacuum.

3.4 Preparation of the present samples

Nanolycrystalline $Ni_{0.50-x}Cu_xZn_{0.50}Fe_2O_4$ (x=0, 0.05, 0.10, 0.15, 0.20, 0.25 and 0.30) and $Ni_{0.45-x}Cu_{(x+y)}Zn_{0.55-y}Fe_2O_4$ (with x = 0.00, 0.05, 0.10 and y = 0.00, 0.10, 0.10) ferrites were prepared by combustion technique. For the preparation of Ni-Cu-Zn ferrites, the analytical pure grade of $Ni(NO_3)_2.6H_2O$, $Cu(NO_3)_2.3H_2O$, $Zn(NO_3)_2.6H_2O$ and $Fe(NO_3)_3.9H_2O$ are weighted according to the desired composition and dissolved in an appropriate amount of ethanol. The mixture will be placed in a constant temperature bath at 70-80°C, followed by an ignition, the combustion reaction is completed within a few seconds and fine nanosized powders will be precipitated. These powders are crushed and ground thoroughly. The fine powders of various compositions are then calcined at 900°C for 5 h for the final formation of Ni-Cu-Zn ferrite nano-particles. Then the fine powders are granulated using Poly Vinyl Alcohol (PVA) as a binder and pressed into disk- and toroid-shaped samples. The samples are sintered at various temperatures in air for 5 hours. The temperature ramps for sintering are 5°C/min for heating, and 10°C/min for cooling.

Figure 3.3 a) Disk and b) Toroid shaped Samples.

References

[1] A Goldman, *Handbook of Modern Ferromagnetic Materials*, Kulwer Acad. Pub, Boston, U.S.A (1999)

[2] R Valenzuela, *Magnetic Ceramics*, Cambridge University Press, Cambridge (1994).

[3] A K M Akther Hossain, "Investigation of colossal magnetoresistance in bulk and thick film magnetites," *Ph D Thesis*, Imperial College, London (1998).

[4] B. D Cullity, *Introduction to Magnetic Materials*, Addison-Wisley Publishing Company, Inc., California (1972)

[5] R. J. Brook, *Sintering: An Overview, Concise Encyclopedia of Advanced Ceramic Materials*, Pergamon Press, Oxford, pp. 438 (1991).

[6] P Reijnen, *Science of Ceramics*, Academic Press, London (1967).

[7] W. D. Kingery, H. K. Bowen and D R Uhlman, *Introduction to Ceramics*, 2nd edition, Wiley Interscience, Newyork, pp 476 (1976)

[8] R. L. Coble and J. E Burke, *4th Int Symp. On the Reactivity of Solids*, Amsterdam, pp. 38-51 (1960)

[9] I. J McColm and N. J. Clark, *Forming, Shaping and Working of high Performance Ceramics*, Blackie, Glasgow, pp. 1-338 (1988)

CHAPTER 4

EXPERIMENTAL TECHNIQUES

In this chapter we describe basic experimental techniques to measure the lattice parameters and frequency dependent AC permeability of ferrite samples. We describe also the experimental technique for the measurement of temperature dependent initial permeability. The Néel temperatures of the samples were determined from this temperature dependent initial permeability.

4.1 X-ray diffraction

Bragg reflection is a coherent elastic scattering in which the energy of the X-ray is not changed on reflection. If a beam of monochromatic radiation of wavelength λ is incident on a periodic crystal plane at an angle θ and is diffracted at the same angle as shown in Fig. 4.1, the Bragg diffraction condition for x-rays is given by

$$2d\,Sin\theta = n\lambda \qquad (4.1)$$

where d is the distance between crystal planes and n is the positive integer which represents the order of reflection. Equation (4.1) is known as Bragg law. This Bragg law suggests that the diffraction is only possible when $\lambda \leq 2d$ [1]. For this reason we cannot use the visible light to determine the crystal structure of a material. The X-ray diffraction (XRD) provides substantial information on the crystal structure.

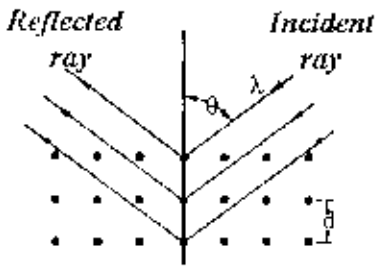

Figure 4.1. Bragg law of diffraction

X-ray diffraction was carried out with an X-ray diffiactometer for the samples $Ni_{0.50-x}Cu_xZn_{0.50}Fe_2O_4$ (with x = 0.00, 0.05, 0.10, 0.15, 0.20, 0.25) and

$Ni_{0.45-x}Cu_{(x+y)}Zn_{0.55-y}Fe_2O_4$ (with x = 0.00, 0.05, 0.10 and y = 0.00, 0.10, 0.10). For this purpose monochromatic Cu-K_α radiation was used. The lattice parameter for each peak of each sample was calculated by using the formula

$$a = d\sqrt{h^2 + k^2 + l^2} \tag{4.2}$$

where h, k and l are the indices of the crystal planes. To determine the exact lattice parameter for each sample, Nelson-Riley method was used. The Nelson-Riley function $F(\theta)$ is given as

$$F(\theta) = \frac{1}{2}\left[\left(Cos^2\theta / Sin\theta\right) + \left(Cos^2\theta / \theta\right)\right] \tag{4.3}$$

The values of lattice constant 'a' of all the peaks for a sample are plotted against $F(\theta)$. Then using a least square fit method exact lattice parameter 'a_0' is determined. The point where the least square fit straight line cut the y-axis (i.e at $F(0) = 0$) is the actual lattice parameter of the sample.

The physical or bulk densities ρ_B of the samples were determined by Archimedes principle with water medium using the following expression[2]:

$$\rho_B = \frac{W\rho}{W - W'}\, g/cm^3 \tag{4.4}$$

where W is the weight of the sample in air, W' is the weight of the sample in the water and ρ is the density of water in room temperature

The theoretical density ρ_{th} was calculated using following expression:

$$\rho_{th} = \frac{8M}{N_A a_o^3}\, g/cm^3 \tag{4.5}$$

where N_A is Avogadro's number (6.02×10^{23} mol^{-1}), M is the molecular weight. The porosity was calculated from the relation $\{100(\rho_{th} - \rho_B)/\rho_{th}\}\%$, where ρ_B is the bulk density measured by Archimedes principle

4.2 Study of microstructure

The microstructural study was performed in order to have an insight of the grain structures. The samples of different compositions and sintered at different temperatures were chosen for this purpose. The samples were visualized under a high-resolution optical microscope (Olympus DP 70) and then photographed. Average

grain sizes (grain diameter) of the samples were determined from optical micrographs by linear intercept technique [3] To do this, several random horizontal and vertical lines were drawn on the micrographs. Therefore, we counted the number of grains intersected and measured the length of the grains along the line traversed. Finally the average grain size was calculated.

4.3 Average particle size measurement

Particle size determination is important in the ferrite nanoparticles Due to their small particle size significant fine particle broadening is observed in the Bragg peaks. A crystal is usually considered perfect when atoms occupy all lattice sites and no imperfection exists in the crystal. The broadening of diffraction peaks arises mainly due to three factors. The peaks become broader due to the effect of small crystallite sizes and thus an analysis of peaks broadening can be use to determine the crystallite sizes introduce additional broadening into the diffraction peaks.

The condition for constructive interference, reinforcement of X-ray scattering from a crystalline powder is given by Bragg's law which is given by Eq. 4.1:

$$2d\,Sin\theta = n\lambda$$

This equates the path difference of X-ray scattered from parallel crystalline planes spaced d $= d_{hkl}$ apart to an integral (n) number of X-ray wavelength λ Here θ is the diffraction angle measured with respect to the crystalline planes For an infinite crystal Bragg scattering occurs at discrete values of 2θ satisfying the Bragg condition, i.e. Bragg peaks are δ-function For finite sized crystals the peaks are broadened over a range of angle

To understand the phenomenon of fine particle broadening following argument of Cullity [4], we consider a finite crystal of thickness, D=md. where m is an integer and d is the distance between crystal planes, i.e. there are m planes in D.

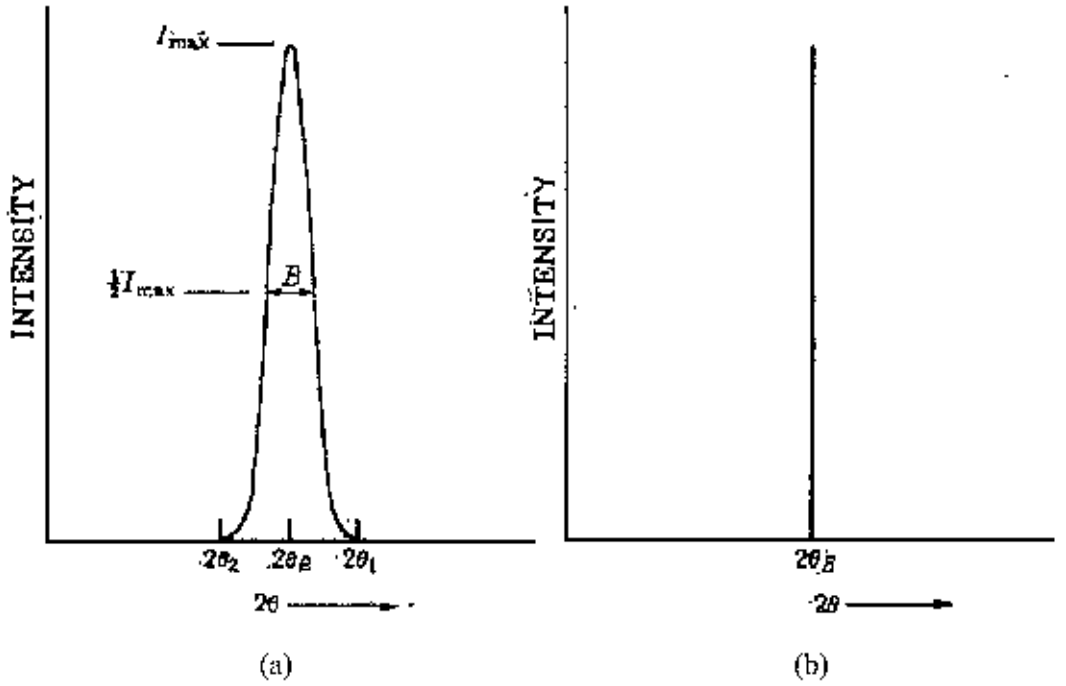

Figure 4.2. Effect of fine particle size on diffraction curves (Schematic). (a). small particle size and (b) large particle size

Considering Fig4.2, if the broadened Bragg peak begins at an angle $2\theta_1$ and ends at $2\theta_2$, the breadth of the peaks or full width at half maximum (FWHM) is given as:

$$\beta = \frac{1}{2}(2\theta_1 - 2\theta_2) = (\theta_1 - \theta_2) \tag{4 6}$$

Now if we consider the path differences for each of the two angles θ_1 and θ_2 for X-ray traveling the full thickness of the crystal. The width β is usually measured in radians. We now write path difference equations for these two angles, related to the entire thickness of the crystal rather to the distance between adjacent planes

$$2D\sin\theta_1 = (n+1)\lambda \tag{4.7}$$

$$2D\sin\theta_2 = (n-1)\lambda \tag{4.8}$$

By subtraction we find.

$$D(\sin\theta_1 - \sin\theta_2) = \lambda \tag{4.9}$$

$$D2\cos\left(\frac{\theta_1+\theta_2}{2}\right)\sin\left(\frac{\theta_1-\theta_2}{2}\right)=\lambda \tag{4.10}$$

But θ_1 and θ_2 are both very nearly equal to θ. so that $\theta_1+\theta_2\approx 2\theta$ and $\sin\left(\frac{\theta_1-\theta_2}{2}\right)\approx\left(\frac{\theta_1-\theta_2}{2}\right)$. So that equation (4.10) can be written as.

$$D2\cos\left(\frac{2\theta}{2}\right)\left(\frac{\theta_1-\theta_2}{2}\right)=\lambda$$

$$\text{or, } D2\cos\theta\left(\frac{\theta_1-\theta_2}{2}\right)=\lambda \tag{4.11}$$

From equation (4.6) and equation (4.11) we get

$$D\beta\cos\theta=\lambda \tag{4.12}$$

$$\text{or, } D=\frac{\lambda}{\beta\cos\theta} \tag{4.13}$$

A more exact empirical treatment yields

$$D=\frac{0.9\lambda}{\beta\cos\theta}; \tag{4.14}$$

This is known as the Scherrer's formula. It is used to estimate the particle size of very small crystal from the measured width of their diffraction curves.

4.4 Complex permeability measurement

For high frequency application, the desirable property of a ferrite is high permeability with low loss. One of the most important goals of ferrite research is to fulfill this requirement. The techniques of permeability measurement and frequency characteristics of the present samples are described briefly

4.4.1 Techniques for the permeability measurement

Measurements of permeability normally involve the measurements of the change in self-inductance of a coil in presence of the magnetic core. The behaviour of a self-inductance can now be described as follows We assume an ideal loss less air coil of inductance L_0. On insertion of a magnetic core with permeability μ, the inductance will be μL_0. The complex impedance Z of this coil [5] can be expressed as follows.

$$Z = R + jX = j\omega L_0 \mu = j\omega L_0(\mu' - j\mu'') \tag{4.15}$$

where the resistive part is $R = \omega L_0 \mu''$ (4.16)

and the reactive part is $X = \omega L_0 \mu'$ (4.17)

The RF permeability can be derived from the complex impedance of a coil, Z, given by equation (4.15) The core is taken as toroidal to avoid demagnetizing effects The quantity L_0 is derived geometrically as shown in section 4.4.2.

4.4.2 Frequency characteristics of the present samples

The frequency characteristics of the ferrite samples i.e. the initial permeability spectra were investigated using an Agilent Impedance Analyzer (model no. 4192A) and Wayne Kerr Precision Impedance Analyzer (model no. 6520A). The complex permeability measurements on toroid shaped specimens were carried out at room temperature on all the samples in the frequency range 1 kHz - 13 MHz. The real part (μ_i') and imaginary part (μ_i'') of the complex permeability were calculated using the following relations [4]: $\mu_i' = L_s/L_0$ and $\mu_i'' = \mu_i' \tan\delta$. where L_s is the self-inductance of the sample core and $L_0 = \mu_0 N^2 S/\pi\bar{d}$ is derived geometrically. Here L_0 is the inductance of the winding coil without the sample core, N is the number of turns of the coil ($N = 6$), S is the area of cross section of the toroidal sample as given below:

$$S = d \times h,$$

where $$d = \frac{d_2 - d_1}{2},$$

d_1 = Inner diameter,
d_2 = Outer diameter,
h = Height

and $\bar{d}$ is the mean diameter of the toroidal sample as given below:

$$\bar{d} = \frac{d_1 + d_2}{2}$$

The relative quality factor is determined from the ratio $\frac{\mu_i'}{\tan\delta}$.

4.5 The Néel temperature measurements

The Néel temperature measurement is one of the most important measurements for ferrimagnetic materials. Néel temperature provides substantial information on magnetic states of a substance in respect of the strength of exchange interaction. So, the determination of Néel temperature is of great importance.

Néel temperature was measured from the temperature dependent initial permeability. For this measurement, the sample was kept inside a cylindrical oven with a thermocouple placed at the middle of the sample. The thermocouple measures the temperature inside the oven and also of the sample. The sample was kept just in the middle part of the cylindrical oven in order to minimize the temperature gradient. The temperature of the oven was then raised slowly. If the heating rate is very fast then temperature of the sample may not follow the temperature inside the oven, and there can be misleading information on the temperature of sample. The thermocouple showing the temperature in that case will be erroneous. Therefore, a slow heating rate was used to eliminate this problem. Also, a slow heating ensures accuracy in the determination of Néel temperature. The oven was kept thermally insulated from the surroundings. The temperature dependent permeability was measured at a constant frequency (100 kHz) of a sinusoidal wave.

4.6 DC magnetization measurement

The magnetization (M) measurements were made on pieces of the samples (approximate dimensions $2 \times 1 \times 1$ mm^3) using the Superconducting Quantum Interface Device (SQUID) magnetometer (MPMS-5S; Quantum design Co. Ltd.)

References

[1] C Kittel, *Introduction to Solid State Physics*, 7th edition, Jhon Wiley & Sons, Inc , Singapore (1996).

[2] A.B Gadkari,T J Shinde, P.N. Vasambekar, "Structural and magnetic properties of nanocrystalline Mg-Cd ferrites prepared by oxalate co-precipitation method," *J. Mater Sci. Mater Electron*, 21(1), 96-103 (2010).

[3] A K M. Akther Hossain, "Investigation of colossal magnetoresistance in bulk and thick film magnetites," *Ph D. Thesis*, Imperial College London (1998)

[4] B D Cullity Elements of X-ray diffraction,Reading, MA,Addision-Wesley,(1972)

[5] A Goldman, *Handbook of Modern Ferromagnetic Materials* Kulwer Acad Pub, Boston U S A (1999)

CHAPTER 5

RESULTS AND DISCUSSION

The nanocrystalline $Ni_{0.50-x}Cu_xZn_{0.50}Fe_2O_4$ (with x = 0.00, 0.05, 0.10, 0.15, 0.20, 0.25) and $Ni_{0.45-x}Cu_{(x+y)}Zn_{0.55-y}Fe_2O_4$ (with x = 0.00, 0.05, 0.10 and y = 0.00, 0.10, 0.10) ferrites are studied. The pellet and ring-shaped samples prepared from $Ni_{0.50-x}Cu_xZn_{0.50}Fe_2O_4$ and $Ni_{0.45-x}Cu_{(x+y)}Zn_{0.55-y}Fe_2O_4$ powders are sintered at various temperatures for five hours in air. Structural and surface morphology are studied by X-ray diffraction and optical microscopy. The AC magnetic properties of the ferrites are characterized with high frequency (1kHz-15MHz) complex permeability, and temperature dependent permeability measurements. DC Magnetizations of all samples are also studied. The effects of varying substitution and sintering temperature on the complex permeability of these ferrites are discussed.

5.1 Investigation of polycrystalline $Ni_{0.50-x}Cu_xZn_{0.50}Fe_2O_4$

5.1.1 X-ray diffraction analysis

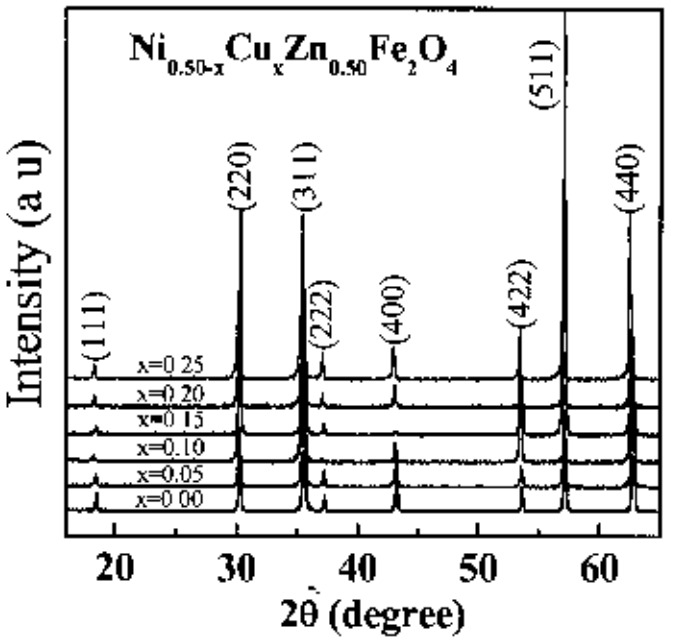

Fig.5.1. The X-ray diffraction patterns for $Ni_{0.50-x}Cu_xZn_{0.50}Fe_2O_4$

The X-ray diffraction (XRD) was performed to verify the formation of spinel structure of various $Ni_{0.50-x}Cu_xZn_{0.50}Fe_2O_4$ ferrites, in which Ni^{2+} is replaced by Cu^{2+}. The XRD patterns of these copper substituted $Ni_{0.50-x}Cu_xZn_{0.50}Fe_2O_4$ (with x = 0.00, 0.05, 0.10,

0.15, 0.20, 0.25) ferrites sintered at 1200°C in air are shown in Fig. 5.1. The results indicated that these materials have a well defined single crystalline phase and formation of spinel structure for each composition. Analyzing the XRD patterns it is observed that the positions of the peaks comply with the reported value [1] and no traces of raw materials were found, there by confirming that the chemical reaction is completed.

The lattice parameter is calculated from the XRD patterns using Nelson-Riley function [2]. The lattice constant a_0, as a function of copper content for various $Ni_{0.50-x}Cu_xZn_{0.50}Fe_2O_4$ is presented in Fig.5.2. It is noticed from this figure that the lattice constant increases with increasing of Cu^{2+} content in the $Ni_{0.50-x}Cu_xZn_{0.50}Fe_2O_4$ ferrites. The increase in lattice constant a_0, with addition of Cu^{2+} can be explained in terms of ionic radii. The radius of Cu^{2+} (0.72Å) is higher than that of Ni^{2+} (0.69Å) [3].

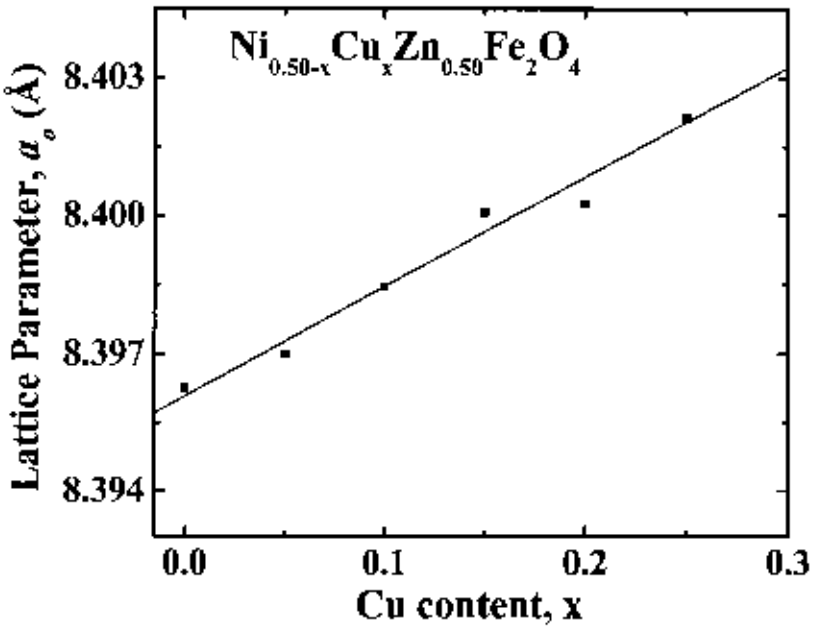

Fig 5.2: The variation of Lattice parameter with copper content (x) for $Ni_{0.50-x}Cu_xZn_{0.50}Fe_2O_4$

The dependence of lattice parameter on the copper content follows Vegards' law as observed in some spinel type materials [4].

5.1.2 Microstructural analysis of $Ni_{0.50-x}Cu_xZn_{0.50}Fe_2O_4$

The optical micrographs of various $Ni_{0.50-x}Cu_x\ Zn_{0.50}\ Fe_2O_4$ samples sintered at 1250°C are shown in Figs. 5.3 and 5.4. From these micrographs it is revealed that Cu^{2+} substitutions have significant influence on microstructures of *Ni-Cu-Zn* ferrites. The average grain size increases as the copper content increases up to x=0.15 and for higher copper content (x>0.15) in the $Ni_{0.50-x}Cu_xZn_{0.50}Fe_2O_4$ grain size decreases. For x=0.10 and x=0.15 formation of exaggerated grains of non-uniform size is seen to occur.

Fig. 5.3. The optical micrographs of $Ni_{0.50-x}Cu_xZn_{0.50}Fe_2O_4$ samples sintered at temperatures 1250°C.

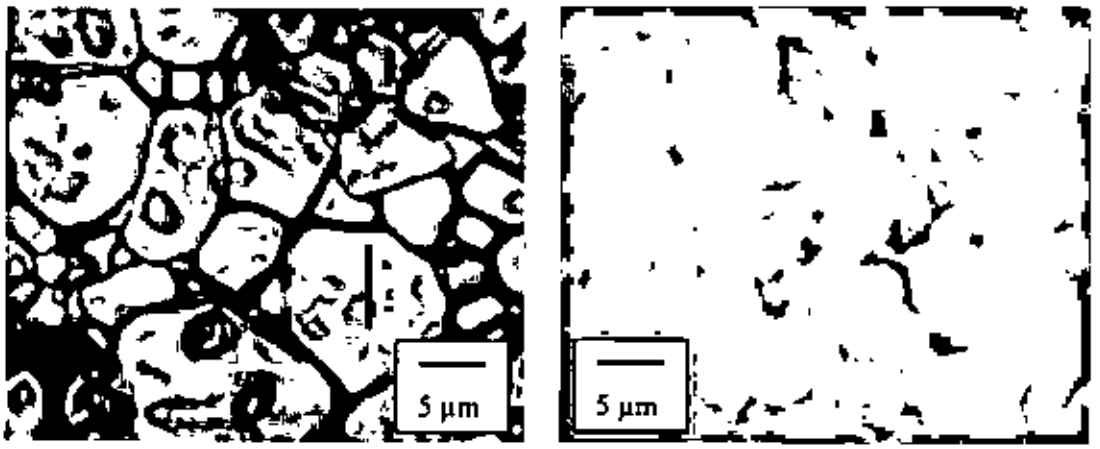

Fig. 5.4 The optical micrographs of $Ni_{0.50-x}Cu_xZn_{0.50}Fe_2O_4$ samples sintered at temperatures 1250 °C.

The average grain size increases gradually with increase of Cu^{2+} may be due to the fact that melting point of copper (1357K) is less than that of nickel (1726K) and the decreases in grain size beyond x=0.15 perhaps related to complicated chemistry of copper (higher concentration) with other materials [5]. Similar behaviour is observed by Hoque *et al* in $Ni_{1-x}Cu_xFe_2O_4$ [6]. The average grain size is highest for $Ni_{0.35}Cu_{0.15}Zn_{0.50}Fe_2O_4$ .It is also found that the sintering temperatures have influence on grain size for a particular composition. It is noticed that the average grain size of all samples increases with the sintering temperatures as presented in Table 5.1. During the early stage of sintering temperature, the volume fraction of pores is large and the grain growth is inhibited. Once the porosity decreases as the sintering temperature increases many of small pores disappear. The grain that grows, consume their neighbor and become larger. The behavior of grain growth reflects the competition between the driving force for grain boundary movement and the retarding force exerted by pores [7].

5.1.3 Density and porosity

X-ray density, bulk density and porosity of various $Ni_{0.50-x}Cu_xZn_{0.50}Fe_2O_4$ are tabulated in the Table-5.1 The bulk density ρ_B of each composition of $Ni_{0.50-x}Cu_xZn_{0.50}Fe_2O_4$ was measured by Archimede's principle using water and X-ray density of each sample were calculated using Eq-4.4 and Eq-4.5, respectively. The porosity of these samples were calculated using the relation $\{100(\rho_{th}-\rho_B)/\rho_{th}\}\%$, where ρ_B is the bulk density.

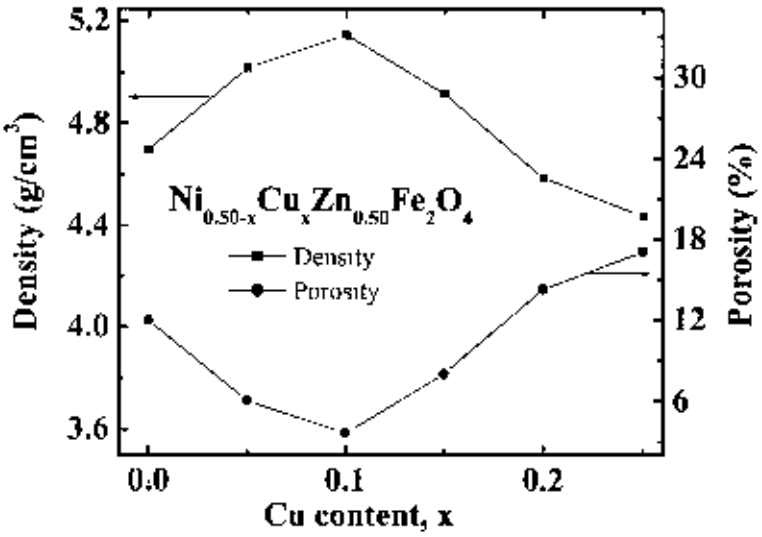

Fig 5 5: Density and Porosity plotted against Cu content for $Ni_{0.50-x}Cu_xZn_{0.50}Fe_2O_4$ sintered at 1150°C

From fig. 5.5 it is noticed that the bulk density increases with increasing copper content up to x=0.10 in the $Ni_{0.50-x}Cu_xZn_{0.50}Fe_2O_4$ Beyond this vale of x, density decreases as the copper content increases. The increase in bulk density can be attributed to the difference in atomic weight of the ferrites components. The atomic weight of Cu^{2+} (63.55 *amu*) is greater than that Ni^{2+} (58.71 *amu*) [8]. The decrease in density may be due to the intergranular/intragranular porosity resulting from discontinuous grain growth as proposed by Burke [9]. From the microstructural studies it was also observed that the average grain size increases with the increase of copper content up to x=0.15 after that grain size decreases. According to Lange and Kellet [10], grain growth and densification are intimately related.

Table 5.1. The lattice parameter, density, porosity, average grain size and natural resonance frequency of the various $Ni_{0.50-x}Cu_xZn_{0.50}Fe_2O_4$ samples sintered at different temperatures with fixed dwell time 5 h.

x	a(Å)	T_s (°C)	ρ_{th} (g/cm^3)	ρ_B (g/cm^3)	P (%)	T_N (°C)	f_r (MHz)	Grain size	μ_i' (at 100 kHz)
0.00	8 39627	1100	5.33647	4.45	16.61	266	5.36	-	97
		1150		4.70	11.92		3.22	-	206
		1200		4 78	10.43		2 50	-	295
		1250		4 80	10.05		0.72	2.25	274
		1300		4.66	12.64		0.18	3.24	449
0 05	8.39701	1100	5 34050	4.90	8.24	253	1.92	-	258
		1150		5 02	6.00		1.07	-	321
		1200		5.04	5.62		2.01	-	374
		1250		4.98	6.75		0.07	3.19	339
		1300		4.87	8.81		0.18	4.76	452
0.10	8.39846	1100	5.34318	5 07	5.11	241	0.65	-	389
		1150		5 15	3.62		0.42	-	419
		1200		5.19	2.86		3.22	-	286
		1250		4.93	7.73		0.11	23.33	364
		1300		4.52	15.4		0.48	24.61	434
0 15	8.40007	1100	5 34554	4.84	9.45	226	0.58	-	369
		1150		4.92	7.96		2.19	-	299
		1200		5.16	3.47		2.70	-	426
		1250		4 69	12.26		0.08	24 04	515
		1300		4 36	18.43		0.15	26 22	570
0.20	8.40026	1100	5.35142	3.92	26.74	210	0.87	-	350
		1150		4.59	14.22		1.23	-	320
		1200		4 99	6.75		2.19	-	341
		1250		4.41	17.59		0.10	6.12	560
		1300		3.81	28.8		0.10	8.15	878
0 25	8.40213	1100	5.35328	3.90	27.14	190	2.08	-	316
		1150		4.44	17.06		3.22	-	128
		1200		4.96	7.34		2.09	-	266
		1250		4.27	20.23		0.18	1.54	387
		1300		3.79	29.24		0.16	4.62	518

On the other hand, the value of X-ray density, ρ_{th} increases with the increases of lattice constant a_0 in the various copper substituted $Ni_{0.50-x}Cu_x Zn_{0.50} Fe_2O_4$ .It increased because the molecular weight of the each samples increases significantly with the addition of Cu^{2+} content So the X-ray density depends upon the lattice constant and the molecular weight of the samples. It can be observed from fig.5.6 that the X-ray densities are larger in magnitude than corresponding bulk densities. This may be due to the presence of pores in the samples [11].

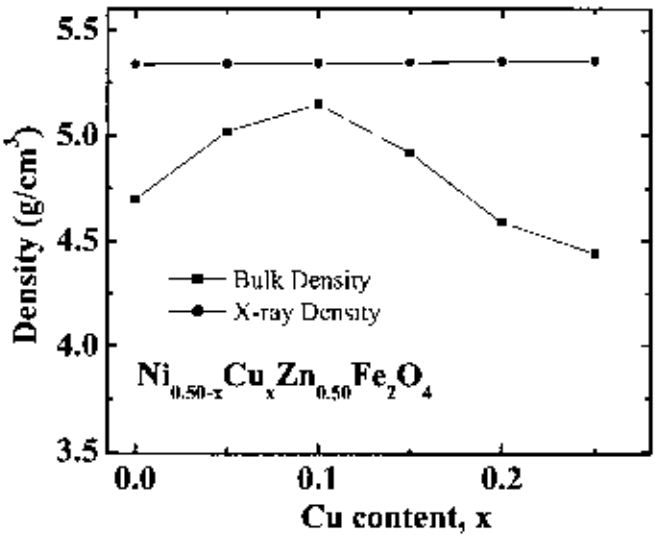

Fig.5.6 The variation of X-ray and bulk densities with Cu *content, x* for $Ni_{0.50-x}Cu_x Zn_{0.50}Fe_2O_4$

Fig 5.7 shows that the variation of bulk density of all samples increases with increasing sintering temperatures. During the sintering process, the thermal energy generates a force that drives the grain boundaries to grow over pores, thereby decreasing the pore volume and densifying the material. As a result densities increase with the increase of sintering temperature At higher sintering temperature abnormal grain growth rate is high, which trapped the pore inside the grain as a result intragranular porosity is increased. The trapped pores binder the migration of pore to the grain boundaries and hence the reduction of the sintered densities. This result agrees with the result for *NiZn* ferrites [12]. Higher temperature sintering generally brings about reduced porosity. But our observation shows that at higher temperature porosity increase which is may be due to decrease in density and less oxygen vacancies.

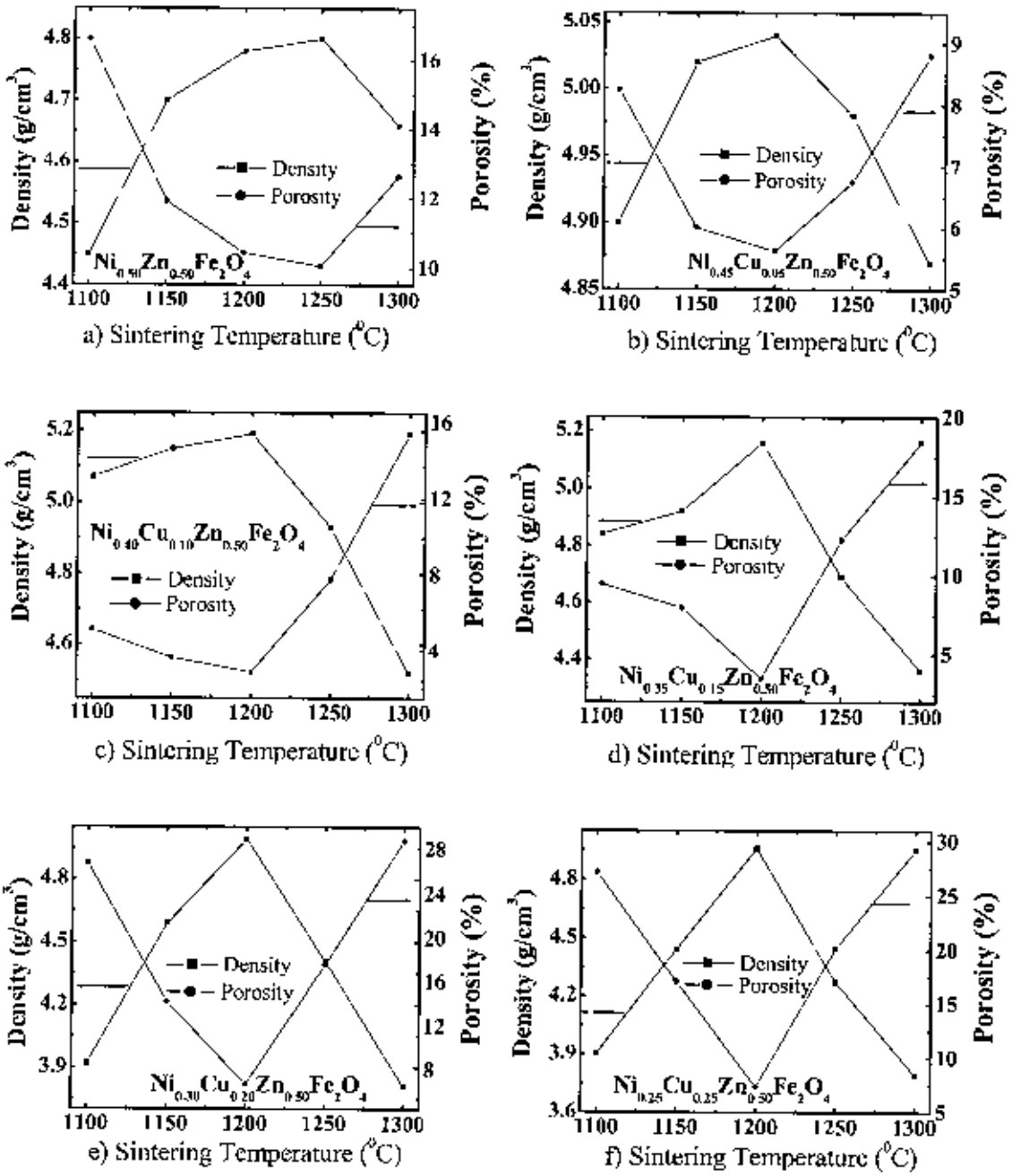

Fig 5.7: The variation of density and porosity for (a) $Ni_{0.50}Zn_{0.50}Fe_2O_4$ (b) $Ni_{0.45}Cu_{0.05}Zn_{0.50}Fe_2O_4$, (c) $Ni_{0.40}Cu_{0.10}Zn_{0.50}Fe_2O_4$, (d) $Ni_{0.35}Cu_{0.15}Zn_{0.50}Fe_2O_4$ (e) $Ni_{0.30}Cu_{0.20}Zn_{0.50}Fe_2O_4$, and (f) $Ni_{0.25}Cu_{0.25}Zn_{0.50}Fe_2O_4$.

5.1.4 Average particle size of $Ni_{0.50-x}Cu_xZn_{0.50}Fe_2O_4$

The average particle size was estimated by using Debye-Scherrer formula from the broadening of the highest intensity peaks (311) of spinel [13]

$$D = \frac{0.9\lambda}{\beta \cos\theta}$$

where, D is the average particle size, λ is the wavelength of the radiation used as the primary beam of Cu K_α (λ=1.54178 Å), θ is the angle of the incident beam in degree and β is the full width at half maximum (FWHM) of the fundamental reflection (311) in radian of the FCC ferrites phase.Debye-Scherrer's formula assumes approximation and gives the average particle size if the grain size distribution is narrow and strain induced effects are quite negligible.

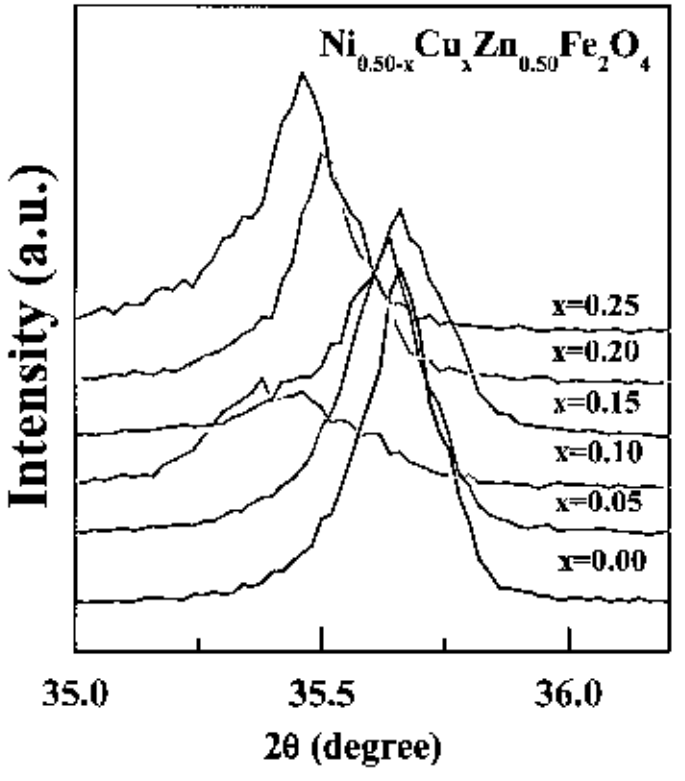

Fig 5 8 XRD patterns of (311) peak with Cu *content, x* for $Ni_{0.50-x}Cu_xZn_{0.50}Fe_2O_4$ nano particles

Fig. 5.8 show the XRD patterns of $Ni_{0.50-x}Cu_xZn_{0.50}Fe_2O_4$ ferrites annealed at 900°C for 5 h,where (311) peak is shown in expanded form to understand the variation of FWHM of the Bragg peaks with the copper content. From this figure it is seen that the value of FWHM decreases with increasing copper content. The particle size of the sample is

inversely proportional to FWHM according to Debye-Scherrer formula. The observed particle size is in the range 0.22nm to 0.73nm which are listed in the Table5.2.

Table 5.2: Particle size and FWHM of $Ni_{0.50-x}Cu_xZn_{0.50}Fe_2O_4$ samples

x	FWHM (in degree)	Particle size (nm)
0.00	0.19	0.46
0.05	0.12	0.73
0.10	0.39	0.22
0.15	0.36	0.24
0.20	0.18	0.48
0.25	0.18	0.48

5.1.5 Complex permeability of $Ni_{0.50-x}Cu_xZn_{0.50}Fe_2O_4$

The compositional variation of complex permeability spectra for the $Ni_{0.50-x}Cu_xZn_{0.50}Fe_2O_4$ samples sintered at 1100°C, 1150°C, 1200°C, 1250°C, and 1300°C are shown in Figs.5.9, 5.10, 5.11, 5.12 and 5.13, respectively. The initial permeability (μ_i') increase with increasing Cu^{2+} content up to x=0.10, because of increase in density and grain size with Cu^{2+} content. Beyond this value of x, initial permeability decrease with increasing Cu^{2+} content. The general characteristic of the permeability spectra is that the real part of initial permeability (μ_i') remain fairly constant in a certain frequency range, while at higher frequency it drops rapidly to a very small value and there is a increase of imaginary part (μ_i''). The μ_i'' arises due to the lagging of the motion of the domain walls with the applied alternating magnetic field. This behaviour resembles a typical relaxation character. It may be due to reversible displacement of domain walls [14].

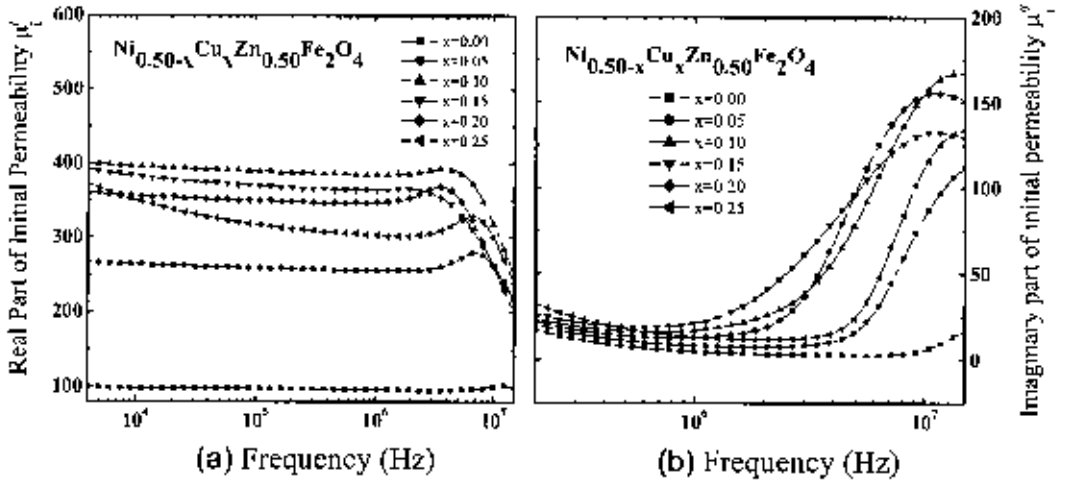

Fig.5.9: (a) The real μ_i' and (b) imaginary permeability μ_i'' spectra for $Ni_{0.50-x}Cu_xZn_{0.50}Fe_2O_4$ samples sintered at temperatures 1100°C in air

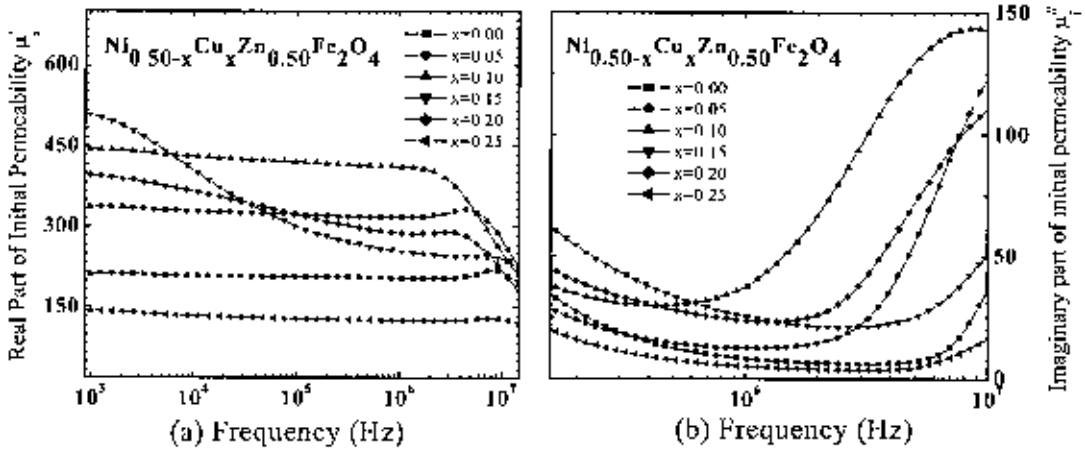

Fig.5.10 (a) The real μ_i' and (b) imaginary permeability μ_i'' spectra for $Ni_{0.50-x}Cu_xZn_{0.50}Fe_2O_4$ samples sintered at temperatures 1150°C in air

The initial (μ_i') permeability increase with increasing sintering temperature because of increase of grain size with temperature. The permeability of polycrystalline ferrite is related to two different magnetizing mechanisms: spin rotation and domain wall motion [15, 16], which can be described as, $\mu_i = 1 + \chi_w + \chi_{spin}$, where χ_w is the domain wall susceptibility, χ_{spin} is intrinsic rotational susceptibility. χ_w and χ_{spin} may be written as: $\chi_w = 3\pi M_s^2 D / 4\gamma$ and $\chi_{spin} = 2\pi M_s^2 / K_u$ with M_s saturation magnetization, K_u the total anisotropy, D the grain diameter, and γ the domain wall energy. Thus, the

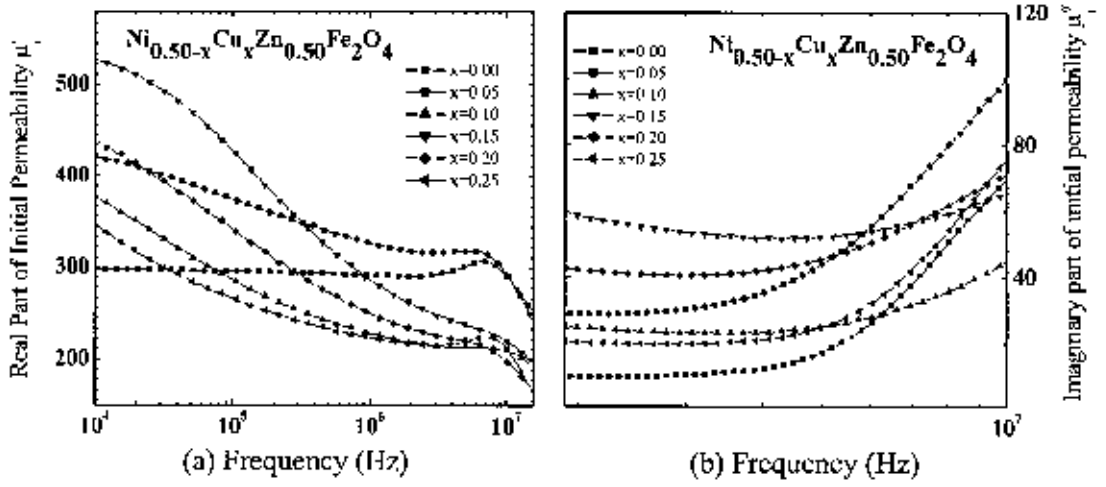

Fig 5.11 (a) The real μ_i' and (b) imaginary permeability μ_i'' spectra for $Ni_{0.50-x}Cu_xZn_{0.50}Fe_2O_4$ samples 1200°C in air.

domain wall motion is affected by the grain size and enhances with the increase of grain size. The initial permeability is therefore a function of grain size. Larger grains tend to consist of a greater number of domain walls. The magnetization caused by domain wall movement requires less energy than that required by domain rotation. As the number of walls increases with the grain sizes, the contribution of wall movement to magnetization is increased. In our experiment, the grain size is enriched by the more content of Cu^{2+} in the

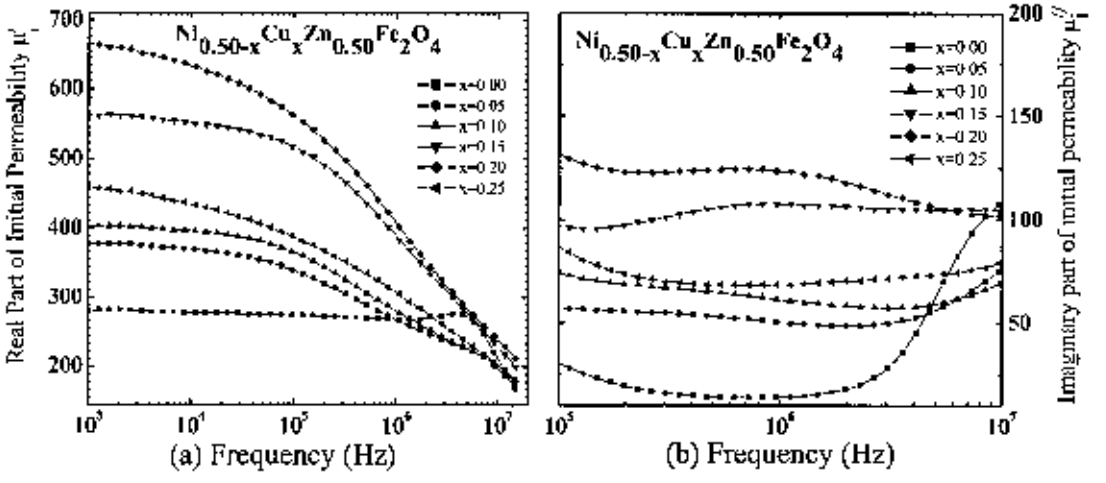

Fig 5.12 (a) The real μ_i' and (b) imaginary permeability μ_i'' spectra for $Ni_{0.50-x}Cu_xZn_{0.50}Fe_2O_4$ samples sintered at temperatures 1250°C in air

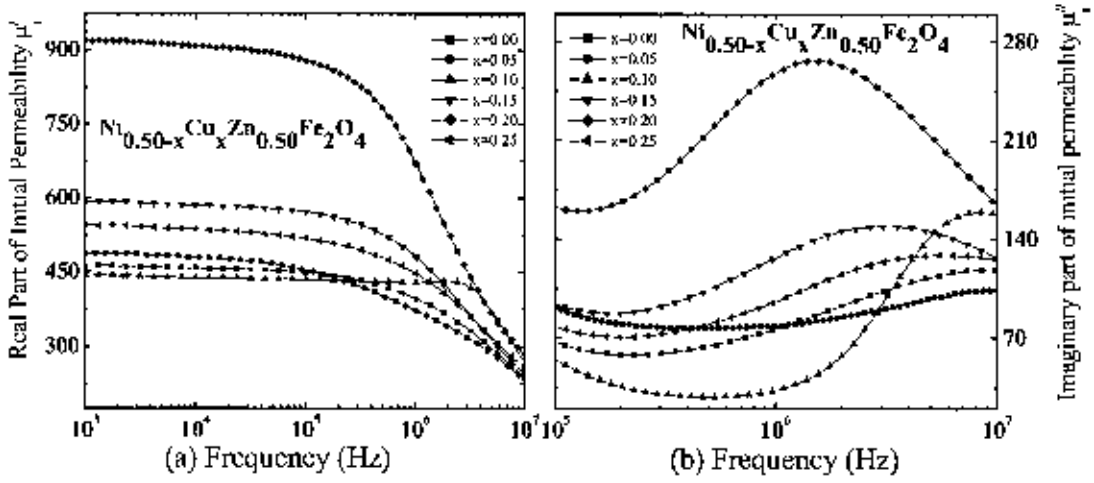

Fig 5.13 (a) The real μ_i' and (b) imaginary permeability μ_i'' spectra for $Ni_{0.50-x}Cu_xZn0.50Fe_2O_4$ samples sintered at temperatures 1300°C in air.

the samples up to a certain level. Similar result reported for others materials by Hossain *et.al* [17]

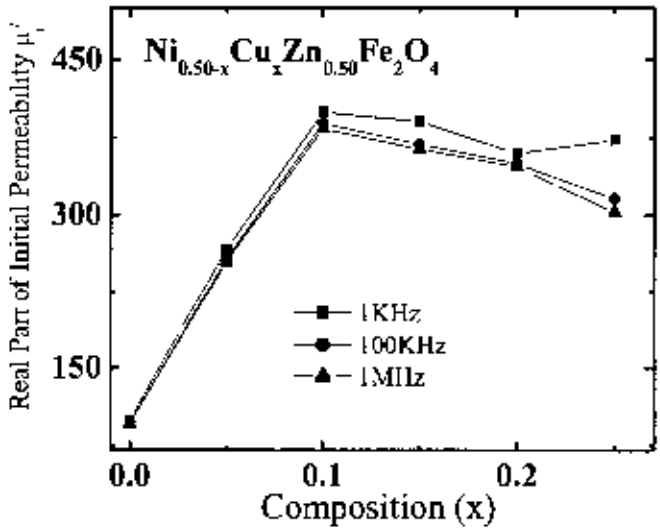

Fig 5.14 Compositional variation of initial permeability (μ_i') of $Ni_{0.50-x}Cu_xZn_{0.50}Fe_2O_4$ ferrites with frequencies

Fig. 5.14 show the variation of permeability at different frequencies with Cu^{2+} content in the $Ni_{0.50-x}Cu_xZn_{0.50}Fe_2O_4$ ferrites. It shows a decrease trend in permeability with the increasing of frequency. This is because at higher frequencies nonmagnetic impurities between the grains and intra granular pores act as pinning points and increasingly hinder

the motion of spin and domain walls thereby decreasing their contribution to permeability and also increasing the loss [18].

Energy loss is an extremely important subject in soft ferrimagnetic materials, since the amount of energy wasted on process other than magnetization can prevent the AC applications of a given material. The ratio of μ_i' and μ_i'' representing the losses in the material are a measure of the inefficiency of the magnetic system. Obviously this parameter should be as low as possible. The magnetic losses, which cause the phase shift, can be split up into three components: hysteresis losses, eddy current losses and residual losses. This give the formula $\tan\delta_m = \tan\delta_h + \tan\delta_e + \tan\delta_r$. The μ_i is initial permeability which is related to low applied magnetic field. Hysteresis losses vanish at very low field strengths. Thus at low field the remaining magnetic losses are due to eddy current losses and residual losses. Residual losses are independent of frequency. Eddy current losses increase with frequency and are negligible at very low frequency. Eddy current loss can be expressed as $P_e \approx f^2/\rho$, where P_e is the energy loss per unit volume and ρ is the resistivity [19,20]. To keep the eddy current losses constant as frequency is increased; the resistivity of the material chosen must increase as the square of frequency. Eddy currents are not problem in the *Ni-Zn* ferrites until higher frequencies are encountered because they have very high resistivity about $10^5 \Omega cm$ to $10^8 \Omega cm$ [21]. The ferrite microstructure is assumed to consist of grains of low resistivity separated by grain boundaries of high resistivity. Thicker grain boundaries are preferred to increase the resistance.

Figs. 5.15 and 5.16 shows the variations of loss factors with frequency of different compositions of the samples sintered at different sintering temperature, T_s. Loss factors are minimum for frequency up to 1 MHz (depending on compositions and T_s).

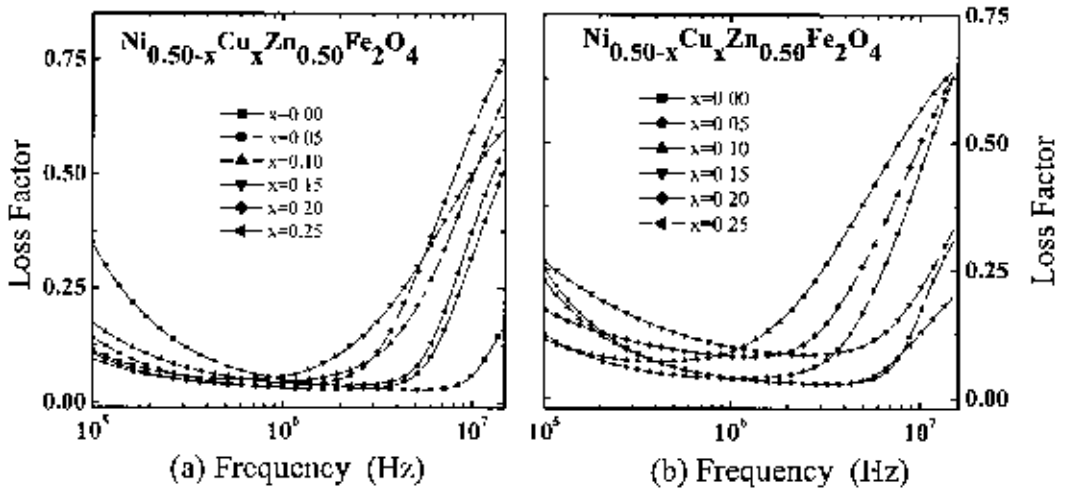

Fig 5.15 The variation of Loss factor with frequency $Ni_{0.50-x}Cu_xZn_{0.50}Fe_2O_4$ samples at (a) 1100° C and (b) 1150° C

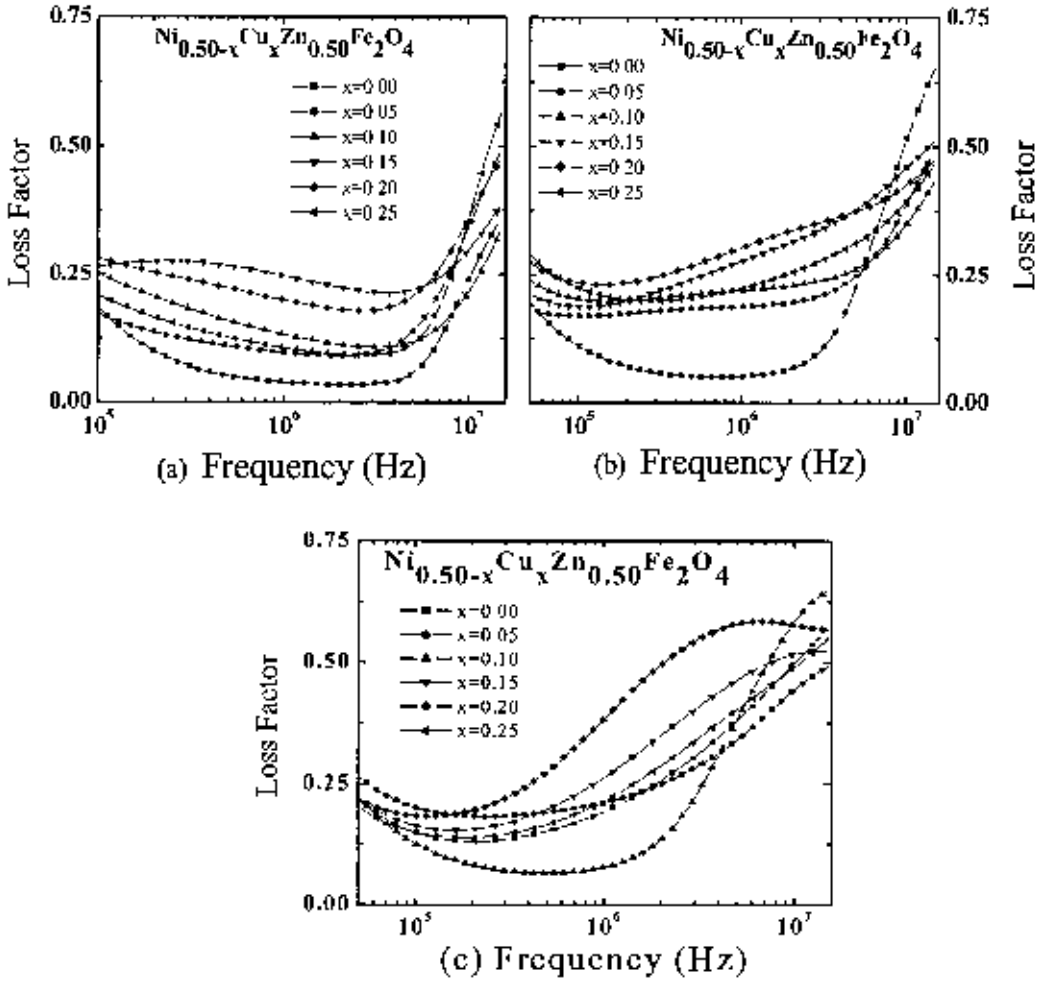

Fig 5.16. The variation of Loss factor with frequency $Ni_{0.50-x}Cu_xZn_{0.50}Fe_2O_4$ samples at (a) 1200° C, (b) 1250° C and (c) 1300° C

Relative quality factor (Q factor) for all samples sintered at various temperatures have been calculated from the quality factor and loss factor. Fig. 5.17 and 5.18 shows the variation of Q factor with frequency which reveal that Q-factor increases with an increase of frequency showing a peak and then decreases with further increase of frequency.

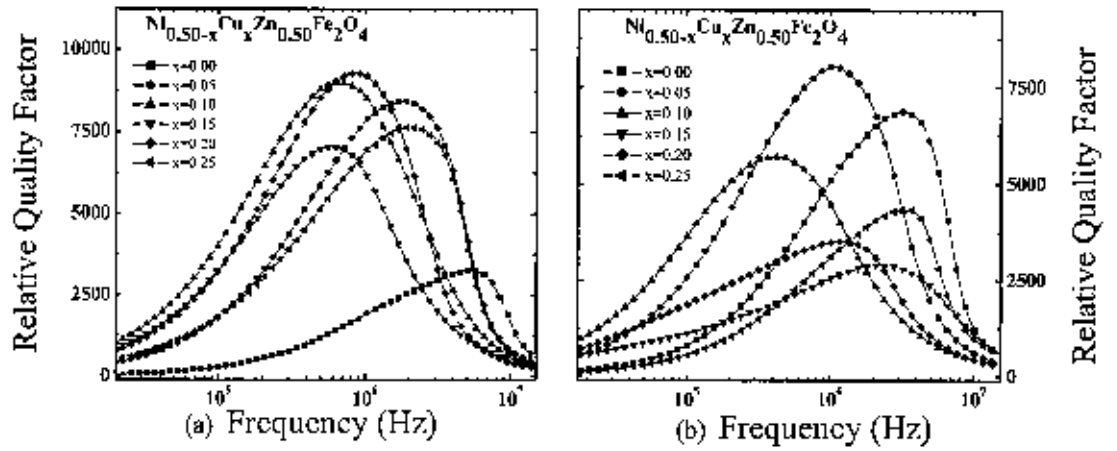

Fig. 5.17: The variation of Quality factor with frequency for $Ni_{0.50-x}Cu_xZn_{0.50}Fe_2O_4$ samples sintered at (a) 1100°C and (b) 1150°C

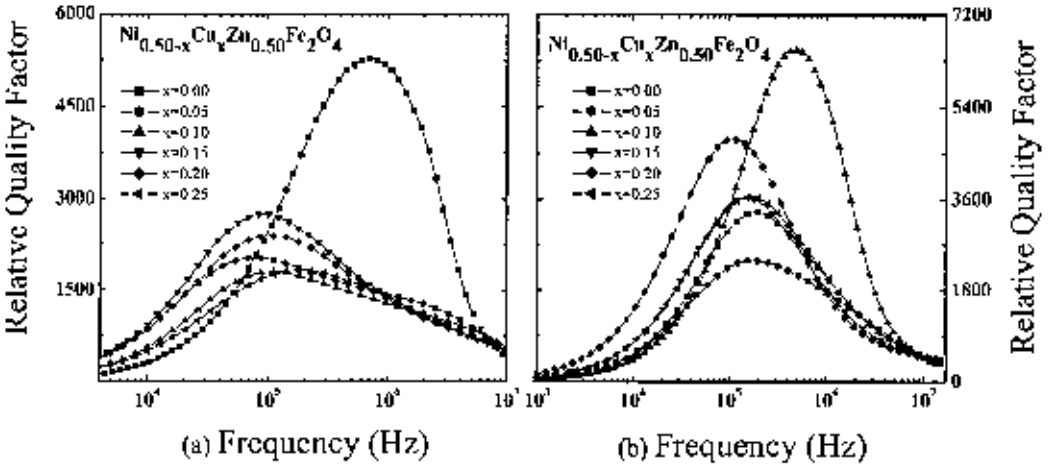

Fig. 5.18: The variation of Quality factor with frequency for $Ni_{0.50-x}Cu_xZn_{0.50}Fe_2O_4$ samples sintered at (a) 1250°C and (b) 1300°C

5.1.6. Temperature-dependent permeability and Néel temperature

The μ_i' as a function of temperature for various $Ni_{0.50-x}Cu_xZn_{0.50}Fe_2O_4$ sintered at 1250°C is shown in Fig. 5.19. The μ_i' is measured at a constant frequency (100 kHz) of a sinusoidal wave. Permeability falls rapidly when the magnetic state of the ferrite samples changes from ferrimagnetic to paramagnetic. The sharp falling of μ_i' with temperature suggests that the single-phase formation of these ferrite [22], which have been confirmed by X-ray diffraction (Section 5.1.1). The Néel temperature, T_N, is determined by drawing a tangent for the curve at the rapid decrease of μ_i'. The intersection of the tangent with the temperature axis determines T_N. From these curves the T_N's of these samples are determined and tabulated in the Table.5.1.

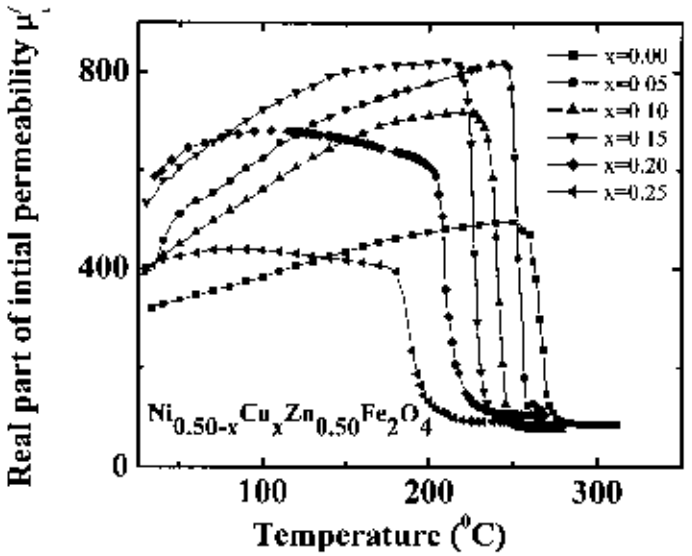

Fig. 5.19: The temperature dependence of μ_i' for $Ni_{0.50-x}Cu_xZn_{0.50}Fe_2O_4$ sintered at 1250°C.

It is revealed from Fig. 5.19 that when Cu^{2+} is substituted in $Ni_{0.50-x}Cu_xZn_{0.50}Fe_2O_4$ (with x = 0.00, 0.05, 0.10, 0.15, 0.20 and 0.25), T_N decreases. The decrease of the Néel temperature with Cu^{2+} substitution is due to the weakening of the *A-B* interaction correspondingly between two sublattices. This could be attributed to the increase in distance (hopping length, *L*) between the magnetic ions of tetrahedral A- site (L_A) and the octahedral B-sites (L_B), which is shown in Figure.5.20. This is also confirmed by the increase in the lattice parameter with increasing Cu^{2+} contents.

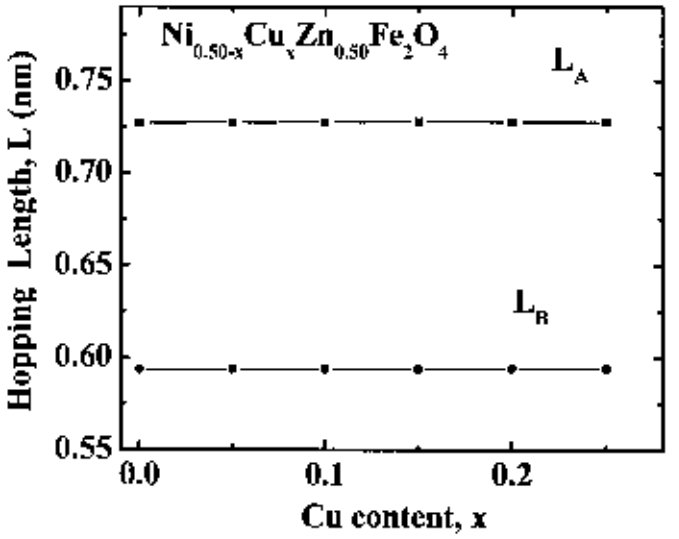

Fig 5.20: The plot of hopping length L in A-site and B-site (L_A and L_B) against Cu^{2+} concentration

It known that the vertical drop of the permeability at the transition temperature indicates the degree of homogeneity in the sample [19].so our samples have shown an excellent degree of homogeneity. Further increasing temperature permeability becomes smaller and independent of temperature i.e. paramagnetic behaviour.The peak near T_N is known as the '*Hopkinson*' peak [19] which indicates the presence of single domain (SD) in the sample Hence it concluded that there is no presence of SD grains in our samples. The variation in μ_i' in our sample appears to be mainly due to variation of magnetocrystalline anisotropy constant and the grain size. Anisotropy constants vary considerably with temperature. In most cases, anisotropy decreases steeply from a high value at low temperature and then slowly decreases down to zero at T_N [19]. There is then no preferred crystallographic direction for the magnetization of a domain. It is observed that the initial permeability, μ_i', increases with temperature to a maximum value just below the T_N . This occurs, because the crystal anisotropy normally decreases with increasing temperature [21]. The initial permeability varies as $\mu_i \approx M_S^2 / K_1^{1/2}$ [19]. Since anisotropy decreases faster than magnetization on heating, the initial permeability expectantly increases with temperature, tends to infinity just below the T_N and then drops for the paramagnetic phase.

5.1.7 DC Magnetization of $Ni_{0.50-x}Cu_xZn_{0.50}Fe_2O_4$

The magnetization as a function of applied magnetic field, *M-H*, for various $Ni_{0.50-x}Cu_xZn_{0.50}Fe_2O_4$ (with x = 0.00, 0.05, 0.10, 0.15, 0.20 and 0.25) samples at room temperature (300K) are shown in Fig. 5.21. The magnetization of all samples increases linearly with increasing the applied magnetic field up to 0.2T. Beyond 0.2T applied field magnetization increases slowly and then saturation occurs. The magnetization curve shift to lower values as Cu^{2+} content increasing up to x=0.15,beyond this value of x, magnetization increase as the copper content increase. Magnetization decrease since the

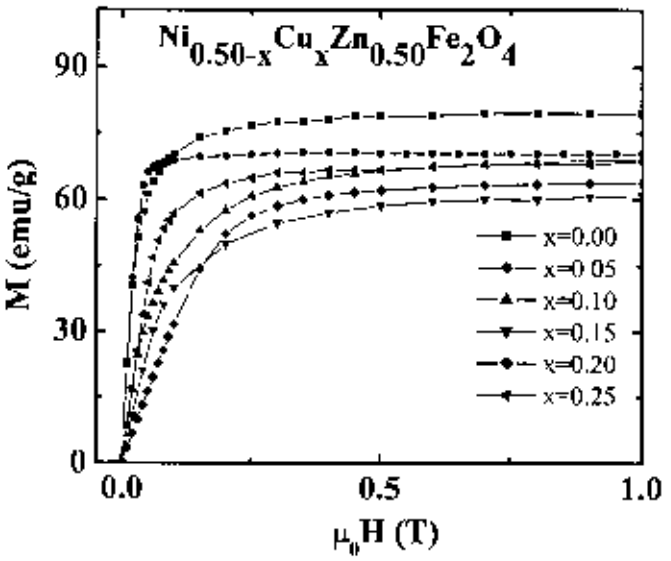

Fig 5.21 The magnetization (*M*) versus the applied magnetic field (*H*) curves for $Ni_{0.50-x}Zn_{0.50}Cu_xFe_2O_4$ samples sintered at 1250°C for 5 h in air

magnetic moment of the Cu^{2+} is lesser than that Ni^{2+}, resulting the decrease of the A-B interaction as well as net magnetization. There is strong evidence that Cu^{2+} change to Cu^{+} at higher copper concentration [23]. The Cu^{+} has a preference to accommodate themselves in A-sites which Cu^{+} can force some of Fe^{3+} migrate from A-sites to B-sites. This migration of Fe^{3+} to B-sites will lead to an increase in magnetization in B-sites leading to the increase of the saturation magnetization. Similar results were reported by other researcher [23]. The saturation magnetization, M_s for all the samples determined by the extrapolation of the MH plots to $\mu_0 H_c$=0. The saturating magnetizing value, $\mu_0 H_s$, saturation magnetization, M_s, and the number of Bohr magneton, μ_B of the ferrites

Table 5.3. The saturation magnetization and Bohr magneton of $Ni_{0.50-x}Cu_xZn_{0.50}Fe_2O_4$ samples sintered at 1250°C

x	The field at which saturation occurs, $\mu_0 H_s$ (Tesla)	M_s (emu/g)	n (μ_B)
0.00	0.2	75.35	3.20
0.05	0.15	69.53	2.96
0.10	0.35	64.04	2.73
0.15	0.5	58.53	2.50
0.20	0.4	60.92	2.60
0.25	0.3	66.01	2.82

$Ni_{0.50-x}Cu_xZn_{0.50}Fe_2O_4$ samples are tabulated in the Table 5.3. The distribution of cations in A and B- sites influences the magnetic properties.

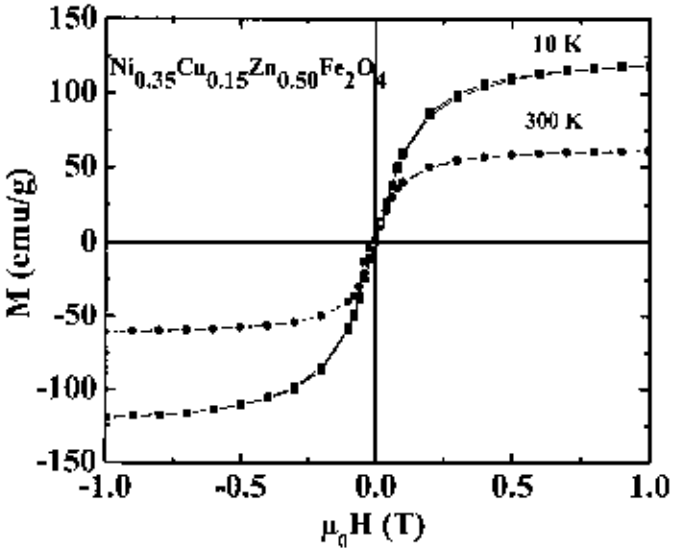

Fig 5.22 The magnetization as a function of applied magnetic field plots for $Ni_{0.35}Cu_{0.15}Zn_{0.50}Fe_2O_4$ measured at 10K and 300 K

The magnetization as a function of applied magnetic field, *M(H)*, for $Ni_{0.35}Cu_{0.15}Zn_{0.50}Fe_2O_4$ is measured both at room temperature (300K) and 10K as shown in Fig. 5.22. The magnetization of $Ni_{0.35}Cu_{0.15}Zn_{0.50}Fe_2O_4$ increases linearly with increasing the applied magnetic field up to 0.3T at both the temperatures and attains its saturation

value for fields higher than 0.3T. The 97% of saturation is observed at 0.5 T applied magnetic filed at room temperature. The saturation magnetization at 10 K for $Ni_{0.35}Cu_{0.15}Zn_{0.50}Fe_2O_4$ is 113 emu/g.

5.2 Investigation of polycrystalline $Ni_{0.45-x}Cu_{(x+y)}Zn_{0.55-y}Fe_2O_4$

5.2.1 X-ray diffraction analysis

The XRD patterns for the $Ni_{0.45-x}Cu_{(x+y)}Zn_{0.55-y}Fe_2O_4$ (with x = 0.00, 0.05, 0.10 and y = 0.00, 0.10, 0.10) ferrites sintered at 1200° C are shown in Fig. 5.23. The result indicated that the material has a well defined single crystalline phase and formation of spinel structure for each composition of Ni-Cu-Zn ferrites. Analyzing the XRD patterns we detect that the positions of the peaks comply with the reported value [1] and no traces of raw materials were found, there by confirming that the chemical reaction is completed.

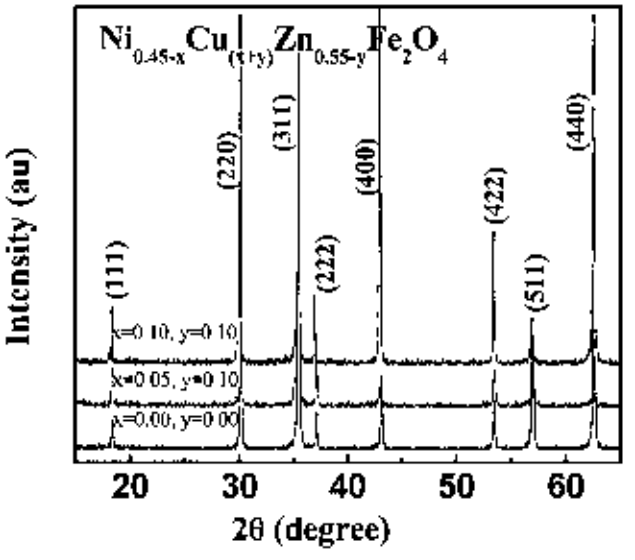

Fig.5.23: The X-ray diffraction patterns for $Ni_{0.45-x}Cu_{(x+y)}Zn_{0.55-y}Fe_2O_4$

The lattice constant a_0 is plotted against the copper concentration (x+y) in the Fig.5.24. It is noticed from this figure that the lattice parameter decreases with increasing Cu^{2+} substitution in $Ni_{0.45-x}Cu_{(x+y)}Zn_{0.55-y}Fe_2O_4$. The decrease in lattice parameter with increasing Cu^{2+} substitution can be explained in terms of ionic radii. The radius of Cu^{2+} (0.72 Å) is lower than that both of Ni^{2+} (0.78 Å) and Zn^{+2}(0.82 Å) [1]. Fig.5.24 shows the

variation of lattice parameter with x and y for $Ni_{0.45-x}Cu_{(x+y)}Zn_{0.55-y}Fe_2O_4$ The dependence of lattice parameter on the concentration follow Vegards' law like in some spinel[4]. The non-linear variation in lattice constant indicates the random distribution of Cu^{2+} ions in the B-site [23], since it has already been reported [24] that copper ions are present indifferent ionics states in the A and B-sites. The lattice parameter, density, porosity and natural resonance frequency of the various $Ni_{0.45-x}Cu_{(x+y)}Zn_{0.55-y}Fe_2O_4$ samples sintered at different temperatures are given in Table 5.4.

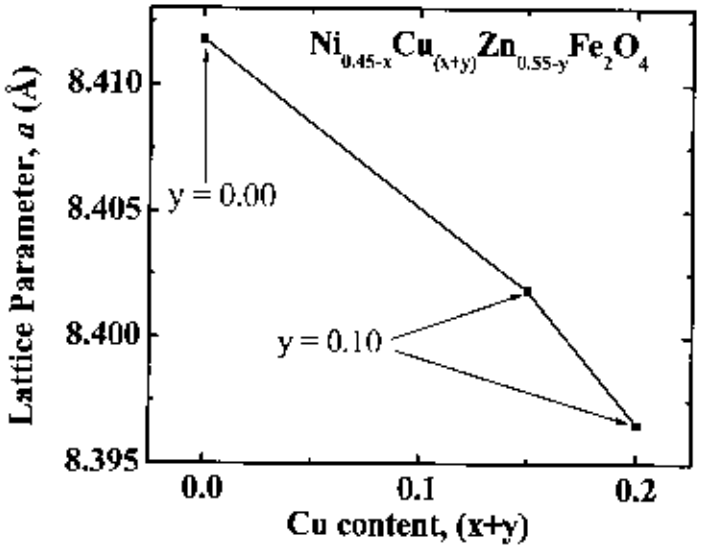

Fig 5.24: The variation of Lattice parameter with Cu *content '(x+y)'* for $Ni_{0.45-x}Cu_{(x+y)}Zn_{0.55-y}Fe_2O_4$

Table 5.4: The lattice parameter, density, porosity, average grain size and natural resonance frequency of the $Ni_{0.45-x}Cu_{(x+y)}Zn_{0.55-y}Fe_2O_4$ samples sintered at various temperatures with fixed dwell time 5 h.

x	y	a(Å)	T_s (°C)	ρ_{th} (g/cm^3)	ρ_B (g/cm^3)	P (%)	T_N (°C)	f_r (MHz)	μ_i' (at 100 kHz)
0.0	0 0	8.41176	1200	5.3153	4.82	9.26	107	0 15	1055
			1250		4.86	8.51		0.04	1249
			1300		4.52	14.8		0.01	1793
0.05	0.10	8.40184	1200	5.3354	4.72	11.3	269	4.10	273
			1250		4.81	9.79		0.06	434
			1300		4.35	18.4		0.20	361
0.10	0 10	8.39653	1200	5.3510	4.25	20.5	469	7 20	105
			1250		4.34	18.7		0 83	112
			1300		3 74	30		0.14	390

5.2.2 Density and porosity:

X-ray density, bulk density and porosity of the various $Ni_{0.45-x}Cu_{(x+y)}Zn_{0.55-y}Fe_2O_4$ are tabulated in the Table 5.4.The bulk density, ρ_g of each composition of $Ni_{0.45-x}Cu_{(x+y)}Zn_{0.55-y}Fe_2O_4$ ferrites was measured by Archimede's principle using water, and X-ray density ρ_{th}, measured by using Eq-4.4 and Eq-4.5, respectively The porosity of each sample were calculated using the relation $\{100(\rho_{th}-\rho_B)/\rho_{th}\}\%$, where ρ_g is the bulk density. From Table 5.4 we may notice that the bulk density is decreasing with increasing Cu^{2+} substitution in $Ni_{0.45-x}Cu_{(x+y)}Zn_{0.55-y}Fe_2O_4$ ferrites. The decrease in bulk density can be attributed to the difference in atomic weight of the ferrites components. The atomic weight of Zn^{2+} (65.38 *amu*) is greater than that both of the Cu^{2+} (63.55 *amu*) and Ni^{2+} (58.71 *amu*) [8] Fig. 5.25 shows that the bulk density of all samples decreases with increasing Cu^{+2}content at different sintering temperatures.

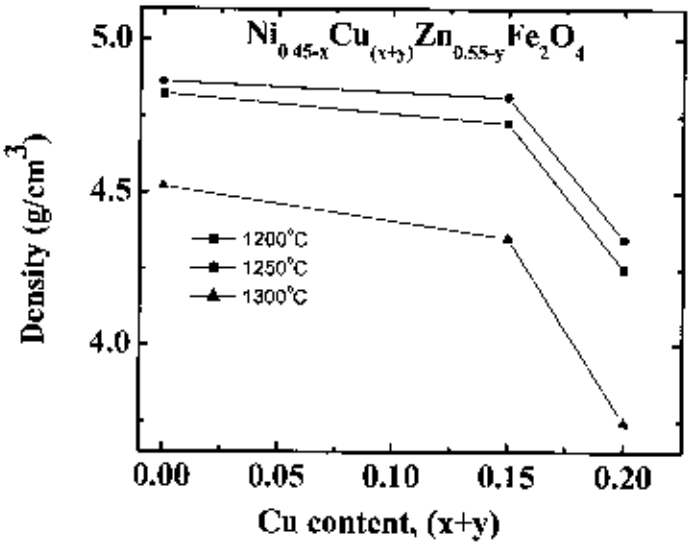

Fig.5.25: The variation of bulk density with Cu *content,(x+y)* and *temperature* for $Ni_{0.45-x}Cu_{(x+y)}Zn_{0.55-y}Fe_2O_4$.

On the other hand, the value of X-ray density ρ_{th}, increases because the lattice constant a_0 decreases with the increasing of Cu^{2+}content in the $Ni_{0.45-x}Cu_{(x+y)}Zn_{0.55-y}Fe_2O_4$. From Fig.5.26 it can be observed that the X-ray densities are larger in magnitude than corresponding bulk densities. This may be due to the presence of pores in the samples [11]. The variation of X-ray and bulk density shown is figure 5.26. Although the lattice

constant decreases non-linearly with the increase of Cu^{2+} content, yet X-ray densities vary linearly owing to the stoichiometery of the samples.

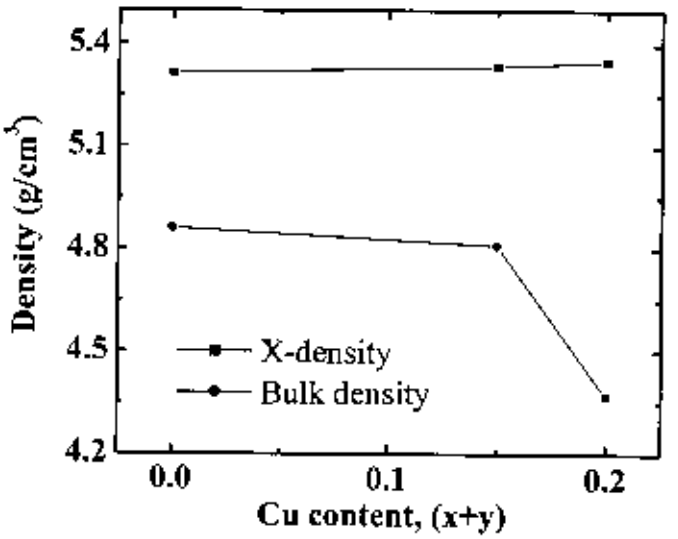

Fig.5.26 The variation of X-ray and bulk densities with Cu *content,(x+y)* for $Ni_{0.45-x}Cu_{(x+y)}Zn_{0.55}Fe_2O_4$

A plot of density and porosity Vs Cu^{2+} concentration has been plotted in fig. 5 27, which show that the density decreases as well as porosity increases by increasing Cu^{2+} content in the $Ni_{0.45-x}Cu_{(x+y)}Zn_{0.55-y}Fe_2O_4$. The increase in porosity with the addition of Cu^{2+} content may be due to the creation of more cation vacancies with the reduction of

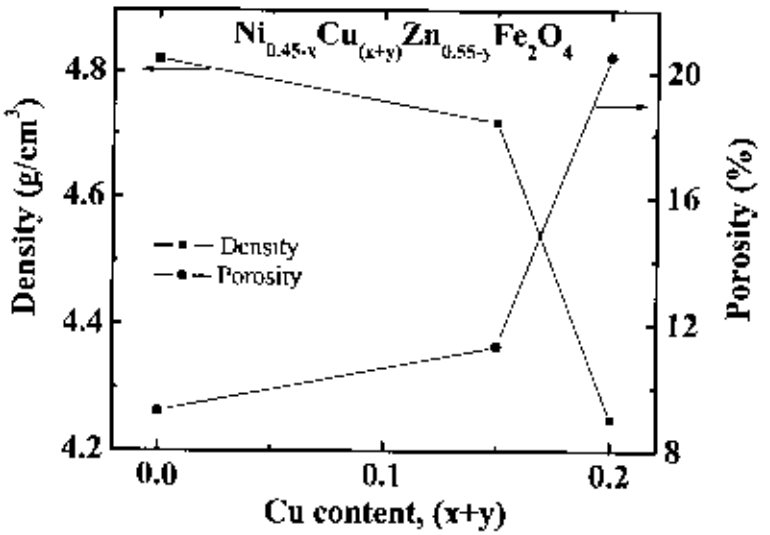

Fig 5.27. Density and porosity plotted against Cu *content,(x+y)* for $Ni_{0.45-x}Cu_{(x+y)}Zn_{0.55-y}Fe_2O_4$

oxygen vacancies [25].At higher sintering temperature abnormal grain growth rate is high, which trapped the pore inside the grain as a result intragranular porosity is increased. The trapped pores binder the migration of pore to the grain boundaries and hence the reduction of the sintered densities. This result agrees with the result for *NiZn* ferrites [12].

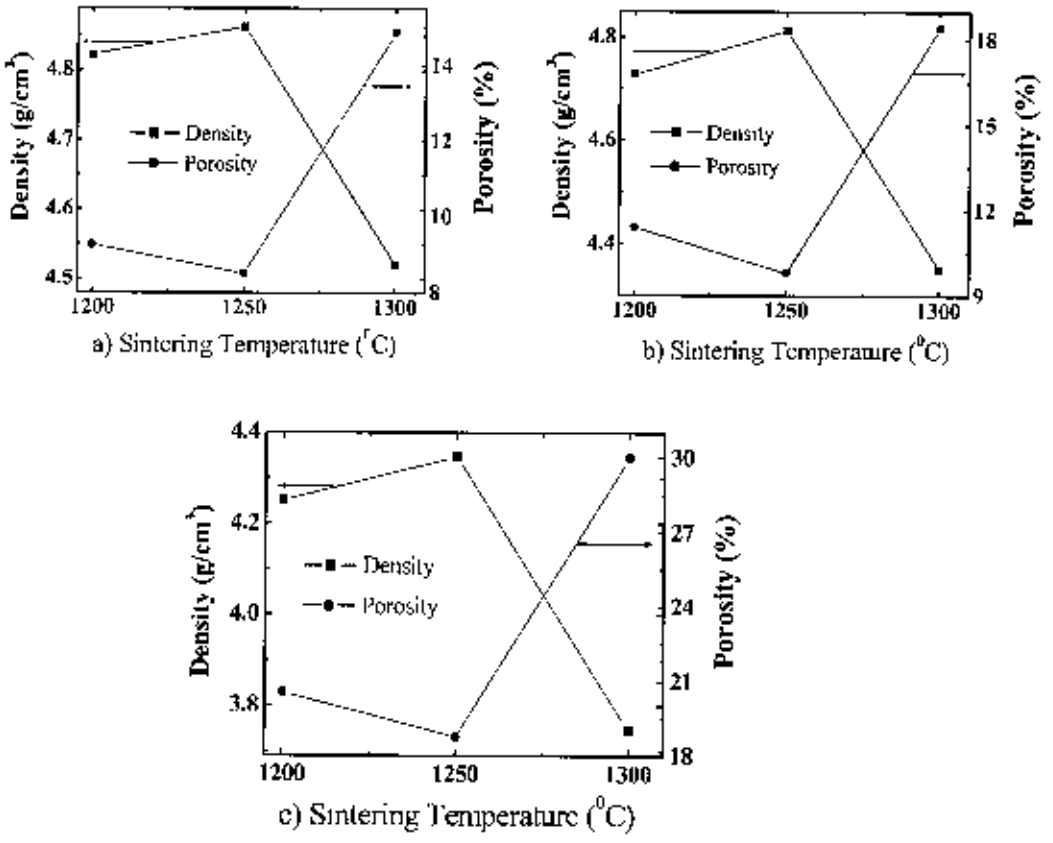

Fig.5 28: The variation of density and porosity for (a) $Ni_{0.45}Zn_{0.55}Fe_2O_4$,(b)$Ni_{0.40}Cu_{0.15}Zn_{0.45}Fe_2O_4$, and (c) $Ni_{0.15}Cu_{0.20}Zn_{0.45}Fe_2O_4$

Higher temperature sintering generally brings about reduced porosity. But our observation shows that at higher temperature porosity increase which is may be due to decrease in density and less oxygen vacancies.

5.2.3 Average particle size of $Ni_{0.45-x}Cu_{(x+y)}Zn_{0.55-y}Fe_2O_4$

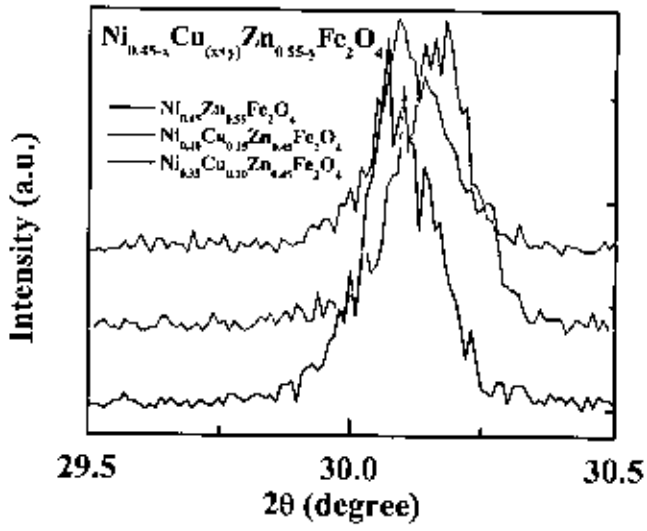

Fig 5.29: XRD patterns of (311) peak with Cu *content.(x+y)* for $Ni_{0.45-x}Cu_{(x+y)}Zn_{0.55-y}Fe_2O_4$ nano particles

Figure 5.29 show the XRD patterns of $Ni_{0.45-x}Cu_{(x+y)}Zn_{0.55-y}Fe_2O_4$ferrites anncaled at 900°C for 5 h, where (311) peak is shown in expanded form to understand the variation of FWHM of the Bragg peaks with the copper content. From this figure it is seen that the value of FWHM increases first and then decreases with increasing copper content. The particle size of the sample is inversely proportional to FWHM according to Debye-Scherrer formula which is described in the section 5 1.4. The observed particle size is in the range 0.58 nm to 0.67 nm which are listed in the Table 5.5.

Table 5.5: Particle size and FWHM of $Ni_{0.45-x}Cu_{(x+y)}Zn_{0.55-y}Fe_2O_4$ samples

x	y	FWHM (in degree)	Particle size (nm)
0.00	0.00	0.13	0.67
0.05	0.10	0.15	0.58
0.10	0.10	0.14	0 62

5.2.4 Complex permeability of $Ni_{0.45-x}Cu_{(x+y)}Zn_{0.55-y}Fe_2O_4$

Figs. 5.30, 5.31 and 5.32 show the complex permeability spectra for $Ni_{0.45-x}Cu_{(x+y)}Zn_{0.55-y}Fe_2O_4$ sintered at 1200°C, 1250°C and 1300°C, respectively. The initial (μ_i') and imaginary (μ_i'') permeability decreases with Cu^{2+} substitution in $Ni_{0.45-x}Cu_{(x+y)}Zn_{0.55-y}Fe_2O_4$. The μ_i' increases with increasing of sintering temperatures for $Ni_{0.45}Zn_{0.55}Fe_2O_4$ and $Ni_{0.35}Cu_{0.20}Zn_{0.45}Fe_2O_4$. In case of $Ni_{0.40}Cu_{0.15}Zn_{0.45}Fe_2O_4$ samples, μ_i' increases as sintering temperature increases up to 1250°C and above 1250°C, μ_i'

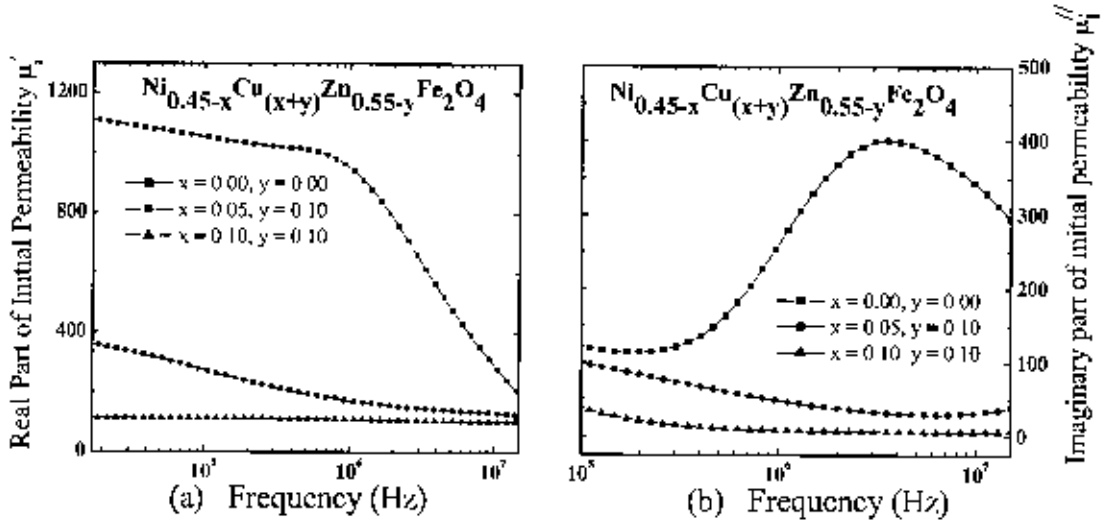

Fig 5.30: (a) The real and (b) imaginary permeability spectra for $Ni_{0.45-x}Cu_{(x+y)}Zn_{0.55-y}Fe_2O_4$ samples sintered at temperatures 1200°C in air.

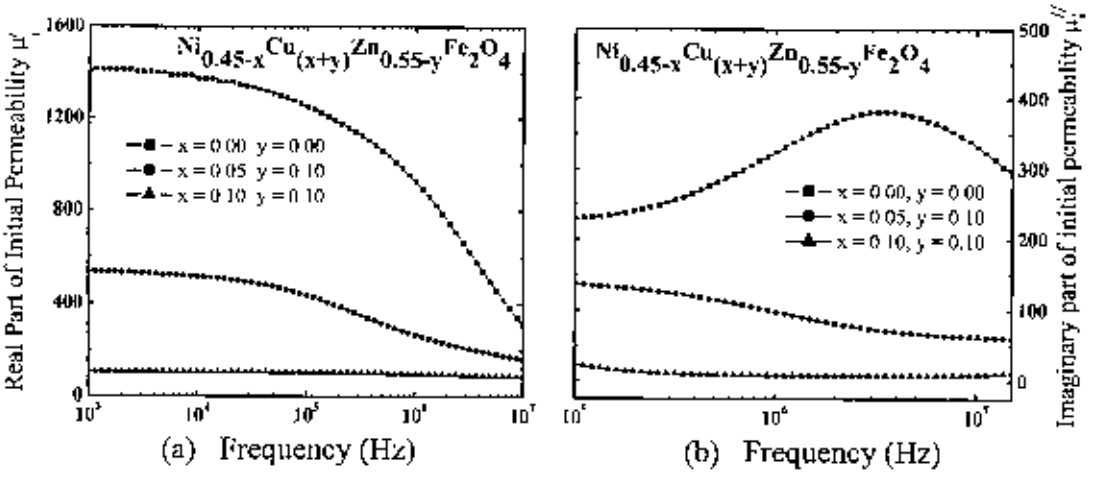

Fig 5.31: (a) The real and (b) imaginary permeability spectra for $Ni_{0.45-x}Cu_{(x+y)}Zn_{0.55-y}Fe_2O_4$ samples sintered at temperatures 1250°C in air

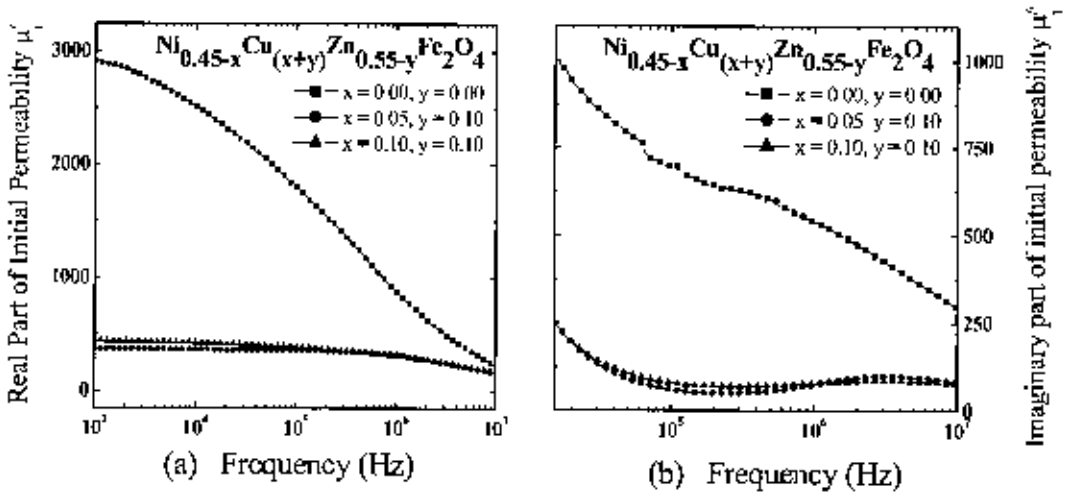

Fig. 5.32: (a) The real and (b) imaginary permeability spectra for $Ni_{0.45-x}Cu_{(x+y)}Zn_{0.55-y}Fe_2O_4$ samples sintered at temperatures 1300°C in air

decreases As sintering temperature increases, the natural resonance frequency shifted from 0.15 to 0.01 MHz for the $Ni_{0.45}Zn_{0.55}Fe_2O_4$ samples, from 4.10 to 0.20 MHz for the $Ni_{0.40}Cu_{0.15}Zn_{0.45}Fe_2O_4$ samples and from 7.2 to 0.14 MHz for the $Ni_{0.35}Cu_{0.20}Zn_{0.45}Fe_2O_4$ samples. The μ_i' of all samples are found independent of frequency below the resonance frequency. The resonance frequencies of all samples are listed in Table 5.4 We observed that for $Ni_{0.45}Zn_{0.55}Fe_2O_4$ and $Ni_{0.35}Cu_{0.20}Zn_{0.45}Fe_2O_4$, μ_i'

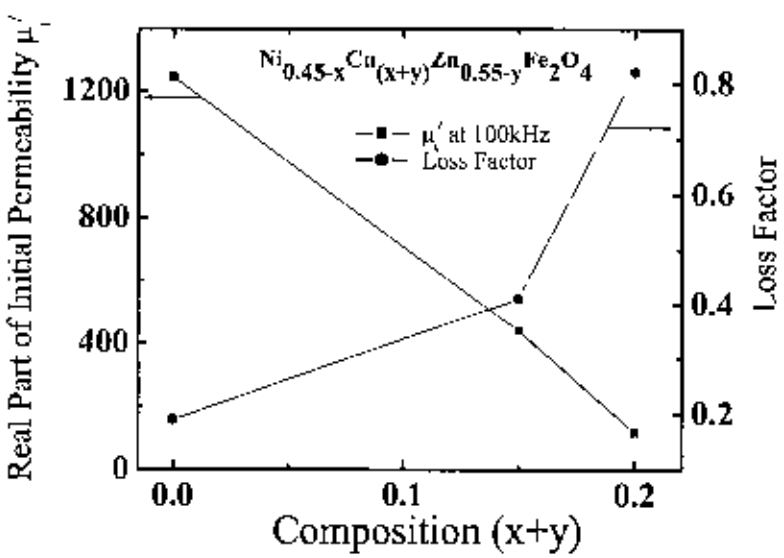

Fig: 5.33: Compositional variation of $Ni_{0.45-x}Cu_{(x+y)}Zn_{0.55-y}Fe_2O_4$ ferrites with initial permeability and loss factor at sintering temperature 1250°C in air.

is found to be maximum at maximum sintering temperature while for $Ni_{0.40}\ Cu_{0.15}\ Zn_{0.45}Fe_2O_4$ sample, at optimum T_s. The compositional variation of initial permeability and magnetic loss factor is shown in Fig.5.33.From this figure it is observed that the initial permeability (μ_i') decrease and the corresponding loss increase except for at higher sintering temperature. From Fig.5.34 we have found that the real part of initial

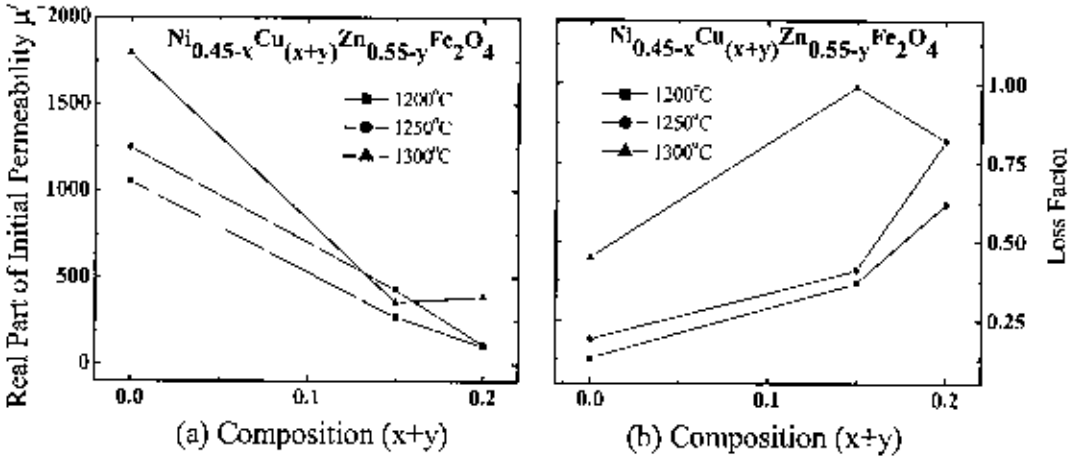

Fig. 5.34: Compositional variation of $Ni_{0.45-x}Cu_{(x+y)}Zn_{0.55-y}Fe_2O_4$ ferrites of (a) initial permeability and (b) loss factor with sintering temperature

permeability (μ_i') and loss factor increases with increasing sintering temperature for $Ni_{0.45-x}Cu_{(x+y)}\ Zn_{0.55-y}Fe_2O_4$ ferrites, except for the sample $Ni_{0.40}\ Cu_{0.15}\ Zn_{0.45}Fe_2O_4$ at higher sintering temperature, 1300°C. Fig.5.35 show the variation of permeability at different frequencies with Cu^{2+} content in the $Ni_{0.45-x}Cu_{(x+y)}Zn_{0.55-y}Fe_2O_4$. It shows a

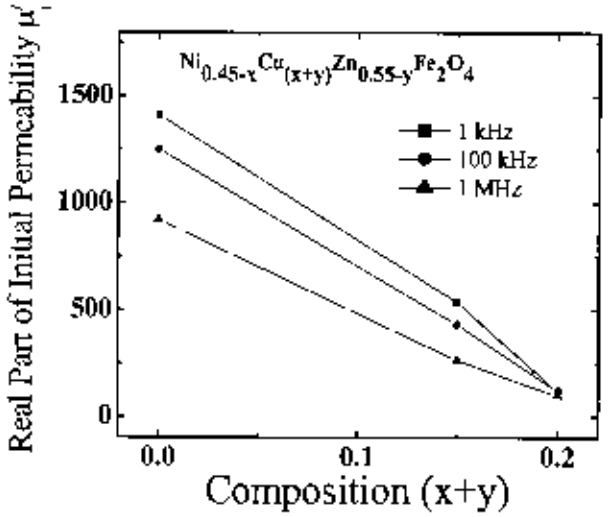

Fig. 5.35. Compositional variation of initial permeability of $Ni_{0.45-x}Cu_{(x+y)}Zn_{0.55-y}Fe_2O_4$ ferrites with frequencies

decrease trend in permeability with the increasing of frequency which is described in section 5.1.5.

Fig. 5.36 shows the variations of loss factors with frequency of different compositions of the samples sintered at different sintering temperature T_s. Loss factors are minimum for frequency up to 1 MHz (depending on compositions and T_s).

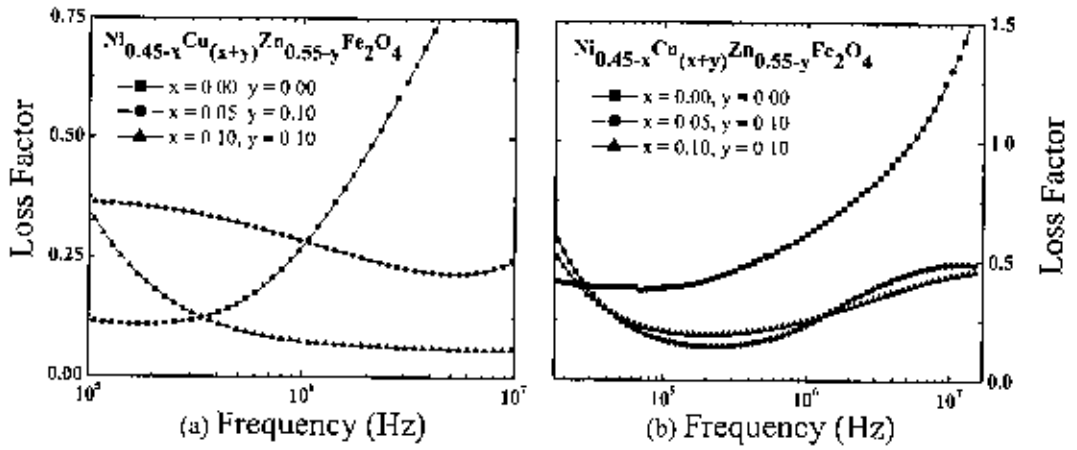

Fig. 5.36: The variation of Loss factor with frequency $Ni_{0.45-y}Cu_{(x+y)}Zn_{0.55-y}Fe_2O_4$ samples at (a) 1200°C and (b) 1300°C

Fig. 5.37 shows the variation of Q factor which reveal that it decreases with increasing of Cu^{2+} contents in $Ni_{0.45-x}Cu_{(x-y)}Zn_{0.55-y}Fe_2O_4$. It is observed that Q factor decreases for $Ni_{0.45}Zn_{0.55}Fe_2O_4$ with increasing sintered temperature but increase for $Ni_{0.40}Cu_{0.15}Zn_{0.45}Fe_2O_4$. For sample $Ni_{0.35}Cu_{0.20}Zn_{0.45}Fe_2O_4$, Q factor first decreases and then increase with increasing the sintering temperature.

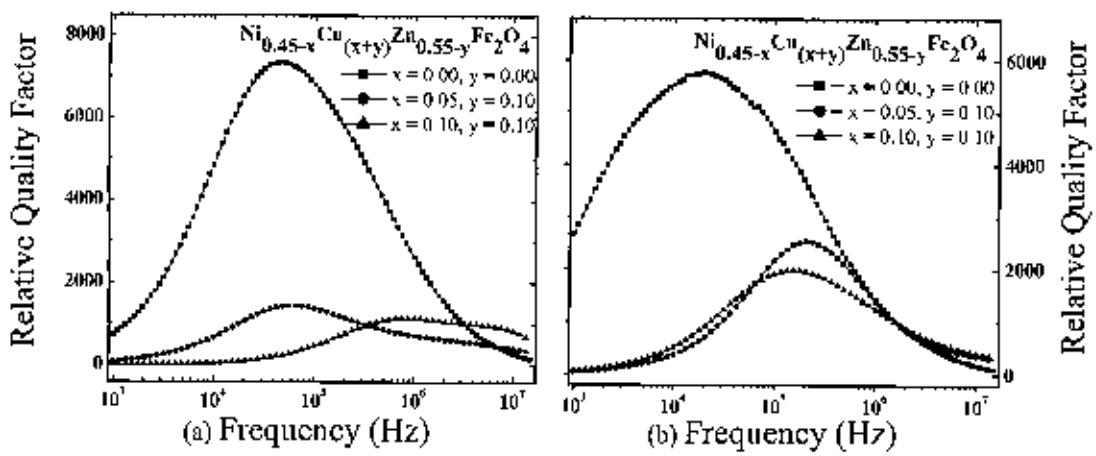

Fig.5.37: The variation of Quality factor with frequency for $Ni_{0.45-x}Cu_{(x+y)}Zn_{0.55-y}Fe_2O_4$ samples sintered at (a) 1250°C and (b) 1300°C

5.2.5. Temperature dependent permeability and Néel temperature

The μ_i', as a function of temperature for various $Ni_{0.45-x}Cu_{(x+y)}Zn_{0.55-y}Fe_2O_4$ sintered at 1250°C is shown in Fig. 5.38. The μ_i' is measured at a constant frequency (100 kHz) of a sinusoidal wave. Permeability falls rapidly when the magnetic state of the ferrite samples changes from ferrimagnetic to paramagnetic. The sharp falling of μ_i' with temperature shows the degree of homogeneity [19] of our samples. The Néel temperature, T_N, is determined by drawing a tangent for the curve at the rapid decrease of μ_i'. The intersection of the tangent with the temperature axis determines T_N. From these curves the T_N's of these samples are determined.

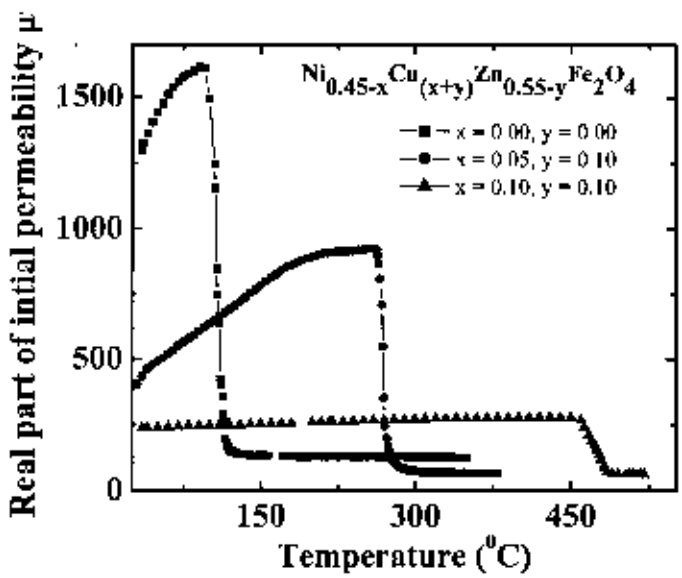

Fig. 5.38: The temperature dependence of μ_i' for $Ni_{0.45-x}Cu_{(x+y)}Zn_{0.55-y}Fe_2O_4$ sintered at 1250°C

It is revealed from Fig. 5.38 that when Cu^{2+} is substituted in the composition $Ni_{0.45-x}Cu_{(x+y)}Zn_{0.55-y}Fe_2O_4$, T_N increases. The T_N for different samples is given in Table-5.4. The increase of the Néel temperature is due to the strengthening of the *A-B* interaction. This could be attributed to the decrease in distance between the moments of *A* and *B* sites, which is shown in Fig 5.39. This is also confirmed by the decrease in the lattice parameter with increasing Cu^{2+} contents in the $Ni_{0.45-x}Cu_{(x+y)}Zn_{0.55-y}Fe_2O_4$ ferrites, which have been confirmed by X-ray diffraction in section 5.2.1.

The shortest distance between moments leads the *A-B* interaction to increase for all the samples and consequently T_N increases.

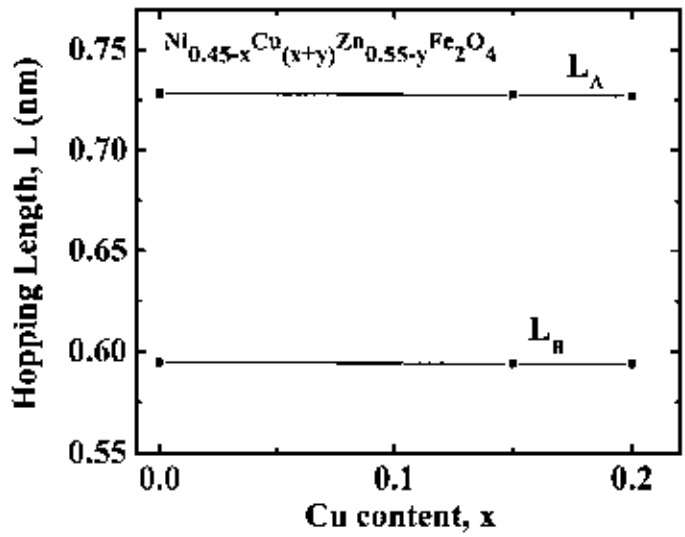

Fig 5.39 The plot of hopping length L in A-site and B-site (L_A and L_B) against Cu^{2+} concentration

5.2.6 DC Magnetization of $Ni_{0.45-x}Cu_{(x+y)}Zn_{0.55-y}Fe_2O$

The magnetization as a function of applied magnetic field, *M-H*, for various $Ni_{0.45-x}Cu_{(x+y)}Zn_{0.55-y}Fe_2O_4$ (with x = 0.00, 0.05, 0.10 and y = 0.00, 0.10, 0.10) samples at room temperature (300K) are shown in Fig. 5.40. The magnetization of all samples increases linearly with increasing the applied magnetic field up to 0.2T Beyond 0.2T

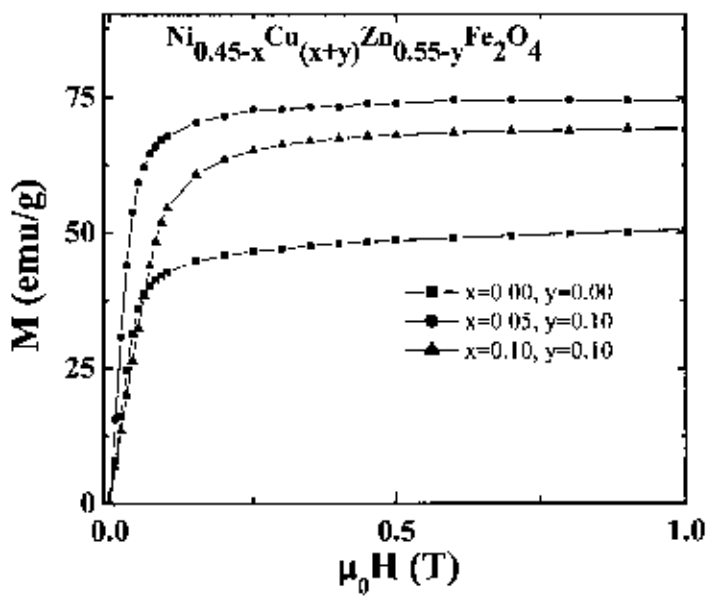

Fig.5.40. The magnetization M versus the applied magnetic field (H) curves for $Ni_{0.45-x}Cu_{(x+y)}Zn_{0.55-y}Fe_2O_4$ samples sintered at 1250°C for 5 h in air.

applied field magnetization increases slowly and then saturation occurs. The saturating magnetizing value, $\mu_0 H_s$, saturation magnetization, M_s, and number of Bohr magneton are tabulated in the Table 5.6.

Table 5.6. The saturation magnetization and Bohr magneton of $Ni_{0.45-x}Cu_{(x+y)}Zn_{0.55-y}Fe_2O_4$ samples sintered at 1250°C

x	y	The field at which saturation occurs, $\mu_0 H_s$ (Tesla)	M_s (emu/g)	n (μ_B)
0.00	0.00	0.40	48	2.047
0.05	0.10	0.35	73	3.114
0.10	0.10	0.30	66	2.819

It is observed from Fig.5.40 that saturation magnetization increases for small substitution of Cu^{2+} (x=0.05) and decrease for x=0.10 in the $Ni_{0.45-x}Cu_{(x+y)}Zn_{0.55-y}Fe_2O_4$. This result can be explained with the help of cation redistribution as result of Cu^{2+} substitution. Perhaps, for small content of Cu^{2+} substitution it prefers B-sites, therefore magnetic moment in B-site is increased and as a result net magnetization also increased. It is also possible that as a result of Cu^{2+} substitution some of the Fe^{3+} converted to Fe^{2+} in B-sites. Since the magnetic moment of Fe^{2+} is less than that of the Fe^{3+}, therefore the net moment is expected to decrease as well as magnetization decrease which is confirmed from Fig.5.40.

References

[1] A. K. M. Akther Hossain, M. Seki, T. Kawai and H. Tabata, "Colossal magnetoresistance in spinel type $Zn_{1-x}Ni_xFe_2O_4$," *J. Appl. Phys.*, 96, 1273 (2004)

[2] A. K. M. Akther Hossain, S. T. ,Mahmud, M. Seki, T. Kawai and H. Tabata, "Structural, electrical transport and magnetic properties of $Ni_{1-x}Zn_xFe_2O_4$," *J. Magn. Magn. Mater., 312, 210-219 (2007)*

[3] R. D. Shannon and C. T. Prewitt, "Effective Ionic Radii in Oxides and Fluorides," *Acta Crystallographica*, B25, 925 (1969)

[4] E. Albers-Schoenberg, ' Ferrites for Microwave Circuits and Digital Computers," *J. Appl. Phys.*, 25, 125 (1954)

[5] www.eng.vt.edu/eng/materials/classproj/example/cu-nih.html.

[6] S. Manjura Hoque, Md. Amanullah Choudhury and Md. Fakhrul Islam, "Characterization of Ni-Cu mixed spinel ferrite," *J. Magn. Magn. Mater*., 251, 292-303 (2002).

[7] A. C. F. M. Costa, E. Tortella, M. R. Morelli and R. H. G. A. Kiminami, "Synthesis, microstructure and magnetic properties of Ni-Zn ferrites," *J. Magn. Magn. Mater.*, 256, 174 (2003).

[8] J. F. Shackelford, M. K. Muralidhara, "*Introduction to Materials Science For Engineers*," Sixth Edition, Pearson Education Inc © (2005)

[9] J. E. Burke,in' W.D. Kingery (Ed.), Ceramic Fabrication Processes,wiley,New York p 120,(1958).

[10] R.L. Lange, B.J. Kellet, ' Thermodynamics of Densification :II.Grain Growth in Porous Compacts and Relation to Densification," *J. Am. Ceram. Soc.*, 72, 735 (1989).

[11] M.M. Barakat, M.A. Hanaish,S.A.Olola and A. Tawfik, ' Sintering behaviour of the spinel ferrite system $Ni_{0.65}Zn_{0.35}Fe_{2-x}Cu_xO_4$" *J. Thermal Analysis*,37, 241-248 (1991)

[12] S.T. Mahmud, A. K. M. Akther Hossain, A.K.M. Abdul Hakim, M. Seki, T. Kawai and H. Tabata, " Influence of microstructure on the complex permeability of spinel type Ni-Zn ferrite," *J. Magn. Magn. Mater.*, 305,269 (2006).

[13] H. P. Klug, L. E. Alexander, "X-ray Diffraction Procedures for Polycrystalline and Amorphous Materials",John Wiley and Sons.New York,p.637 (1997).

[14] R. LEBOURGEOIS, J. P. GANNE and B. HLORT, "High frequency Mn-Zn power ferrites," *J. Phys. IV France 7* Suppl. C1. 105-108 (1997).

[15] Hu Jun and Yan Mi, "Preparation of high permeability Ni-Cu-Zn ferrite," *Journal of Zhejiang University Science*, 6B(6). 580 (2005).

[16] T. Tsutaoka, M. Ueshima, T. Tokunaga, T. Nakamura and K. Hatakeyama, "Frequency dispersion and temperature variation of complex permeability of Ni-Zn ferrite composite materials " *J. Appl. Phys.*, 78(6), 3983 (1995)

[17] A K. M. Akther Hossain. T S Biswas, S. T. Mahmud, Takeshi Yanagida, Hidekazu Tanaka, Tomoji Kawai, "Influence of Mg and Cr substitution on structural and magnetic properties of polycrystalline $Ni_{0.50}Zn_{0.50-x-y}Mg_xCr_yFe_2O_4$," *Materials chemistry and physics*, 113(1) 172-178 (2009)

[18] A GLOBUS, Thesis, Univ. of Paris. Paris, France (1963)

[19] R. Valenzuela, *Magnetic Ceramics*, Cambridge University Press, Cambridge (1994).

[20] P Brailsford, *Physical Principles of Magnetism*, D. Van Nostrand Company Ltd., London (1966)

[21] B D Cullity *Introduction to Magnetic Materials*. Addison-Wisley Publishing Company, Inc California (1972)

[22] S A Ghodake,U R. ghodake,S R. Sawant S.S Suryavanshi,P.P.Bakare, "Magnetic properties of NiCuZn ferrites synthesized by oxalate precursor method," *J Magn. Magn. Mater* , 305, 110-119 (2006).

[23] I Z. Rahman and T. T. Ahmed, "A study on Cu substituted chemically processed Ni-Zn-Cu ferrites," *J. Magn. Magn Mater.*, 290-291, 1576-1579 (2005).

[24] T. T Ahmed, I Z. Rahman,and S. A M Tofail, "Effect of copper ion distribution on the magnetization of nanoscaled NiZn ferrite," *J. Magn. Magn. Mater* , 272-276,Part3 2250-2252 (2004).

[25] Tahir abbas, M. U. Islam and M Ashraf Ch, "Study of sintering behaviour and electrical properties of Cu-Zn-Fe-0 system," *Mod Phy. Letts.*, B.9 (22). 1419-1426 (1995).

CHAPTER 6

CONCLUSIONS

Nanocrystalline various $Ni_{0.50-x}Cu_xZn_{0.50}Fe_2O_4$ and $Ni_{0.45-x}Cu_{(x+y)}Zn_{0.55-y}Fe_2O_4$ ferrites were successfully prepared by combustion technique. The XRD patterns of various $Ni_{0.50-x}Cu_xZn_{0.50}Fe_2O_4$ and $Ni_{0.45-x}Cu_{(x+y)}Zn_{0.55-y}Fe_2O_4$ clearly indicate their single phase and formation of spinel structure. Lattice parameter, a_o, increases with increasing of Cu^{2+} content in $Ni_{0.50-x}Cu_xZn_{0.50}Fe_2O_4$, whereas a_o, decreases in $Ni_{0.45-x}Cu_{(x+y)}Zn_{0.55-y}Fe_2O_4$. These phenomena are explained in terms of their ionic radii. Since the ionic radii of both of Cu^{2+} (0.72Å) and Ni^{2+} (0.69Å) are smaller than Zn^{+2}(0.82 Å) therefore, a_o, decreases in $Ni_{0.45-x}Cu_{(x+y)}Zn_{0.55-y}Fe_2O_4$ and increases in $Ni_{0.50-x}Cu_xZn_{0.50}Fe_2O_4$. It is also observed that the theoretical density of all compositions increases though the increases of lattice constant in $Ni_{0.50-x}Cu_xZn_{0.50}Fe_2O_4$ ferrites. Since the theoretical density or X-ray density depends upon the lattice constant and the molecular weight of the samples. Bulk density of the all sample of $Ni_{0.50-x}Cu_xZn_{0.50}Fe_2O_4$ ferrites increases and porosity decreases up to the optimum level of copper content and beyond that level density decreases and as well as porosity increases. But in case of $Ni_{0.45-x}Cu_{(x+y)}Zn_{0.55-y}Fe_2O_4$ bulk density decreases and porosity increases with the increasing copper content. Bulk density of all samples of $Ni_{0.50-x}Cu_xZn_{0.50}Fe_2O_4$ ferrites increases as the sintering temperature increases from 1100°C to 1200°C and beyond this temperature bulk density decreases except for $Ni_{0.50}Zn_{0.50}Fe_2O_4$,which decrease above 1250°C. For the $Ni_{0.45-x}Cu_{(x+y)}Zn_{0.55-y}Fe_2O_4$ systems bulk density increases with increasing sintering temperature from 1200°C to 1250°C and above 1250°C density decreases. On the other hand, porosity decreases with increasing sintering temperature from 1200°C to1250°C, and above 1250°C, porosity increases. During the sintering process, the thermal energy generates a force that drives the grain boundaries to grow over pores, thereby decreasing the pore volume and increasing the density of the materials. At higher sintering temperatures the density decreases, because the intragranular porosity increases as a result of discontinuous grain growth which leads to decrease the sintered density. The grain size increases with increasing of copper content, x=0.15 in the $Ni_{0.50-x}Cu_xZn_{0.50}Fe_2O_4$. Beyond this value of x, grain size decreases. The study of microstructure shows that, grain size also increases with increasing sintering temperature. The particle sizes of these compositions are found

in the rage of 0 22nm to 0 73 nm On the other hand, for the $Ni_{0.45-x}Cu_{(x+y)}Zn_{0.55-y}Fe_2O_4$ systems particle size range is 0.58nm to 0.67nm depending upon on the composition.

The real part of permeability, μ_i', increases with increasing copper content up to x=0.10 in $Ni_{0.50-x}Cu_xZn_{0.50}Fe_2O_4$ because the average grain size increases with increasing Cu^{2-} content. The μ_i' decreases with increasing Cu^{2+} content in $Ni_{0.45-x}Cu_{(x+y)}Zn_{0.55-y}Fe_2O_4$ except for $Ni_{0.35}Cu_{0.20}Zn_{0.45}Fe_2O_4$. At higher temperature generally permeability depends on grain size, and grain size increases with increasing sintering temperatures So it is seen that permeability increases with increasing sintering temperatures for various $Ni_{0.50-x}Cu_xZn_{0.50}Fe_2O_4$ and $Ni_{0.45-x}Cu_{(x+y)}Zn_{0.55-y}Fe_2O_4$. For $Ni_{0.40}Cu_{0.15}Zn_{0.45}Fe_2O_4$ μ_i' increases as the sintering temperature increases from 1200°C to 1250°C and above 1250°C this value decreases. At high sintering temperatures some pores are trapped within grain boundary for rapidly growing grains Therefore the μ_i' decreases though grain size increase.

The resonance frequency, f_r decreases first with increasing Cu^{2+} content up to a certain level in $Ni_{0.50-x}Cu_xZn_{0.50}Fe_2O_4$ After that level f_r increases. On the other hand, for $Ni_{0.45-x}Cu_{(x+y)}Zn_{0.55-y}Fe_2O_4$ resonances frequency increases with increasing Cu^{2+} content, except at higher sintering temperature It is found that resonance frequency is shifted from higher value to lower value as sintering temperature increases for all samples. It is observed that $Ni_{0.56}Zn_{0.5}Fe_2O_4$ shows highest f_r for $Ni_{0.50-x}Cu_xZn_{0.50}Fe_2O_4$ series, which is 5 36 MHz (sample sintered at 1100°C) and $Ni_{0.35}Cu_{0.20}Zn_{0.45}Fe2O_4$ shows 7.20 MHz (sample sintered at 1200°C) for $Ni_{0.45-x}Cu_{(x+y)}Zn_{0.55-y}Fe_2O_4$ series.

The loss factor increases with the increasing Cu^{2+} content and sintering temperature in the $Ni_{0.45-x}Cu_{(x+y)}Zn_{0.55-y}Fe_2O_4$ On the other hand, loss factor decreases with increasing Cu^{2+} content up to x=0.20 in the $Ni_{0.50-x}Cu_xZn_{0.50}Fe_2O_4$. Beyond this value of x, loss factor again increases. It is observed that Q factor decreases with increasing sintered temperature. For inductors used in filter applications, the Q factor is often used as a measure of performance The highest Q value obtained in $Ni_{0.30}Cu_{0.20}Zn_{0.50}Fe_2O_4$ is 9380, probably due to the growth of lesser imperfection.

The T_N decreases with increasing Cu^{2+} content in $Ni_{0.50-x}Cu_xZn_{0.50}Fe_2O_4$ and increases in $Ni_{0.45-x}Cu_{(x+y)}Zn_{0.55-y}Fe_2O_4$. The decrease of the Néel temperature with Cu^{2+} substitution is due to the weakening of the A-B interaction and increases due to the strengthen of the A-B interaction in the spinel lattice. This could be attributed to the

increase and decrease in distance (hopping length, L) between the magnetic ions of tetrahedral A- site (L_A) and the octahedral B-sites (L_B). The highest T_N for $Ni_{0.50-x}Cu_xZn_{0.50}Fe_2O_4$ ferrites is 266°C and for $Ni_{0.45-x}Cu_{(x+y)}Zn_{0.55-y}Fe_2O_4$ is 469°C.

From magnetization as a function of applied magnetic field, $M(H)$ curves, it is clear that at room temperature all compositions of $Ni_{0.50-x}Cu_xZn_{0.50}Fe_2O_4$ and $Ni_{0.45-x}Cu_{(x+y)}Zn_{0.55-y}Fe_2O_4$ are in ferrimagnetic state. The M_s, as well as μ_B, of all the compositions, decreases with increasing Cu^{2+} content up to x=0.15.Beyond this vale of x, the M_s and as well as μ_B, values increase with increasing Cu^{2+} content These results are explained with the help of cation redistribution in A- site and B- site of the spinel crystal structure. Magnetization decrease since the magnetic moment of the Cu^{2+} is lesser than that Ni^{2+}, resulting the decrease of the A-B interaction as well as net magnetization. There is strong evidence that Cu^{2+} change to Cu^{+} at higher copper concentration. The Cu^{+} has a preference to accommodate themselves in A-sites which Cu^{+} can force some of Fe^{3+} migrate from A-sites to B-sites. This migration of Fe^{3+} to B-sites will lead to an increase in magnetization in B-sites leading to the increase of the saturation magnetization in $Ni_{0.50-x}Cu_xZn_{0.50}Fe_2O_4$ On the other hand, for the $Ni_{0.45-x}Cu_{(x+y)}Zn_{0.55-y}Fe_2O_4$ it is also possible that as a result of Cu^{2+} substitution some of the Fe^{3+} converted to Fe^{2+} in B-sites. Since the magnetic moment of Fe^{2+} is less than that of the Fe^{3+}, therefore the net moment is expected to decrease as well as magnetization decrease with the increasing of Cu^{2+} content.

.....